Numerical Modelling of the Effect of Lateral Nonuniformity due to Horizontal Flow Contraction on Flow Dynamics over a Steep Slope

By

Rahadian Rukmana

UNIVERSITY OF TWENTE. | Deltares

Date: July 14th, 2023

Conducted by:

Rahadian Rukmana
s2054817
Rahadianrukmana@student.utwente.nl

Commissioned by:

Deltares
Dr. Ir. Y. (Yorick) Broekema
Yorick.broekema@deltares.nl

Deltares
Dr. Ir. D. (Désirée) Plenker
Desiree.plenker@deltares.nl

Supervised by:

The University of Twente
Dr. Ir. P.C. (Pieter) Roos
p.c.roos@utwente.nl

The University of Twente
Dr. V. (Vasileios) Kitsikoudis
v.kitsikoudis@utwente.nl

The University of Twente
Ir. F. (Fateme) Ebrahimierami
f.ebrahimierami@utwente.nl

UNIVERSITY OF TWENTE. | **Deltares**

Preface

Ah, the journey of adulthood, a mysterious and thrilling expedition that we embark upon with equal parts excitement and trepidation. As I stand on the precipice, gazing at this monumental master thesis, I can't help but feel a rush of emotions, like a rollercoaster ride through the corridors of knowledge. The past five years at the University of Twente has been nothing short of pleasant surprises, like discovering a hidden treasure chest of friendship, experience, and existential crisis. So, allow me to raise my virtual glass and extend my heartfelt gratitude to the incredible individuals who made this adventure truly epic.

To my extraordinary professors, thank you for imparting your wisdom and knowledge wholeheartedly with such passion, making me slightly wiser and infinitely more caffeinated. I promise to use this knowledge for good and not for evil (or at least most of the time). To my incredible friends, my ride-or-die, my source of endless laughter and support. You've been with me through thick and thin, enduring my endless rants about my study, life, and the mysteries of why I'm still single. *I still think I have a good personality*. We may have been sleep-deprived, but we were never short on laughs and unforgettable memories. Thank you for reminding me that "it's not just the grades you make, but it's the hands you shake". Ah, my dearest best friend, Rayhan, the Batman to my Robin, the Holmes to my Watson, words cannot express the depth of my gratitude. You've been the comedic relief throughout my student life and the scholarly chaos and countless drafts of this thesis, reminding me to always find joy in the process and that I'm a terrible cook. Of course, my gratitude extends to my amazing family, who has been the wind beneath my wings throughout this journey. Despite the distance and time difference, your love and belief in me have crossed oceans and time zones.

Now, let me express my deep appreciation to Yorick and Désirée who have welcomed me at Deltares for my master thesis. Yorick, your research has inspired me beyond words; without which there would be no thesis, literally. Your patience and expertise have been invaluable as you propelled me forward in the right direction as I float in a sea of confusion. Désirée, thank you for generously sparing your time when I showed up at your office twice every five minutes, I practically had a permanent reservation. Thank you for your patience in answering my questions that ranged from genius to utterly weird and for being patient when I understood your answers differently. A heartfelt appreciation also goes to Vasileios and Fateme, who helped lay the foundation of this research. Your unwavering support and generosity in sharing your knowledge have helped me connect the unconnectable dots, and I am forever grateful for your support. And Pieter, thank you for your reassurance and encouragements that protected me from self-doubt and reminding me that I am capable. To Marijke Stehouwer and Judith Roos, who have granted me the gift of a scholarship and a tale worth sharing with the world, I am forever indebted.

As I conclude this preface, my heart is filled with gratitude and a touch of nostalgia. These years of academic exploration have brought me not only knowledge but also cherished connections and memories that will last a lifetime. I will always carry them with me. To everyone who played a part in shaping my academic and personal growth, thank you from the bottom of my caffeinated heart. You've made this adventure one for the books, filled with laughter, learning, and occasional existential crisis. Thank you for turning the pages of my story into a heart-warming masterpiece. With love, Ian.

Abstract

This research is motivated by recent findings indicating the presence of a three-dimensional flow phenomenon near hydraulic structures, characterized by the jet-like flow and lateral nonuniformity (Broekema et al., 2018, 2019). This phenomenon has been observed to potentially enhance scour near the Eastern Scheldt Storm Surge Barrier, the Netherlands (Broekema et al., 2018). Broekema et al. (2019) further demonstrated experimentally that flow separation over steep slopes may be supressed due to lateral non-uniformity on the upstream flow field, thereby enhancing scour potential.

With limited understanding of this phenomenon, this study aims to investigate flow characteristics and turbulence behaviour using numerical simulations, namely the RANS turbulence model. The numerical simulation cases build upon the open channel experiment conducted by Broekema et al. (2019) that inspired this research. The cases vary the steepness of the bed slope (resembling the scour hole) and the distance between the obstruction and the upstream edge of the slope (resembling bed protection) which controls the magnitude of the lateral velocity gradient. The simulations were conducted using OpenFOAM with the PIMPLE algorithm, suitable for the unsteady flows, coupled with the $k - \omega$ SST turbulence closure model.

The findings revealed the relationship between the distance of the obstruction to the slope and flow separation. Placing the obstruction further upstream allowed for the development of a mixing layer over greater distance, which reduces the lateral velocity gradient and resulting in flow divergence that resembles a horizontally uniform flow, and ultimately leading to flow separation. Conversely, placing the obstruction closer to the slope led to vertical flow attachment due to a larger lateral non-uniformity. From a practical standpoint, this observation may have relevance in the design of hydraulic structures, whereby bed protections around hydraulic structures should be sufficiently long to allow for sufficient mixing to occur, reducing the velocity differences and turbulence intensities, to induce vertical flow separation and minimize the risks of flow attachment such as enhanced scour and erosion.

Moreover, this study elucidated the notable correlation between the pressure field and flow separation. In all instances of vertical flow separation, an adverse pressure gradient was consistently observed upstream and downstream of the slope. This adverse pressure gradient occurred as the flow depth increased, leading to flow deceleration. Conversely, in situations of flow attachment, a decrease in pressure prior to the slope indicated flow acceleration as the flow converged horizontally. Consequently, the deceleration of the flow from the increased flow depth at the slope was reduced, resulting in a diminished adverse pressure gradient and the boundary layer staying attached to the bed.

The model demonstrated good agreement with the measurement data upstream of the slope in all cases. Discrepancies between the model and measurement data were observed around the slope, where high turbulence intensities were measured. The model

consistently underpredicted this turbulence and the turbulent kinetic energy in all cases which indicates the limitations of the RANS modelling approach. The assumption of turbulence isotropy in RANS does not adequately reflect the actual behaviour of turbulence. In contrast, these shallow shear flows exhibit anisotropic turbulence motion responsible for the transverse exchange of mass and momentum (van Prooijen & Uijttewaal, 2002). Furthermore, the RANS model simulates all turbulence length scales simultaneously which lacks the resolution necessary to capture the energy transfer between larger and smaller eddies, thereby hindering not only the interaction between the turbulence structures and the bottom turbulence but also the turbulence associated with the mixing layer (vortex shedding). In light of these findings, this research suggests employing higher-resolution models such as DES and LES along with free-surface modelling, to improve accuracy.

Table of Contents

List of Figures

List of Tables

1. Introduction

1.1. Scour Holes and Hydraulic Structures

Scour holes (large local erosion pits), because of large-scale erosion of an alluvial bed, are common in the vicinity of hydraulic structures; and the Eastern Scheldt storm surge barrier, the Netherlands, being a hydraulic structure (weir), is no exception. Downstream of said barrier, there exist scour holes adjacent to the applied bed protection (van Velzen et al., 2014). From the very beginning of the hydraulic structure's design phase, scouring as a phenomenon was already expected to arise. However, both the scour depth and its growth could not have been predicted well with good accuracy, despite the development of empirical relations (Breusers, 1967; Dietz, 1969; Zanke, 1978) and physical-model studies (Hoffmans & Verheij, 2021) that are largely based on 2D-vertical understanding (Ghodsian & Vaghefi, 2009; Guan et al., 2013; G. Hoffmans & Booij, 2010). However, the reality is that flows downstream of a hydraulic structure are rarely two-dimensional (Broekema et al., 2018), given, for instance, the lateral nonuniformity induced by the jet-like flow downstream of the hydraulic structure.

Predicting the scour hole formation and the corresponding mitigation strategies requires an understanding of the hydrodynamics (the flow) and the subsequent morphodynamical changes (i.e., the response of the sandy bed). Bed protection, amongst other mitigation measures, aims to either reduce the depth of the scour holes or ensure that scour holes are located at a distance that does not compromise the geotechnical stability of the hydraulic structure which may lead to structural failure (Bey et al., 2007; Broekema et al., 2018; Dargahi, 2010). Hoffmans and Verheij (2021) outlined that the expected equilibrium scour depth at the Eastern Scheldt storm surge barrier downstream of the bed protection, according to 2D-vertical formulations, is approximately 2.2 times the reference water depth; which is where the level is currently observed. Nevertheless, continual observation of the scour has shown that erosion is still taking place (Broekema et al., 2018).

In explaining this scour prediction, a breakthrough by Broekema et al. (2018, 2019), revealed a scour-enhancing mechanism downstream of the Eastern Scheldt storm surge barrier; whereby horizontal convergence of the flow was observed, followed by a flow that remains attached to the sloping bed of the scour hole as opposed to flow separation. Hence, the mutual interaction between the horizontal and vertical flow states is presumed to enhance the scour potential, which may explain the deviation in scour predictions. This finding suggests that there is another facet to scouring that is not captured by 2D empirical relations or physical model experiments. It signalled for the three-dimensionality of the flow characteristics and thus the need for a three-dimensional approach, emphasising that a 2D-vertical approximation may be incomplete for some aspects of the phenomenon. However, due to the novelty of this discovery, the understanding of this phenomenon is still limited.

1.2. Problem Analysis

A recent field investigation by Broekema et al. (2018), indicated that horizontal shear flow characterized by lateral velocity gradient in the streamwise velocity leads to a self-amplifying scour mechanism; that is, through a phenomenon called vertical flow attachment and horizontal convergence attributed to potential vorticity conservation. In another study, Broekema et al. (2019) further investigated this notion through a physical flume experiment resembling a flow downstream of a hydraulic structure (see Figure 1), where a flow is constricted at one side of the flume upstream (to induce flow non-uniformity) of a linearly sloping bed (resembling the scour) that is steep enough to ensure flow separation. The obstruction and its distance to the upstream edge of the slope (resembling bed protection) control the magnitude of the lateral velocity gradient; this is based on the understanding that the development of a mixing layer which widens in the streamwise direction gradually reduces the lateral velocity gradient (Talstra, 2011; van Prooijen & Uijttewaal, 2002).
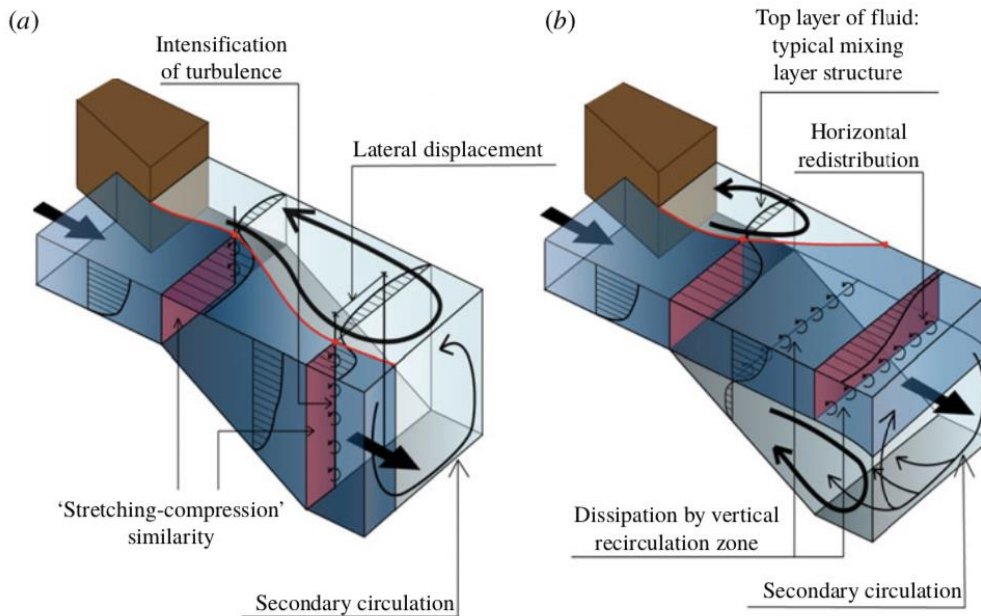
Figure 1: Conceptualization of the two flow states observed in the flume experiment. A) vertically attaching and converging in the horizontal plane b) Vertically separating and diverging in the horizontal plane. Obtained from Broekema et al. (2019).

From this experiment, it was found that the magnitude of lateral velocity gradient highly influences the transition between a) flow attachment and horizontal convergence to b) flow separation and horizontal divergence; the higher magnitude being more likely to result in flow attachment (Broekema et al., 2019). These flow states are illustrated in Figure 1. However, Broekema et al. (2019) argued that this phenomenon cannot be explained through potential vorticity conservation or adverse pressure gradient alone, but rather the local behavior of the flow; that is the interaction between the lateral velocity gradient and the turbulence or recirculation zone induced by the slope. Yet, this aspect of the study could not be fully examined. Hence, further investigation through

high-resolution numerical modelling may provide additional insights into the complexities surrounding the transition between flow states.

Numerical simulations in fluid dynamics have grown in usage due to the continuous development of computational power and its ability to circumvent limitations or drawbacks of experimental procedures such as the cost and time to, for example, perform many different (flume) experiments (Pereira et al., 2021). Most computational fluid dynamics (CFD) are based on the Navier-Stokes equations to simulate fluid motion (Hu, 2012). However, the primary challenge to using CFD in simulating flows of engineering problems is modelling turbulence (Pereira et al., 2021). Turbulence is present in various temporal and spatial scales whose interactions are non-linear (Pereira et al., 2021) and it governs the physics such as energy dissipation and mixing, just to name a few (Hanjalic, 2004; Jaramillo Ibarra et al., 2008; Pereira et al., 2021). Simulating this multiscale phenomenon depends on the purpose, application, and flow features of interests (Pereira et al., 2021).

The Reynolds-Averaged Navier-Stokes (RANS) turbulence model has been the workhorse of engineering practices due to its computational effectiveness in modelling all turbulence scales as opposed to other more demanding techniques such as Direct Numerical Simulation (DNS) and Large-Eddy Simulation (LES) which fully and partially resolves the turbulence scales, respectively (Jaramillo Ibarra et al., 2008; Lü et al., 2021; Molland & Turnock, 2007; Pereira et al., 2021). This computational advantage, however, comes with a limitation. For instance, while RANS is able to reproduce (primary) recirculation zones (Babarutsi et al., 1996; Bijvelds et al., 1999; Thangam & Speziale, 1991), Talstra (2011) argued that coherent structures are not well reproduced with RANS since all turbulence scales are equally represented and time-averaged; and further noted that resolving individual structures is important to simulate the dynamics of coherent structures and that LES is better suited for this purpose. The use of RANS turbulence model involves utilizing turbulence closure models. These models apply mathematical equations to generate values for the Reynolds stresses and provide an engineering approximation of how turbulence affects the mean-flow field (Hanjalic, 2004; Molland & Turnock, 2007; Pereira et al., 2021). In a CFD simulation, the choice of turbulence model closure depends on the type of turbulent flow being studied (Tu et al., 2018). The selection process requires a thorough validation and verification procedure, such as performing sensitivity analysis with different turbulence closure models and comparison of the numerical solutions with experimental data (Tu et al., 2018).

1.3. Research Objective

Based on the problem analysis, further research utilizing numerical model, such as the RANS turbulence model, can provide valuable insights into the complex transition between the flow states as influenced by turbulence, slope characteristics and lateral velocity gradients. This leads to the following research question:

"How does the RANS turbulence model perform in simulating flow separation under horizontal shear flow conditions and linearly sloping bed?"

In answering the main research question, this research is organized around three sub-questions, namely:

1. What is the impact of the turbulence closure model on the RANS simulations' capability to simulate flow separation under horizontal shear flow conditions and a linearly sloping bed?
2. How capable is the RANS turbulence model in simulating flow separation under horizontal shear flow conditions and a linearly sloping bed, considering the influence of different slope angles?
3. What is the impact of the spacing between the horizontal obstruction and the upstream edge of the slope on the flow state at the slope?

Research question one focuses on the influence of the turbulence closure model in capturing the general features of the flow characteristics and how the choice of turbulence closure model affects the predictive capabilities of the RANS turbulence model. Research question two delves into the influence of the slope angles on the flow. By examining various slope angles, the question aims to uncover the model's ability to capture the sensitivity of the flow behavior to varying angles, taking into account the additional turbulence that may be induced by the steeper slope (Broekema et al., 2019). Research question three expands the scope to include different spacings between the horizontal obstruction and the upstream edge of the slope, which directly affects the magnitude of the lateral velocity gradient. By examining various spacing scenarios, the question aims to highlight the model's ability to predict the effect of this interaction on flow separation or attachment.

1.4. Report Outline

This report guides you through six successive chapters. The first chapter, as already outlined, introduced the research background and objective of this study. **Chapter 2** elaborates on the theoretical framework, consisting of theories in the Navier-Stokes equation, horizontal shear flows, flow separation, current knowledge state based on the previously conducted research and the modelling approach. **Chapter 3** expands upon the numerical methodology used to conduct the numerical studies of this research. **Chapter 4** presents the result of the numerical studies, followed by discussion of the result in

Chapter 5. Lastly, this study is concluded with **Chapter 6** – entailing the conclusion of the research and recommendations for further research.

2. Theoretical Framework

The following chapter elaborates on the theoretical background derived from the literature study previously performed. Firstly, the hydrodynamic principles required to interpret the current knowledge state and the results later are presented. This includes the general equation of motion, the Navier-Stokes equation; vorticity; horizontal shear flows; and the fundamentals of flow attachment and separation. Secondly, as this research builds on previous research of Broekema et al. (2019) on the relationship between lateral non-uniformities and vertical flow attachment, the current knowledge state is presented. Thirdly, the RANS equation and turbulence model are explained.

2.1. The Navier-Stokes equation and vorticity

The motion of fluids, both liquids and gases, is mathematically governed by the Navier-Stokes equation of motion. This equation, taking the form of a set of partial differential equations describes the flow of fluids based on principles of conservation of mass and momentum. Here, the Navier-Stokes equation for an incompressible homogenous three-dimensional flow with no body forces and the continuity equation respectively are presented.

$$\rho \left[\frac{\partial \boldsymbol{u}}{\partial t} + (\boldsymbol{u} \cdot \nabla)\boldsymbol{u} \right] = -\nabla p + \mu \nabla^2 \boldsymbol{u} \tag{1}$$

$$\nabla \cdot \boldsymbol{u} = 0 \tag{2}$$

Where $\boldsymbol{u}$ is the fluid velocity vector $\boldsymbol{u} = (u, v, w)$ and ∇ is the gradient operator; p is the non-hydrostatic normalized pressure ($p = P/\rho + gz$, where P (kg m^{-1} s^{-2}) is the hydrodynamic pressure); ρ being the (constant) fluid density (kg m^{-3}) ; and μ being the dynamic fluid viscosity (kg m^{-1} s^{-1}) and g being the gravitational acceleration (9.81 m s^{-2}).

Turbulence is primarily brought on by two aspects of the Navier-Stokes equations (Talstra, 2011). Firstly, with a large Reynolds value, Re ($= \mathcal{U}\mathcal{L}/(\mu/\rho) > 2000$, where $\mathcal{U}$ and $\mathcal{L}$ are the velocity and characteristic length, respectively), a flow problem can become hydrodynamically unstable (Nieuwstadt et al., 2016) and display turbulent behavior. Secondly, even in cases where the initial flow field did not contain rotation, viscous forces coupled with no-slip boundary conditions may introduce rotation (vorticity) into the velocity field (Talstra, 2011). As a result, a turbulent flow field includes vortices or "eddies" due to the presence of vorticity and turbulence is considered a 3D phenomenon (Talstra, 2011). In the physical sense, said vortices (coherent structures) are unstable and they break down into smaller vortices whereby the turbulent kinetic energy is passed down to the smaller scales of eddies until it reaches the smallest length scale (the so-called Kolmogorov scales) before the energy is being transformed into heat due to viscosity. This is coined as the 3D energy cascade. Taking the curl of the entire equation

1 and defining vorticity as the curl of the velocity field ($\boldsymbol{\omega} = \nabla \times \mathbf{u}$) gives the vorticity equation, which highlights the role of vorticity in the energy cascade:

$$\frac{\partial \boldsymbol{\omega}}{\partial t} + (\mathbf{u} \cdot \nabla)\boldsymbol{\omega} = (\boldsymbol{\omega} \cdot \nabla)\mathbf{u} + \mu\nabla^2\boldsymbol{\omega} \tag{3}$$

$$(\boldsymbol{\omega} \cdot \nabla)\mathbf{u} = \mathbf{S}\boldsymbol{\omega} \tag{4}$$

Whereby $\boldsymbol{\omega}$ is the vorticity vector and $\mathbf{S}$ is the velocity gradient tensor ($\mathbf{S} = \frac{1}{2}(\nabla\boldsymbol{u} + \nabla\boldsymbol{u}^{\mathrm{T}})$). Of particular interest here is the first term on the right-hand side of equation (3, which is the vortex stretching term. This term signifies that the local vorticity will increase if the velocity field is stretched along the direction of the local vorticity vector and that energy is transferred to smaller scales of eddies (Talstra, 2011).

Despite turbulence essentially being a 3D phenomenon, it is commonly found that turbulent flows are restricted in one of its three dimensions; often in the vertical direction or depth (Talstra, 2011). Hence, the flow can be considered as a shallow flow and the large-scale turbulence can be considered quasi-two-dimensional which differs from the 3D turbulence dynamics. This distinction means that the vorticity vector in the vorticity equation (equation (3, consists of only one component ($\boldsymbol{\omega} = (0, 0, \omega_z)$), perpendicular to the 2D velocity field (Talstra, 2011). This means that because of vertical restriction, vortex or velocity stretching in this perpendicular direction is not possible but instead, horizontal vortices can grow to length scales larger than the water depth (Broekema, 2020); and the aforementioned vortex stretching term vanishes because the vertical flow velocity is negligible, such that $\partial w/\partial z = 0$. Hence, theoretically, vorticity is conserved in 2D or shallow flows and an increase in flow depth would suggest that it allows for more vortex stretching (Broekema, 2020). The presuppositions elaborated above hold for the ideal 2D inviscid configurations (Talstra, 2011). Although the reality tends to deviate from this ideal, shallow turbulent flows display many 2D characteristics, hence the quasi-2D flow behavior, where vortex stretching is hindered in the vertical direction and the energy dissipation capacity is strongly reduced.

2.2. Horizontal shear flows

Horizontal shear flows occur due to lateral velocity differences among fluid particles and the associated fluid viscosity that results in shear force. In other words, there exist considerable horizontal shear flows when large lateral differences in streamwise velocity are present. In environmental flows, said phenomena could arise due to e.g., variations in transverse topography (van Prooijen et al., 2005) and separation of flow downstream of hydraulic structures (Jirka, 2001), just to name a few. Regarding horizontal shear flows, two distinctions can be made, namely free and shallow shear flows. The difference is that the former has "infinite" depth whereas the latter has "finite" depth, therefore the presence of the walls and bottom friction cannot be neglected (Talstra, 2011; van Prooijen & Uijttewaal, 2002).

Horizontal shear flows are characterised by the development and expansion of horizontal coherent structures (2DCS) which are defined as large-scale turbulent fluid masses that span the full water depth (Jirka, 2001). Furthermore, the size of 2DCS often grows in the downstream direction, due to the phenomenon called entrainment; whereby smaller scales or weaker turbulence are engulfed by the large growing coherent structures. However, consistent with the previously elaborated confinement, the size and behaviour of horizontal vortices are greatly influenced by the relative shallowness of the flow (Jirka, 2001; Talstra, 2011). For instance, Jirka (2001), suggested a theoretical upper limit for the size of an eddy given that larger eddies dissipate their kinetic energy more rapidly when their size-to-depth ratio increases.

Jirka (2001) identifies three mechanisms that generate horizontal coherent structures, namely: 1) topographical forcing, the strongest of the three, which arises from forced flow separation around objects or geometric features such as groynes and weirs, resulting in transverse shear and return velocities that give rise to 2DCS; 2) internal transverse shear instabilities, which generates 2DCS due to lateral velocity differences and subsequent hydrodynamic instabilities without external forcing apart from bottom friction, leading to internal turbulence; 3) secondary instability of the base flow, weakest of the three, where 2DCS emerges as a backscatter of 3D turbulence structures to larger scales, often caused by underwater obstacles or decelerations in the base flow. In the context of the flow downstream of the Eastern Scheldt Storm Surge Barrier, topographical forcing is the dominant mechanism, although the presence of internal transverse shear instabilities cannot be ruled out, particularly due to the jet-like flow structure. Figure 2 provides illustration of these three types of 2DCS.
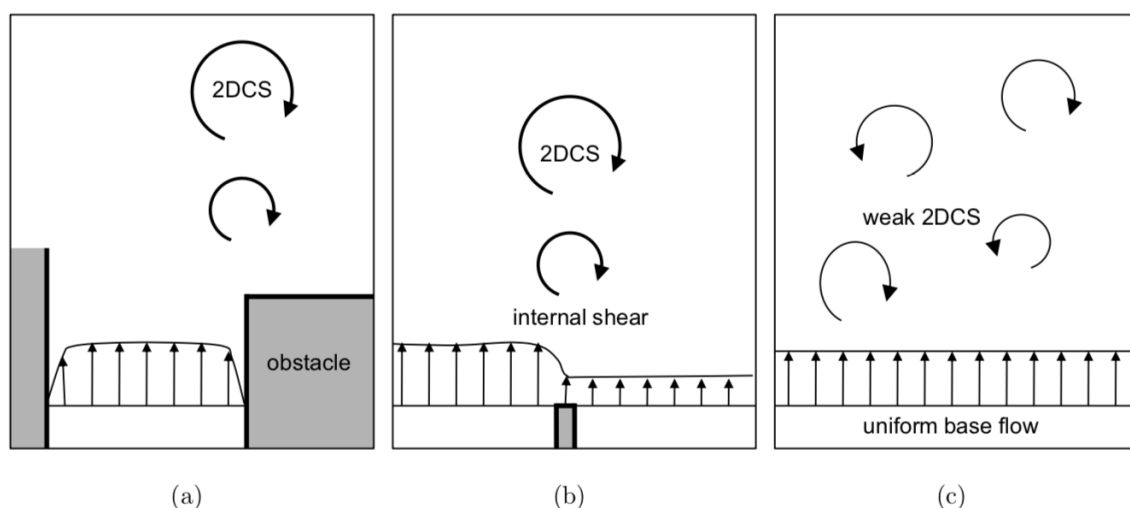
Figure 2: Illustration of three mechanisms leading to 2DCS from the top view. a) topographical forcing; b) Internal transverse shear instabilities; c) secondary instability of base flow. Obtained from Talstra (2011).

2.3. Flow separation and recirculation zone

Flow separation occurs when a boundary layer detaches from a confining wall surface it is moving parallel to, due to an adverse pressure gradient against the flow direction. Change in the fluid velocity, brought about by features like sharp edges (geometrical reasons) or flow expansions are typical causes of this phenomenon (Schiereck, 2012); the latter is prominent in most engineering cases whereby an adverse gradient is present due to deceleration of the velocity field (dynamical reasons) around flow expansion or artificial perturbation in the flow field (Talstra, 2011). In the case of flow separation, both the wall friction and pressure gradient are in opposition to the flow's direction, which stops the development of the boundary layer thereby causing the flow rate near the wall to reduce to zero or even turn into a return flow (changes sign) (Talstra, 2011; White, 2009). The point at which the flow rate changes sign is what is referred to as the separation point or stagnation point. This point, however, is highly influenced by the flow geometry, wall roughness and flow conditions (e.g., turbulence) (Talstra, 2011).

Flow separation can occur in both laminar and turbulent flows, meaning any Reynolds number where boundary layers are present (Talstra, 2011). Of particular interest here is the concept of the boundary layer, as Simpson (2003) states that (vertical) flow separation occurs when the boundary layer detaches from the associated solid wall (bed). A boundary layer is a specific region, directly adjacent to the confining wall, where the flow is slower than that of the main flow. The thickness of this boundary layer depends on the equilibrium between the counteracting forcing terms, namely pressure gradient and wall shear stress. Under a favourable pressure gradient – where the pressure points in the mean flow direction – the boundary layer becomes narrow because of the large wall shear stress and velocity gradient, hence flow attachment (Figure 3a). On the other hand, under an adverse pressure gradient – where the pressure points against the flow direction – the opposite would happen which causes the boundary layer to thicken to become "infinitely wide", unstable (Talstra, 2011) and eventually detaches from the flow, hence flow separation (Figure 3b). Flow separation is also often accompanied by a turbulent wake (White, 2009).
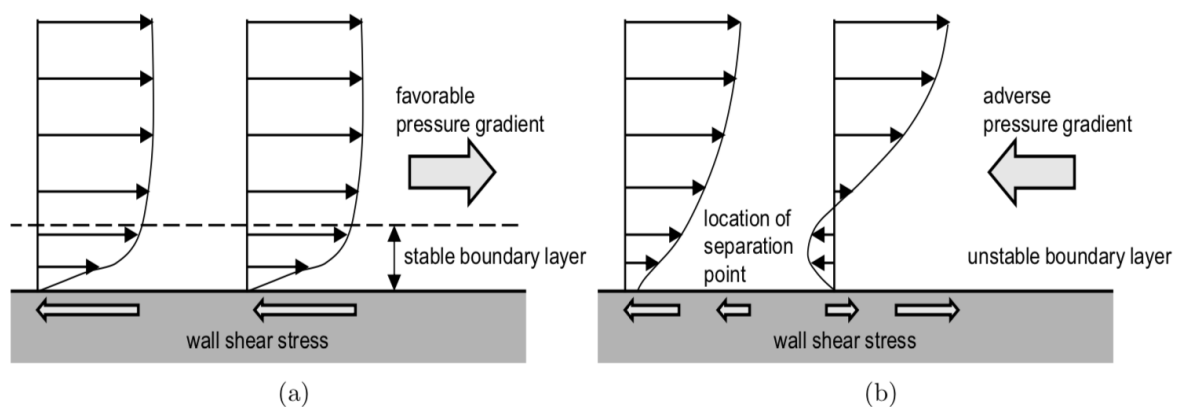
Figure 3: The effect of pressure gradient on boundary layer equilibrium visualised a) favourable pressure gradient and stable boundary layer, b) adverse pressure gradient and separating boundary layer. Obtained from Talstra (2011).

Flow separation phenomena result in the formation of a high velocity difference between the incoming flow and the separation area, leading to significant turbulence and, in some cases, the creation of a recirculation zone (van Prooijen et al., 2005). This shear induces the transfer of streamwise momentum through large-scale eddies. The conservation of mass, combined with this momentum transfer gives rise to the emergence of a fluid recirculation zone, often referred to as the primary recirculation or primary gyre which is steady in confined flows (with sidewalls) (Uijttewaal et al., 2001). The large-scale eddies or 2DCS at the interface between the main inflow and the recirculation zone is what constitutes the so-called mixing layer which enhances the diffusivity of turbulence and momentum transfer at this region, from the high-velocity side to the low-velocity side, gradually reducing the velocity difference (Nieuwstadt et al., 2016; Talstra, 2011). The inception of 2DCS associated with the mixing layer is called vortex shedding and they grow in size and energy in streamwise direction before dissipating. In certain cases, a secondary gyre, flowing in the opposite direction to the primary one, may also form. The size of the gyre is commonly measured by the reattachment length, which represents the distance from the separation point to the point where the flow reattaches to the wall (Talstra, 2011; Uijttewaal et al., 2001). This is illustrated in Figure 4.
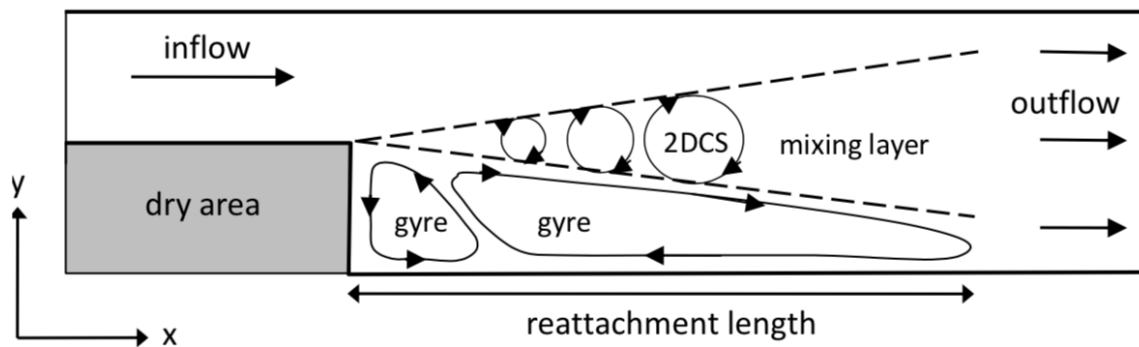
Figure 4: Schematization of a recirculation zone and the large-scale eddies at the interface of the main inflow and the recirculation zone (mixing layer), downstream of a separation point (top view). Obtained from Talstra (2011).

2.4. Current knowledge state

A recent field observation on the scour holes landward of the Eastern Scheldt storm surge barrier was performed by Broekema et al. (2018). The observations revealed that when the lateral velocity gradient is significant, the vertical flow separation over the sloping bed of the scour hole may be suppressed. This phenomenon was attributed to the conservation of potential vorticity and horizontal contraction of the flow, which can lead to a local acceleration of the flow that counteracts the adverse pressure gradient responsible for separating the boundary layer from the bed (Broekema et al., 2018). Furthermore, a self-amplifying scour mechanism was identified. Lateral velocity gradients lead to high velocities near the bed in scour holes through horizontal flow contraction, which amplifies erosion. As the contraction is directly proportional to the increase in (scour) depth, it maintains the scouring potential, hence the self-amplifying mechanism (Broekema et al., 2018). It was concluded that the character of the flow is determined by the combined effect of the horizontal and vertical flow structure, although the interaction is still being investigated.

From Broekema et al. (2018), it was postulated that the lateral velocity gradient was one of the underlying causes to flow attachment. Hence, in another study, Broekema et al. (2019) further investigated this notion through a physical flume experiment resembling a flow downstream of a hydraulic structure, where a flow is constricted at one side of the flume upstream (to induce flow non-uniformity) of a linearly sloping bed (resembling the scour) that is steep enough to ensure flow separation. The obstruction and its distance to the edge of the slope (resembling bed protection) control the magnitude of the lateral velocity gradient; this is based on the understanding that the development of a mixing layer which widens in the streamwise direction gradually reduces the lateral velocity gradient (Talstra, 2011; van Prooijen & Uijttewaal, 2002).

From the experiment, it was ascertained that two distinct flow states are present, namely a) vertical flow separation and horizontal divergence as well as b) vertical flow attachment and horizontal convergence. This is illustrated in Figure 5. In agreement with Broekema et al. (2018), the transition between flow attachment to flow separation was found to be highly influenced by the magnitude of the lateral gradient in the streamwise velocity, whereby the steeper it is the more likely for flow attachment to occur. Additionally, the former flow state, flow attachment and horizontal convergence, was found to have higher bed shear stress compared to the latter (Broekema et al., 2019), highlighting that high streamwise momentum can be advected to the bed and enhances scour potential.

Broekema et al. (2019) noted that horizontal convergence and flow attachment in this experiment cannot be fully attributed solely to potential vorticity nor the adverse pressure gradient to explain the transition between the flow states but rather to the localized behaviour of the flow. Specifically, the interaction between the lateral velocity

gradient and the turbulence induced by the slope that promotes the growth of the horizontal recirculation zone, so large that it constricts the high-velocity side of the mixing layer.
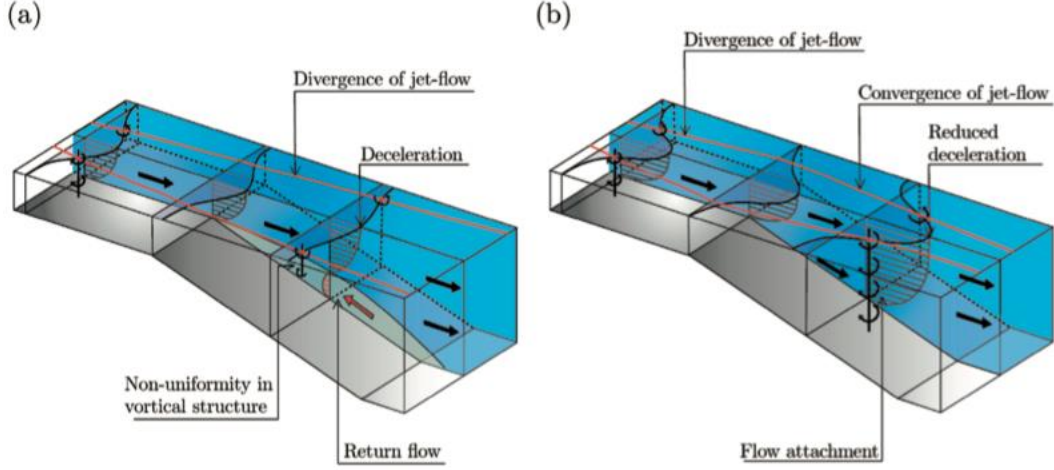
Figure 5: Conceptualization of the two flow states observed on the field. a) Vertically separating and diverging in the horizontal plane; b) vertically attaching and converging in the horizontal plane. Obtained from Broekema et al. (2018).

2.5. Reynolds-Averaged Navier-Stokes (RANS)

The RANS turbulence model is a method to model turbulent flows instead of directly resolving the Navier-Stokes equations. RANS is considered a statistical approach or description of turbulence. It analyzes the flow in two components, namely the mean and fluctuations, or the so-called Reynolds decomposition. The concept of Reynolds decomposition is explained further below, where for stationary turbulence (statistically steady), the flow variable of interest (e.g., $\phi(x,t)$) can be represented by the sum of its mean (e.g., $\bar{\phi}(x,t)$), which is a time-average over a certain sampling period, and the fluctuations around the mean (e.g., $\phi'(x,t)$).

$$\phi(x,t) = \bar{\phi}(x,t) + \phi'(x,t) \qquad (5)$$

This decomposition, when incorporated into the instantaneous (momentum) Navier-Stokes equation, results in a set of new averaged equations that introduce new unknown quantities, namely the Reynolds stresses.

$$\nabla \cdot \bar{\boldsymbol{u}} = 0 \qquad (6)$$

$$\rho \left[\frac{\partial \bar{\boldsymbol{u}}}{\partial t} + (\bar{\boldsymbol{u}} \cdot \nabla) \bar{\boldsymbol{u}} \right] + \rho \frac{\partial}{\partial x_j}(\overline{u_i' u_j'}) = -\nabla \bar{p} + \mu \nabla^2 \bar{\boldsymbol{u}} \qquad (7)$$

As can be seen above, this introduces an additional term $\overline{u_i' u_j'}$, known as the turbulent stress tensor or more commonly known as the Reynolds stress tensor. Rearranging the averaged momentum equation yields the following:

$$\rho \left[\frac{\partial \overline{\boldsymbol{u}}}{\partial t} + (\overline{\boldsymbol{u}} \cdot \nabla)\overline{\boldsymbol{u}} \right] = -\nabla \overline{p} + \nabla_i \cdot \tau_{ij} \tag{8}$$

$$\text{Where the viscous stress, } \tau_{ij} = \mu \left(\frac{\partial \overline{u}_i}{\partial x_j} + \frac{\partial \overline{u}_j}{\partial x_i} \right) - \rho(\overline{u_i' u_j'}) \tag{9}$$

The whole procedure presented above resulted in a total of six additional unknown independent stresses introduced into the governing Navier-Stokes equations due to the averaging process, resulting in more unknowns than equations (Hanjalic, 2004). Hence, the equations presented above are not a closed system; the so-called turbulence closure problem (the number of unknowns is larger than the number of equations) (Hanjalic, 2004; Molland & Turnock, 2007). To represent these stressors in terms of known values, a closure process is thus necessary. Turbulence closure modelling, a technique commonly used, uses a set of mathematical equations to provide values to the unknown variables and offers an engineering approximation of the effect of turbulence on the mean-flow field (Hanjalic, 2004; Molland & Turnock, 2007; Pereira et al., 2021). This particular approach makes RANS a more computationally efficient choice than LES or DNS as it models both large and small eddies simultaneously instead of resolving them; hence its popularity in industrial and engineering applications. However, this comes at a cost of modelling accuracy, since all turbulence scales are equally represented and time-averaged (Hanjalic, 2004; Molland & Turnock, 2007; Pereira et al., 2021). Hence, the applicability of RANS can be limited (Pereira et al., 2021).

3. Numerical Methodology

In this section, the methodology employed in this study is elaborated. It follows the procedure of CFD analysis as proposed by Molland and Turnock (2007) as well as Faragher (2004), whereby the overall process is defined into three main stages, namely:

1) Pre-processing: this includes understanding the problem, specifying the geometry, turbulence closure model, computational mesh, initial and boundary conditions
2) Solution: this includes running the CFD solver and monitoring for convergence
3) Post-processing: this may include needing to refine the mesh, perform sensitivity studies, analysis and interpretation of the obtained solution.

3.1. Model selection

This study will be performed with the open-source CFD software OpenFOAM (Open-source Field Operation and Manipulation). It employs the finite volume method (FVM) which is a three-dimensional application of the finite difference method, whereby the problem domain is discretised into finite volumes or cells in which the integral form of the conservation laws (e.g., mass, energy) – or in this case the partial differential RANS equations expressed in integral forms – are applied in each of the cells such that enough algebraic equations are available to approximate the physical parameters at the nodal locations of the finite volumes (McDavid, 2001; Neill & Hashemi, 2018; Sharif Ahmadian, 2016). Better accuracy and stability can be achieved when solving equations in their integral form, especially when the problem domain contains steep gradients (i.e., significant derivatives) (Neill & Hashemi, 2018). Admittedly, many commercial CFD software packages, such as ANSYS, CFX and COMSOL Multiphysics are available. However, this study builds upon a model that has been partially developed with OpenFOAM; thereby justifying the software selection.

3.2. Model Geometry

The computational domain used in this study is consistent with the flume laboratory experiment setup of Broekema et al. (2019), which is illustrated in Figure 6. The glass flume is 14 m long, 0.4 m wide and 0.27 m deep (Broekema et al., 2019). At the inlet, a turbulent flow of 11 l s^{-1} (Q$_{in}$) with Reynolds number $Re = 3 \times 10^4$ and Froude number $Fr = 0.4$ is imposed (Broekema et al., 2019).

Two distinct features of the flume are the 1) horizontal obstruction on one side of the flume which gradually spans up to half the width of the flume and 2) a linearly sloping bed downstream of the obstruction. The former feature imposes lateral nonuniformity in the streamwise velocity of the flow whose magnitude is based on how far it is distanced from the upstream edge of the slope (L_D). This is based on the understanding that the lateral velocity gradient gradually reduces as the mixing layer widens in the streamwise direction (Talstra, 2011; van Prooijen & Uijttewaal, 2002). The second feature ensures that

the slope steepness, i_b, is steep enough such that flow separation would have occurred in the absence of the horizontal obstruction, hence a laterally uniform flow (Broekema et al., 2019). Upstream of the slope, the water depth, d_u, is 0.12 m whereas the downstream water depth, d_d, is approximately 0.27 m. The channel upstream of the slope is shallower due to the bed being placed 0.15 m higher than its downstream counterpart, which sees increase in water depth over the sloping bed.

For consistency's sake, this study also uses a coordinate system like that of Broekema et al. (2019), where the x-direction denotes the streamwise direction of the flow, the y-direction denotes the lateral direction perpendicular to the flow, and the z-direction denotes the vertical direction, perpendicular to the horizontal plane.
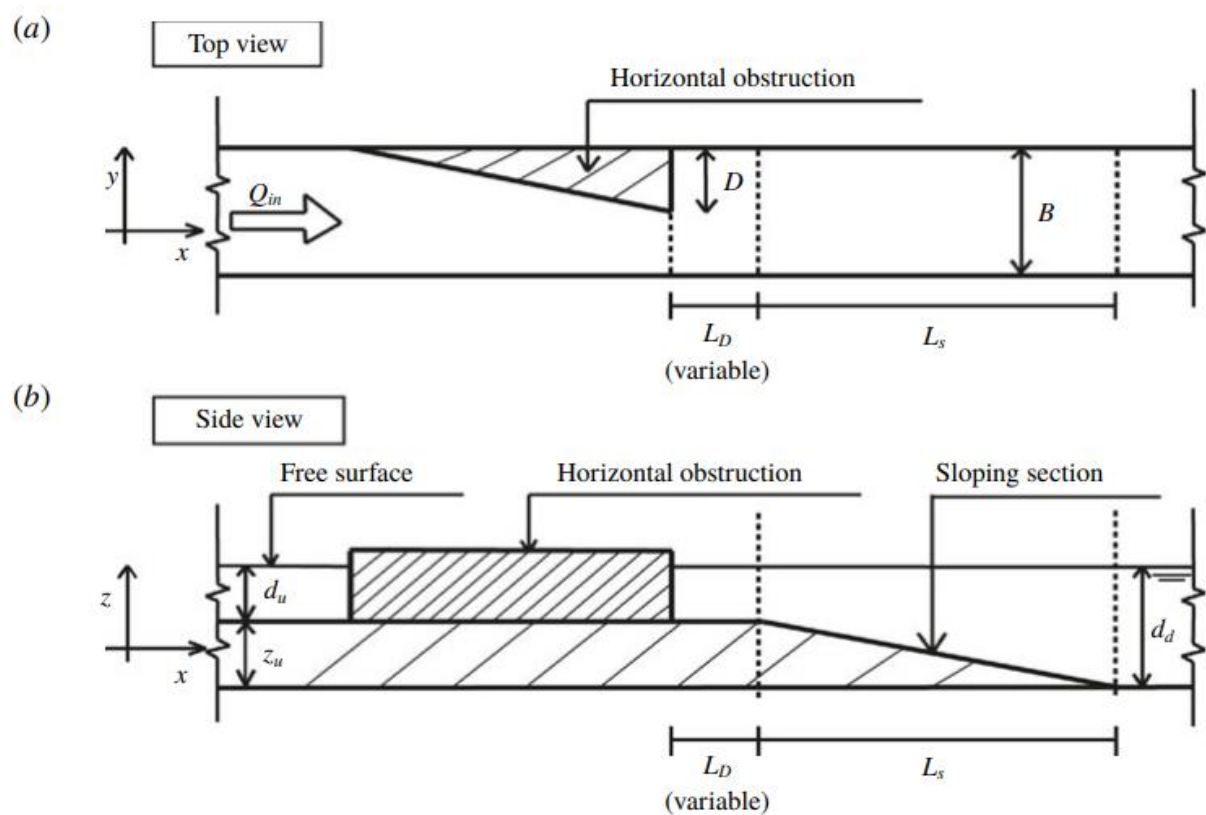
Figure 6: a) top view and b) side view of the flume experiment. The flume width, B, is 0.4m and the maximum width of the horizontal obstruction, D, is 0.5B. L_D and L_u, are the distance between the horizontal obstruction and the upstream edge of the slope and the length of the sloping section, respectively. Water depth d_u = 0.12 m, d_d = 0.27 m and bed level z_d = 0.15 m. Obtained from Broekema et al. (2019).

3.3.   Boundary Conditions

Boundary conditions were imposed at the inlet, outlet, and walls of the computational domain. At the inlet, a constant velocity u, 0.25 m/s, in the streamwise-direction is imposed, along with a kinematic viscosity v, 10^{-6} m²/s, equivalent to the kinematic viscosity of water at 20°C, to achieve a Reynolds number of $Re = 3 \times 10^4$; similar to that of the experiment conditions outlined in section 3.2. In OpenFOAM, this is defined with a *fixedValue* (Dirichlet) boundary condition, meaning constant value throughout time or iterations. At the outlet, the *zeroGradient* (Neumann) boundary condition is applied for

the velocity, allowing the flow to freely adjust its velocity as it leaves the computational domain through the outlet boundary.

For the velocity boundary conditions, the sidewalls and the bed were considered no-slip whereas the water surface was considered a slip surface. Consistent with the definition of no-slip boundary conditions, the walls were set to no-slip based on the presumption that the fluid layer's velocity and the boundary's velocity are the same; hence no movement or slip between them. In other words, the fluid velocity is zero at the wall (Koshizuka et al., 2018; Rapp, 2017). The opposite applies to the slip boundary condition, where the velocity at the boundary is non-zero.

At the walls and the inlet, a *zeroGradient* boundary condition is applied for the pressure boundary condition since no external pressure in the computational domain is imposed. This allows for the pressure to adjust freely to the flow conditions inside the domain. Regarding the former, this can be also explained by the fact that a fixed wall physically does not exert any force on the fluid, therefore imposing the *zeroGradient* boundary condition on the walls implies that there is no flux of pressure across the walls. At the outlet, a *fixedValue* of 0 is imposed for the pressure; often this is interpreted as a reference value such as the atmospheric pressure. Additionally, the turbulent kinematic viscosity (v_t) at the outlet and inlet is calculated from the turbulence closure model while those at the vicinity of the walls are calculated using a wall function, as will be explained further in Section 3.8. The boundary conditions applied for the simulation are summarized in Table 1.

Table 1: Overview of the modelling boundary conditions.

Boundary	u (m/s)	P/ρ (m²/s²)	v_t (m²/s)
Inlet	fixedValue (0.25)	zeroGradient	Calculated
Outlet	zeroGradient	fixedValue (0)	Calculated
Free surface	slip	zeroGradient	NutUBlendedWallFunction
Side walls	noSlip	zeroGradient	NutUBlendedWallFunction
Bottom wall	noSlip	zeroGradeint	NutUBlendedWallFunction

3.4. Computational mesh

The generation of mesh alludes to subdividing the whole flow domain into a discretised continuous finite volume, or the so-called grid or mesh. In performing a CFD analysis, the mesh-generation process needs to balance: 1) the need to improve solution accuracy by using a higher number of cells in certain regions of the flow where the flow parameters change rapidly, 2) the need to have a domain large enough such that the boundary conditions will not impact the solution negatively and 3) the need to obtain a solution within a feasible time frame (Molland & Turnock, 2007).

The meshing of the computational domain, as elaborated in Section 3.2, was accomplished using the *blockMesh* utility from OpenFOAM. This utility generated a structured rectangular hexahedral mesh throughout the domain. The computational domain was discretized into eight distinct blocks to facilitate the meshing process (see Figure 7). The mesh density was appropriately biased to allocate a higher concentration of cells in the regions of interest, namely after the horizontal obstruction and over the slope (block 2 – 5 in Figure 7 and Figure 8). These areas are critical as they exhibit significant flow gradients where flow separation or attachment occurs. The implementation of mesh biasing serves the dual purpose of optimizing computational resources and accurately capturing the flow characteristics of interest. To minimize the simulation time, the length of the computational domain is shortened to 8 m instead of 14 m, encompassing 4 m downstream and upstream of the upstream edge of the slope.
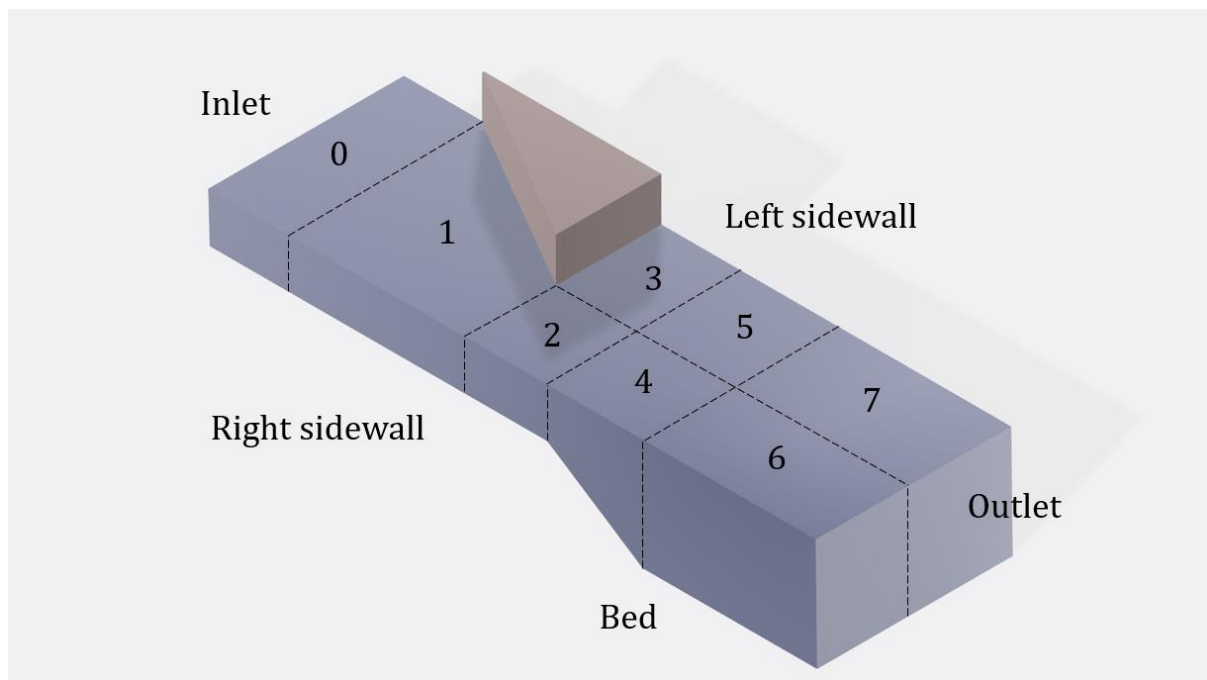
Figure 7: The discretization of the computational domain into eight different blocks including the name of the faces. Figure is not to scale.

Furthermore, the domain was subdivided into six divisions, each assigned specific names for their corresponding faces: inlet, outlet, right and left sidewall, upper-wall (representing the water surface), and lower-wall (representing the bottom surface or bed); shown in Figure 7. It is worth noting that the water surface employs the so called rigid-lid assumption, whereby the deformation of the water surface is not modelled.
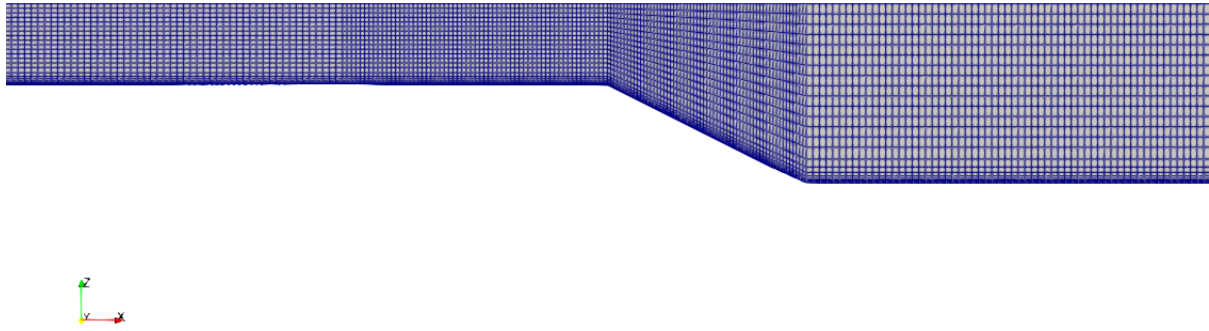
Figure 8: Side view of the computational mesh showing higher mesh density after the horizontal obstruction and over the slope given these are the flow regions of interests.

Four different mesh resolutions were tested to assess the grid independence as detailed in Section 4.1. These resolutions, presented in Table 2, undergo successive refinements. The eight distinct blocks were interconnected and require an equal number of cells in the spanwise and vertical direction between the blocks. Consequently, the refinement in this study primarily stems from enhancing the grid resolution in these directions, while maintaining a constant cell size of 1 cm in the streamwise direction, except for the biased portion, which is approximately 0.5 cm, providing a finer resolution around the slope.

In the coarse mesh resolution, upstream of the obstruction, the unit grid cells measure 1 cm in the spanwise and vertical direction (block 0 in Figure 7). As the channel narrows due to the obstruction, the spanwise cell size reduces to 0.5 cm and remains consistent further downstream (block 1-7 in Figure 7). However, as the channel gets deeper, the vertical resolution becomes coarser, reaching a cell size of 2.25 cm in the deeper part of the channel (block 4-7 in Figure 7). Therefore, to address the coarser vertical grid resolution, refinements were implemented in the vertical grid, resulting in the medium-resolution mesh. This mesh refines the vertical grid, with a cell size of 1 cm in the deeper part of the channel and 0.44 cm in the shallow part upstream of the slope.

The fine-resolution mesh further refines the vertical grid to achieve a unit grid cell size of approximately 0.65 cm and 0.29 cm in the deep and shallow part of the channel, respectively; bringing it closer to the spanwise resolution. It was later found that the result between the medium and fine mesh did not exhibit significant improvement, suggesting that grid independence in the vertical direction had been achieved. Finally, the extra-fine mesh refines the spanwise grid of the fine mesh, resulting in unit grid cell sizes of 0.67 cm upstream of the obstruction and 0.33 cm downstream.

Table 2: Grid or mesh resolutions and the respective number of cells tested to achieve grid independence.

Grid type	Number of Cells
Coarse	609,600
Medium	1,447,200
Fine	2,082,800
Extra Fine	3,050,400

3.5. Numerical Algorithm

In this study, two numerical ($p - u$ coupling) algorithms to solve the RANS equations were evaluated, namely the SIMPLE (Semi-Implicit Method for Pressure-linked equations) (Caretto et al., 1973) and PIMPLE algorithm. The PIMPLE algorithm is a combination of the classical SIMPLE and PISO (Pressure Implicit Splitting of Operators) (Issa, 1986); hence the merged acronym. The SIMPLE algorithm was intended for steady state simulations, where a pressure correction term is used while the velocity corrections are neglected. SIMPLE requires a lot of iterations to arrive at a convergent solution. On the other hand, the PISO algorithm was designed for transient simulations and repeatedly solves the pressure correction equation, updating the velocities in the process with velocity correction. Hence, the PIMPLE algorithm, being a combination of the two, is best imagined as the SIMPLE algorithm being applied for every time step. In other words, the PIMPLE algorithm allows for specifying the number of outer corrector loops or iterations to be performed within each time step before progressing to the next, continuing until the final time step is reached. This unique characteristic of the PIMPLE algorithm enables the use of larger time steps and Courant numbers greater than one without compromising the stability of the solution.

3.6. Solver Details

The numerical solution of the equations involved the utilization of various approaches within the solver. In terms of time discretization, the backward scheme, a second-order implicit time scheme, was employed for the PIMPLE algorithm, while a steady-state time scheme was used for the SIMPLE algorithm, as there is no time derivative involved.

Both the PIMPLE and SIMPLE solvers employed the "Gauss linear" numerical approach for resolving the gradients. The term "Gauss" refers to the finite volume discretization based on Gaussian integration, while "linear" represents the interpolation scheme, specifically linear interpolation or central differencing. To address the Laplacian schemes, the "Gauss linear corrected" scheme was chosen. For the pressure solution, the Diagonal Incomplete-Cholesky (DIC) Gauss Seidel smoother in combination with the Geometric Algebraic Multi-Grid (GAMG) solver was applied. As for the other quantities, such as ε, ω and velocity components, the smoothSolver with Symmetric Gauss Seidel smoother was applied. Furthermore, all convective terms were discretized using second-order schemes.

Within the PIMPLE algorithm, the value of *nCorrectors* was set to 2, indicating that the pressure equation and momentum corrector were solved twice for every time step. The number of *nNonOrthogonalCorrectors* was set to 1 to correct for non-orthogonality by repeating the pressure equation once. Under-relaxation with a value of 0.9 for all variables was used in both algorithms for stability. The maximum number of iterations for the SIMPLE algorithm was set to 10,000 for all cases, as a preliminary run of 50,000 iterations revealed that convergence did not improve after 10,000 iterations. For the PIMPLE algorithm, the time-step of the simulation were indirectly specified through a maximum Courant number as OpenFOAM automatically adjusted the time-step in accordance with changes in field values and local mesh size. A Courant number of 3 was used for all cases. One additional simulation was performed with a Courant number of 0.7 to assess its influence on the solution.

3.7. Turbulence closure model

The utilization of turbulence closure models is an integral part of implementing a RANS turbulence model, as was explained above in section 2.5. In this study, a pair of two-equation turbulence closure models will be tested. These are the $k - \varepsilon$ and $k - \omega$ SST, which are argued to be some of the most used turbulence models in engineering practices (Brown et al., 2016; Norton et al., 2010). These turbulence closure models are based on the eddy-viscosity concept, where the Reynolds stresses are based on the Boussinesq eddy viscosity assumption; meaning that they are approximated similarly to that of the viscous stress of an isotropic fluid (Baker et al., 2019; Hanjalic, 2004; Lü et al., 2021), whereby the Reynolds stresses are proportional to the mean rates of deformation hence it carries the isotropic assumption (Versteeg & Malalasekera, 2007):

$$\tau_{ij} = \rho \overline{(u_i' u_j')} = \mu_t \left(\frac{\partial \bar{u}_i}{\partial x_j} + \frac{\partial \bar{u}_j}{\partial x_i} \right) - \frac{2}{3} \rho k \delta_{ij} \qquad (10)$$

Where μ_t is the eddy or turbulent viscosity, k being the turbulent kinetic energy per unit mass and δ_{ij} being the Kronocker delta. A brief description of these turbulence closure models is given below.

3.7.1. The $k - \varepsilon$ model

The $k - \varepsilon$ model (Launder & Spalding, 1974) is among the most widely employed turbulence closure model. It is a semi-empirical transport equation that assumes isotropic turbulence, based on the turbulent kinetic energy, k, and dissipation rate, ε (Hanjalic, 2004). Its simplicity makes it robust in the sense that a flow solution should be found, but the model tends to generally underperform in transitional turbulence or adverse pressure conditions and is often unable to accurately replicate flow behaviour close to the flow separation (Brown et al., 2016; Lü et al., 2021; Wilcox, 2012). Additionally, it does not perform well near the wall or the viscous boundary layer (Brown

et al., 2016) which may require for instance a wall function or near-wall treatment as will be discussed in section 3.8.

3.7.2. The shear-stress transport (SST) $k - \omega$ model

The $k - \omega$ SST model (Menter, 2012) is a mix of the $k - \varepsilon$ and $k - \omega$ models. It addresses the weakness of the basic $k - \omega$ model for being overly sensitive to the free stream while maintaining its advantage in the near-wall regions. This was done using an empirical blending function, resulting in the $k - \omega$ model being applied for near-wall treatment and the $k - \varepsilon$ model in the free stream (Brown et al., 2016). Overall, this results in enhanced resolution of the boundary layer of viscous flow (Menter, 2012). Since it is derived from the standard models mentioned earlier, the $k - \omega$ SST model also assumes isotropic turbulence (Menter, 2012; Brown et al., 2016).

3.8. Near-wall Treatment

Accurate modelling of near-wall physics may require the implementation of near-wall treatments. The $k - \varepsilon$ model, for instance, cannot be applied in regions where viscous effects are dominant but can be overcome with wall functions (Lü et al., 2021).

In near-wall flows, the position within the boundary layer is commonly expressed in nondimensional form y⁺. It represents the distance normal to the wall and is associated with the local Reynolds number; hence the magnitude of y⁺ also depends on the Reynolds number (Molland & Turnock, 2007; Nieuwstadt et al., 2016; Pope, 2000). The y^+ is calculated as $y^+ = yu_\tau/v$, where u_τ is the wall friction velocity derived from the wall shear stress (τ_w) as the velocity at the wall is zero ($u_\tau = \sqrt{\tau_w/\rho}$,) with y and v being the absolute distance from the wall and the kinematic viscosity, respectively. Additionally, the variation of dimensionless tangential velocity close to the wall is expressed as $u^+ = u/u_\tau$. The near-wall flows exhibit a multi-layered structure following the universal law of the wall and the value of y^+ characterizes the flow regime near the wall. This structure consists of the laminar (viscous) sublayer ($y^+ < 5$) close to the wall where the viscous stress dominates; the buffer layer ($5 < y^+ < 30$) where the viscous and turbulent stress are roughly equal; the logarithmic (inertial) layer ($30 < y^+ < 200$) where the turbulent stress dominates (Molland & Turnock, 2007; Nieuwstadt et al., 2016; Pope, 2000).

To address near-wall physics, two approaches are commonly employed: wall functions and near-wall modelling strategies. Wall functions utilize empirical equations fitted to the near-wall flow behaviour to reproduce the flow behaviour in the viscous layer and the logarithmic layer using linear and logarithmic function, respectively. At the viscous sublayer, the fluid is dominated by the viscous effect while the Reynolds shear stress is negligible, hence the linear relation $u^+ = y^+$. In the logarithmic layer, the turbulence stresses dominate which varies logarithmically with distance y, hence the logarithmic function $u^+ = \ln{(Ey^+)}/\kappa$; where κ is the von Karman constant defined as 0.41 and E being an empirical wall roughness coefficient defined as 9.8 in OpenFOAM. Examples of

such wall functions include the standard wall function (Launder & Spalding, 1974) and the non-equilibrium wall function (Kim et al., 1995).

On the other hand, near-wall modelling employs high-resolution meshes in close proximity to the wall, enabling the boundary layer profile to be resolved all the way to the wall. In this approach, the first cell centroid is ideally placed within the viscous sublayer (preferably $y^+ < 1$) (Lü et al., 2021). The near-wall region is characterized by high velocity gradient due to the no-slip boundary condition at the wall, resulting in a velocity profile that transitions from zero at the wall to the free stream value away from the wall. Consequently, it is common practice to gradually refine the mesh size near the wall, ensuring that the modelled flow velocities that are linearly interpolated between cell centroids capture the velocity variations and steep gradients accurately. This is illustrated in Figure 9. Near-wall modelling strategies often require significantly higher computational time due to the higher cell count and finer resolution near the wall. Additionally, the increased mesh resolution near the wall can lead to cells with high aspect ratios and skewness, potentially compromising mesh quality and overall solution accuracy.
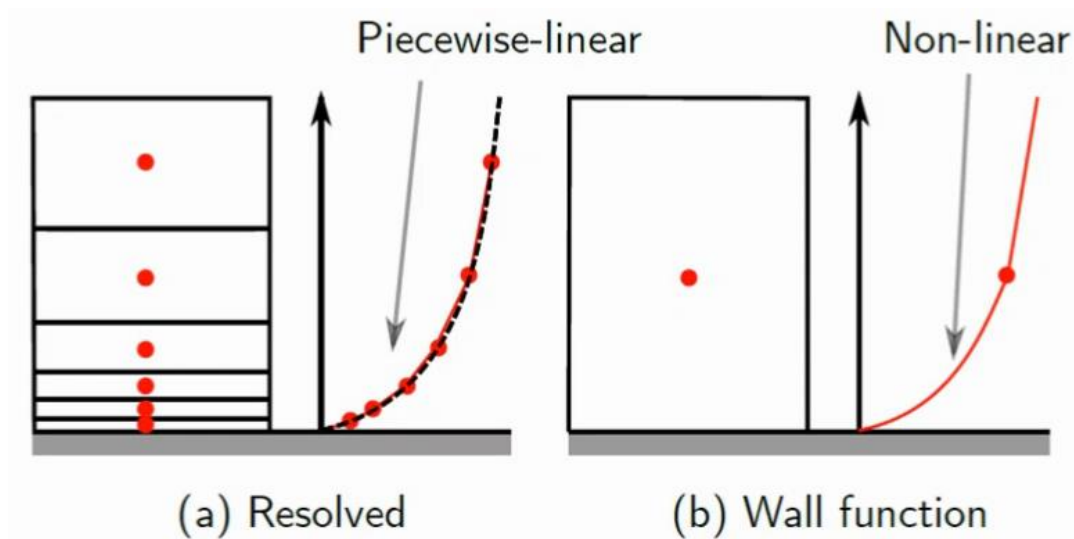
Figure 9: Two different methods of addressing the near-wall physics. (a) Resolved through near-wall modelling with high - resolution meshes near the wall; (b) Wall function. The red dots inside the squares represent the cell centroids. Obtained from Fluid Mechanics 101 (2019)

In this study, both near-wall treatments are considered. The near-wall modelling strategy was employed in the vertical direction for all mesh resolutions, as depicted in Figure 10, by inflating the mesh in the vertical direction for all mesh resolutions. Wall function was applied to the sidewalls, except for the case of medium mesh with side-wall refinements where the side walls are also inflated. The so-called *nutUBlendedWallFunction* wall function in OpenFOAM was used which provides turbulent kinematic viscosity from the velocity and a blending method between the laminar sub-layer and the log region. The inflated side walls were implemented using the *snappyHexMesh* utility from OpenFOAM, as illustrated in Figure 11, specifically for the mesh with side-wall refinements. In this specific mesh configuration, mesh biasing around the slope as explained in Section 3.4

was omitted due to challenges faced by the *snappyHexMesh* utility in incorporating the inflated sidewall layers when mesh biasing was included.
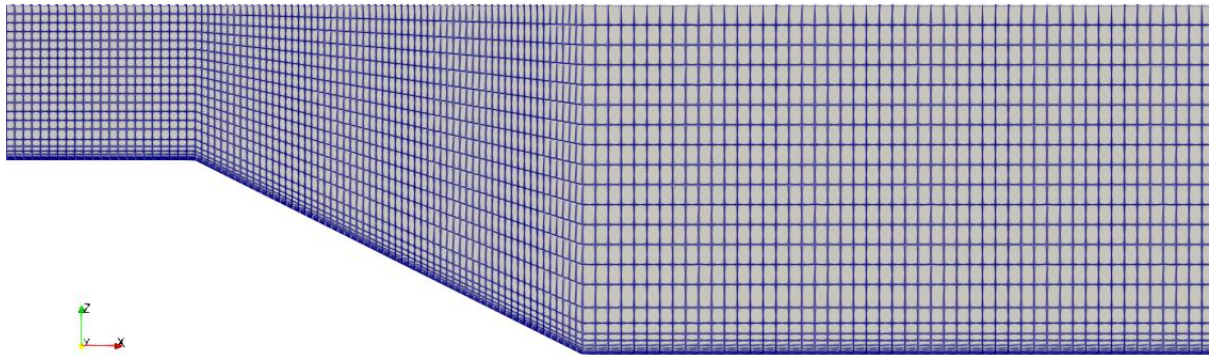
Figure 10: Inflated mesh on the z-direction for all the mesh
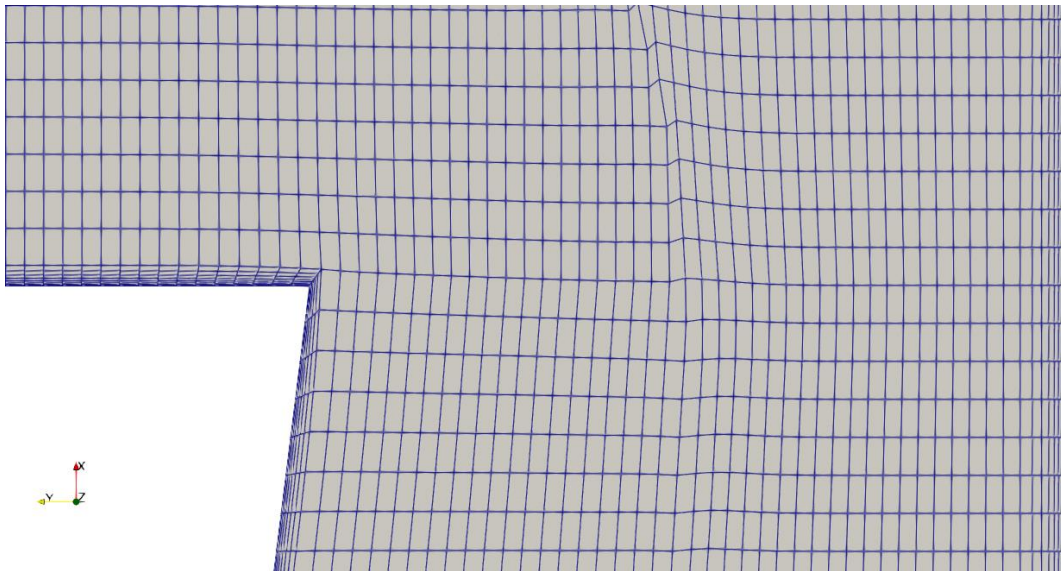
Figure 11: Side-wall refinement using OpenFOAM utility snappyHexMesh, for the medium mesh with sidewall refinements.

3.9.   Monitoring Convergence

Convergence in numerical processes can be defined as the alignment of the numerical solution with the actual solution of a partial differential equation, given specific initial and boundary conditions (Faragher, 2004; Molland & Turnock, 2007; Tu et al., 2018). It is characterized by two key aspects: stability and consistency. Consistency refers to the accuracy of the approximation of the partial differential equations, leading to reduced truncation errors and enhanced precision with grid or time-step refinement. Truncation error measures the accuracy of the approximation as well as the rate at which the error lowers with further grid or time-step refinement (Tu et al., 2018). Stability, on the other hand, pertains to the behaviour of errors. If the errors do not diverge during computations, the numerical solution is deemed stable. In the context of iterative

techniques, stability corresponds to a non-diverging (converging) solution (Tu et al., 2018).

In a CFD analysis, the system often iteratively solves the aforementioned algebraic equations; hence, the term iterative convergence. This iterative convergence is tracked by monitoring the imbalances or errors in the system, commonly referred to as residuals. As the numerical process progresses, the residuals should decrease up to the defined threshold or tolerance to achieve satisfactory convergence (Tu et al., 2018). Hence, a convergence criterion was established for this study, where the solver was considered converged when the residuals of variables such as the velocity components, pressure, and turbulent kinetic energy, just to name a few, reached magnitudes on the order of $O(10^{-6})$.

3.10. Simulation cases

To address the research question, outlined in Section 1.3, a series of simulations were conducted with the two selected turbulence closure models under two different slope steepness and varying distance L_D – all other simulation domain aspects remained the same. In t

With a steepness of 1:2 and L_D of 0.4 m, flow attachment was observed in the experiment but not when L_D was 0.7 m (Broekema et al., 2019). As this was the only scenario in which flow separation occurs in laterally non-uniform flow (Broekema et al., 2019), further investigation of these two cases was performed to shed light on how flow attachment is affected by the upstream flow field and allows for analysis of the flow structure. Following the nomenclature introduced by Broekema et al. (2019), these cases are denoted as S2A (slope 1:2, attached flow) and S2D (slope 1:2, detached flow). Additional runs were also performed under a different slope angle, 1:4, referred to as case S4A (slope 1:4, attached flow) to examine the influence of slope steepness on the flow field and flow attachment. These abbreviations are summarized in Table 3. These geometric configurations are analogous to a select few cases investigated by Broekema et al. (2019) so that a direct comparison between this study and theirs can be made. All in all, the investigated cases provided a systematic approach to investigating the influence of varying slope steepness and distance of obstruction to the upstream edge of the slope on the flow field at the slope.

Table 3: Overview of the selected number of cases and its abbreviations. Case S2A (read: slope 1:2, attached flow), S4A (read: slope 1:4, attached flow), S2D (read: slope 1:2, detached or separated flow).

Slope steepness	L_D (m)	Vertical flow state	Abbreviation
1 in 4 (14°)	0.4	Attached	S4A
1 in 2 (26.5°)	0.4	Attached	S2A
	0.7	Detached (separated)	S2D

A detailed overview of the simulation runs conducted with the SIMPLE and PIMPLE algorithms can be found in Table 4 and Table 5, respectively. For the simulations

performed with the SIMPLE algorithm, each turbulence closure model was tested across all mesh resolutions while simulations performed with the PIMPLE algorithm uses only the $k - \omega$ SST. This stems from the fact that the $k - \varepsilon$ model works only with $y^+ > 30$, which puts heavy reliance on wall functions to represent the near-wall flows. Versteeg and Malalasekera (2007) noted the inadequacy of using wall functions in situations involving boundary layer separation (e.g., due to adverse pressure gradients) whereby they emphasised that the log-law based wall functions do not yield accurate predictions of the velocity profile in such cases and recommended to directly resolve the viscous sublayer (Constantinescu et al., 2003). Moreover, it is acknowledged that the $k - \omega$ SST exhibits better performance than the $k - \varepsilon$ model when encountering adverse pressure gradient, enabling more accurate representation of flow separation (Hanjalic, 2004; Menter, 2012; Versteeg & Malalasekera, 2007; Wilcox, 2012). Since the PIMPLE algorithm takes significantly longer computational time to run, conducting a sensitivity analysis on the wall functions employed was not feasible within the time frame of this thesis. Hence, the $k - \omega$ SST model was used.

Table 4: Overview of the SIMPLE simulation runs, performed across all mesh resolutions.

No.	Turbulence closure model	Slope steepness	L_D (m)
1		1 in 2 (26.5°)	0.4
2	$k - \varepsilon$		0.7
3		1 in 4 (14°)	0.4
4		1 in 2 (26.5°)	0.4
5	$k - \omega$ SST		0.7
6		1 in 4 (14°)	0.4

Table 5: Overview of the PIMPLE simulation runs. All cases were performed with the $k - \omega$ SST.

No.	Mesh Resolution	Slope steepness	L_D (m)	Courant number
1			0.4	3
2			0.7	0.7
3	Medium	1 in 2 (26.5°)	0.7	3
4			0.8	3
5			1.0	3
6		1 in 4 (14°)	0.4	3
7		1 in 2 (26.5°)	0.4	3
8	Medium with side wall refinements		0.7	3
9		1 in 4 (14°)	0.4	3
10		1 in 2 (26.5°)	0.4	3
11	Fine		0.7	3
12		1 in 4 (14°)	0.4	3
13	Extra Fine	1 in 2 (26.5°)	0.4	3

4. Results

This chapter provides an overview of the result obtained using the PIMPLE algorithm. Simulations with the SIMPLE algorithm highlighted challenges in achieving convergence and accurately capturing the transient flow phenomena of interest. These difficulties were likely attributed to the inherent transient nature of the phenomena. These unsteady characteristics manifest as persistent fluctuations in the flow field from one iteration to the next, which prevents the residuals from reaching the desired level as the solution attempts to reach for a steady state that does not exist due to the inherently unsteady flow separation process. Results from the SIMPLE algorithm is presented in Appendix A. Consequently, the adoption of the PIMPLE algorithm, a transient solver, was deemed appropriate. The obtained results will be presented and discussed, with particular emphasis on comparing them with the available measurement data of Broekema et al. (2019).

4.1. Grid independence

One way to assess and confirm the accuracy of the model is to obtain solutions on grids that have undergone successive grid refinements (grid convergence) and ensure that the solution has not altered because of the subsequent refinements (Tu et al., 2018). In other words, the mesh must be refined to eliminate the errors resulting from the mesh design until the obtained results reveal no changes. As outlined in Table 2, several grid resolutions were considered. The obtained velocity data form each grid resolution is used as a metric for this grid independence study where the depth-averaged and time-averaged velocity data is compared with the measurements.

Looking at the time-depth-averaged velocity profile (Figure 12), it is apparent that the fine mesh closely resembles the measured data, as anticipated given the higher cell count and improved resolution. Here, case S4A is used as an example; other cases are presented in the Appendix B. However, a contrasting trend was observed when evaluating the time-averaged Mean Absolute Error (MAE) and Root Mean Square Error (RMSE) of the velocities over the domain where measurements were made (Table 6). Surprisingly, the errors exhibited a slight increase with each successive grid refinements from medium to fine for all cases, contrary to the expected trend of error reduction as observed in the depth-averaged velocity profile. This discrepancy suggests the presence of other contributing factors or errors that, when depth-averaged, mask the underlying error in the solution.
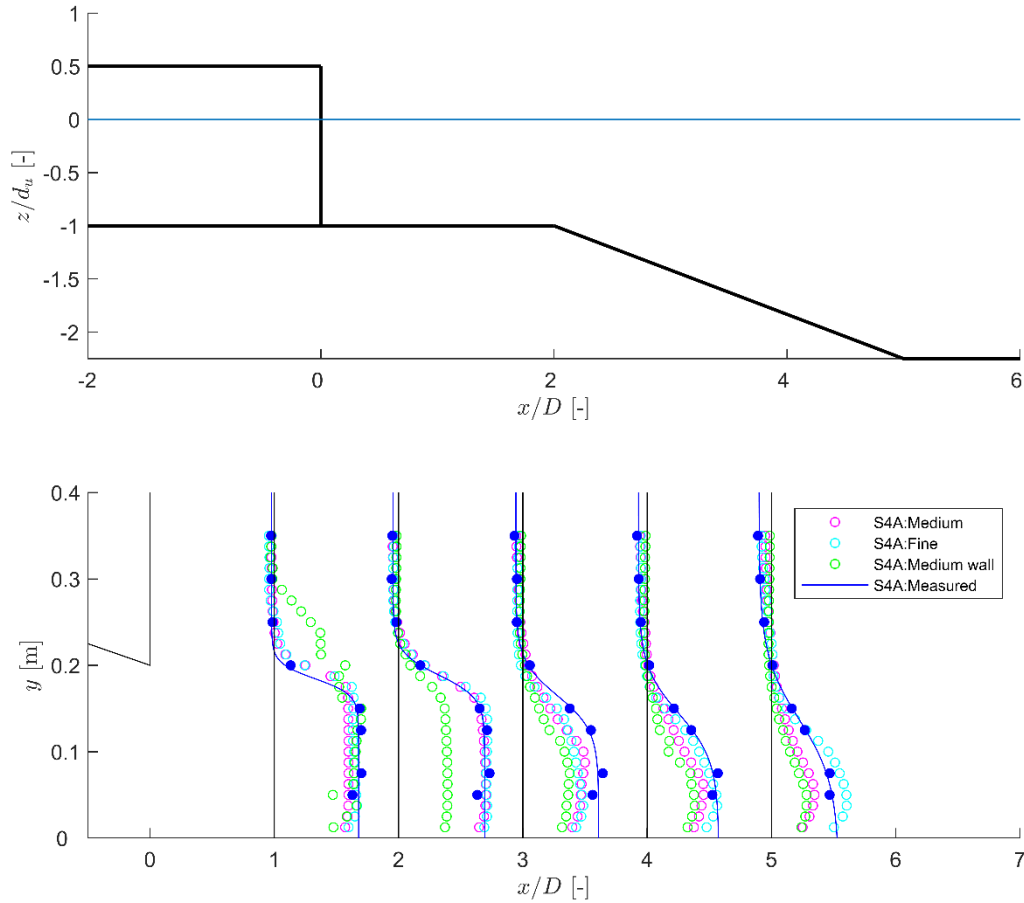
Figure 12: Lateral mixing layer profiles of the depth-averaged streamwise velocity of various mesh resolutions and the measurements, as a function of streamwise distance. The model results are presented as round markers whereas the measurements are plotted in both solid lines (fitted hyperbolic-tangent profile) and round markers (measured) for cases PB and S4A. The top panel guides the reader regarding the position of the slope.

Upon careful examination, it was identified that a minor oversight in the meshing process contributed to this observation. Specifically, the same mesh inflation ratio in the vertical direction was applied across the successive refinements. The inflation ratio being the ratio between the lengths of the first and last cell being inflated. Consequently, when combined with cell refinements, it led to the generation of very small cells as reflected by the significantly higher aspect ratio and numerous cells that were nearly planar, with their volume being small compared to their area; the so-called cells with small determinants in OpenFOAM. As a result, the mesh quality deteriorated and so does the solution. This is also reflected by the y^+, whereby the minimum y^+ value of the fine and extra fine mesh is of one and two orders of magnitude smaller than the medium mesh, respectively. It is worth noting that the medium mesh already exhibited a small y^+ ($= 10^{-2}$). Additionally, the user-defined time-step was not reduced with the successive mesh refinements. The exact impact of this oversight is difficult to gauge due to OpenFOAM's adaptive time-steps which adjusts or overwrites the time-step based on changes in the field values and local mesh sizes when the simulation is running, indirectly defined by the maximum Courant number. Overall, the oversight in the meshing process, coupled with

the consequences it imposed on the mesh quality and the time-step likely played a role in the observed deviation.

As for the medium mesh with side-wall refinements, the higher error is attributed to the high mesh skewness and non-orthogonality. Furthermore, the meshing process encountered limitations with the utility *snappyHexMesh*, which hindered a smoother transition between the wall-refined region and the main flow; hence the interpolation of the steep velocity gradient as you would expect from near-wall modelling strategies may have been compromised, introducing additional errors to the solution. Additionally, the refinements applied towards the wall was not sufficient, as evidenced by many of the first cell centres in the high-velocity regions having a y^+ between 5 and 30 ($5 < y^+ < 30$). This indicates that these cells lie in the buffer-region as opposed to the viscous sublayer, leading to further inaccuracies. Meanwhile, in the same region, the medium mesh has a $y^+ > 30$, which places the cells in the logarithmic region, which can be represented well by the wall functions.

All in all, due to time constraints within the scope of the thesis, it was not feasible to rectify the identified issues by conducting additional runs with a finer mesh configuration. Consequently, the decision was made to proceed with the medium mesh and Courant number of three for further analysis.

Table 6: The mean absolute error (MAE) and root mean square error (RMSE) of the time-averaged flow velocities between the numerical model and measurements.

Grid type	Case S4A		Case S2A		Case S2D	
	MAE (m/s)	RMSE (m/s)	MAE (m/s)	RMSE (m/s)	MAE (m/s)	RMSE (m/s)
Medium	0.044	0.062	0.049	0.073	0.10	0.15
Medium with side wall refinements	0.062	0.085	0.062	0.087	0.13	0.17
Fine	0.062	0.073	0.060	0.087	0.13	0.18
Extra Fine			0.062	0.098		

4.2. Monitoring convergence

The residuals of the velocity components, pressure, k, and ω are examined to assess the convergence behaviour. For this analysis, case S2A is selected as an example, as depicted in Figure 13. The figure consists of two panels: the top panel displays the initial residuals in each time-steps, while the bottom panel shows the iterations performed within the respective time step. For readability, only the first 30 time-steps are shown. The results demonstrate that the PIMPLE algorithm successfully achieved the desired convergence level at every time step, as indicated by the iterations performed. This observation supports the earlier hypothesis derived from the SIMPLE simulation, which suggested that the inability to reach convergence was likely attributed to the unsteady nature of the flow phenomena. By employing the PIMPLE algorithm, which accounts for the unsteadiness of the flow, convergence was effectively attained.
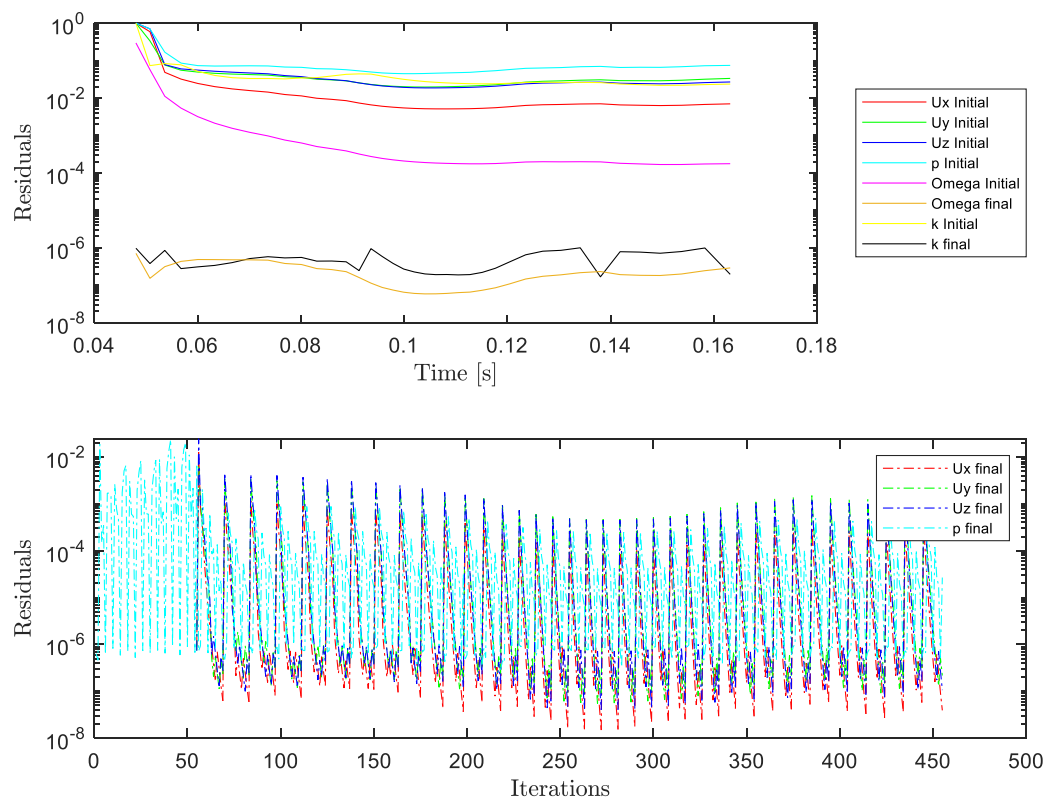
Figure 13: Residuals plot of the velocity components, pressure, k and ω over the first 30 time-steps of case S2A. The upper panel shows the initial residual in every time step and the bottom panel shows the final residual derived from the outer corrections or iterations within each time step, showing convergence is achieved at every time step.

4.3. Comparison of the RANS simulation result with experimental data

In this section, the validation of the RANS simulation utilizing the PIMPLE algorithm is conducted by comparing the data obtained from the medium-resolution mesh model with the experimental data of Broekema et al. (2019). The investigation begins with an analysis of the time-averaged velocity field, followed by the pressure field, time-depth-averaged horizontal mixing layer dynamics and the examination of time-averaged turbulent kinetic energy (TKE).

4.3.1. Time-averaged flow

The comparison of the modelled time-averaged flow velocity field with the measurement data was performed for all cases. The model requires the first 100 seconds of the simulation time for the flow to be fully developed. Therefore, the averaging is carried out beyond this time duration. Moreover, the resolution of the simulation is higher than that of the interpolated measurement data. To ensure a fair comparison, the simulation data is appropriately interpolated to achieve a resolution similar to that of the measurements.

Case S4A and S2A

First, the observed flow fields from the vertically attaching case are analysed (S4A and S2A). As depicted in Figure 14 and Figure 15, it is apparent that when the flow remains vertically attached to the slope, a notable convergence is observed in the high-velocity side of the flow. Additionally, both cases exhibit horizontal flow separation in the low-velocity side of the flow; namely at the edge of the obstruction where a horizontal recirculation zone is present as also observed by Broekema et al. (2019) as well as earlier lateral expansion studies conducted by Talstra (2011).

Case: S4A Simulated
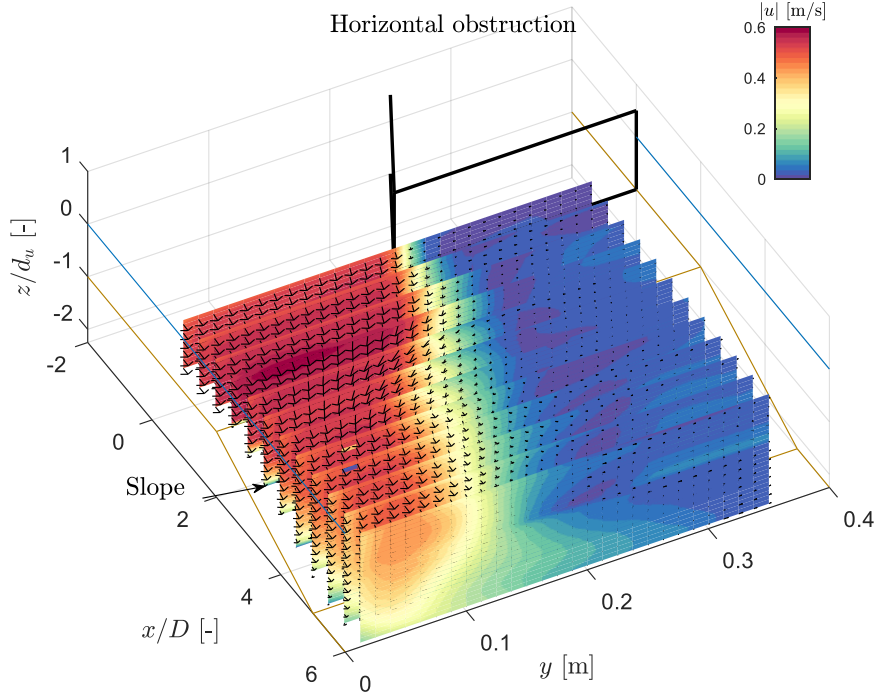
Figure 14: The three-dimensional representation of the time-averaged flow field, where the flow remains attached to the bed (case S4A). The origin of the x-axis, $x/D = 0$, is located at the downstream end of the obstruction. The colour bar represents the magnitude of the mean velocity $|\bar{u}| = \sqrt{\bar{u}_1^2 + \bar{u}_2^2 + \bar{u}_3^2}$. Obtained from the simulation.

Case: S2A Simulated
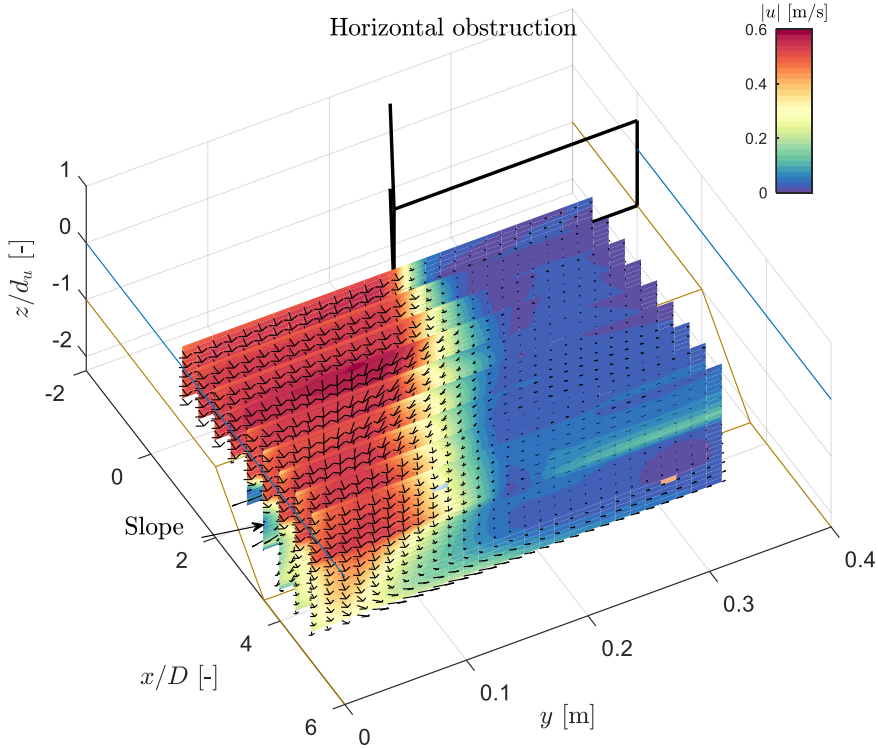
Figure 15: The three-dimensional representation of the time-averaged flow field, where the flow remains attached to the bed (case S2A). The origin of the x-axis, $x/D = 0$, is located at the downstream end of the obstruction. The colour bar represents the magnitude of the mean velocity $|\bar{u}| = \sqrt{\bar{u}_1^2 + \bar{u}_2^2 + \bar{u}_3^2}$. Obtained from the simulation.

The accuracy of the numerical simulations was assessed by comparing the time-averaged flow field with the available measurement data. The quantitative differences between the simulation results and the measurements for cases S4A and S2A are illustrated in Figure 16 and Figure 17, respectively, where the simulated data was subtracted from the measured data. The presented results reveal certain trends regarding the velocity distribution in the simulated flow compared to the measurements. The simulation tends to overestimate the velocity on the high-velocity side of the flow while underestimating it on the low-velocity side, which this research hypothesises to be caused by inadequate turbulence production and mixing between the two velocity regions. Furthermore, due to the absence of experimental measurements taken upstream of the downstream edge of the horizontal obstruction, it is difficult to assess whether the simulation agrees well with the measurements in that region. However, notably, at $x/D = 0$, minimal differences are observed, suggesting that the upstream flow field of the model is in good agreement with the measurements but starts to differ downstream of the horizontal obstruction.

Figure 16: The deviation of the model (measurement - simulation) of the three-dimensional time-averaged flow velocity field, where the flow remains attached to the bed (case S4A). The colour bar denotes the difference in the magnitude of the mean velocity between the measurement and the model ($|\bar{u}|_{measurement} - |\bar{u}|_{model}$).

Figure 17: The deviation of the model (measurement - simulation) of the three-dimensional time-averaged flow velocity field, where the flow remains attached to the bed (case S2A). The colour bar denotes the difference in the magnitude of the mean velocity between the measurement and the model ($|\bar{u}|_{measurement} - |\bar{u}|_{model}$).

Moreover, a consistent overestimation of velocity is observed at the sharp edge of the obstruction, with deviations of up to 0.2 m/s. This discrepancy can be attributed to several factors, including the acceleration of the flow near the contraction, the influence of the wall, and the inherent limitations of the model in accurately capturing the flow behaviour around sharp edges. These factors collectively contribute to the observed differences between the simulated and measured velocities in the vicinity of the obstruction's sharp edge. Furthermore, although generally the vertical profile of the flow field on the high-velocity side is uniform, the flow near the bed over the slopes in both cases is underestimated, as indicated by the red patches of colour in in Figure 16 and Figure 17, which is likely due to the time-averaging of the flow which is highly unsteady. It will be shown in section 4.3.3, how this influences the turbulent horizontal mixing layer dynamics.

Case S2D

The accurate representation of flow separation posed a challenge for the RANS simulation and PIMPLE solver in the case of S2D, as depicted in Figure 18. The model failed to capture the expected behaviour of flow separation and instead exhibited flow

characteristics that closely resembled the vertically attached flow observed in the other cases. Consequently, the flow remained vertically uniform. In contrast to the model's behaviour, the measurement data suggests that in the case of flow separation, the flow should exhibit strong divergence rather than convergence. This discrepancy is evident from the significant differences in velocity between the high-velocity and low-velocity sides of the flow, as illustrated in Figure 19. The aforementioned behaviour persisted even when employing finer mesh resolutions and lower Courant number of 0.7 (not shown for brevity), indicating that numerical factors were not solely responsible for this discrepancy. The case S2D was also reperformed with the $k - \varepsilon$ model (Appendix C), which also results in flow convergence and attachment, suggesting that the observed flow state is not due to the turbulence closure model.
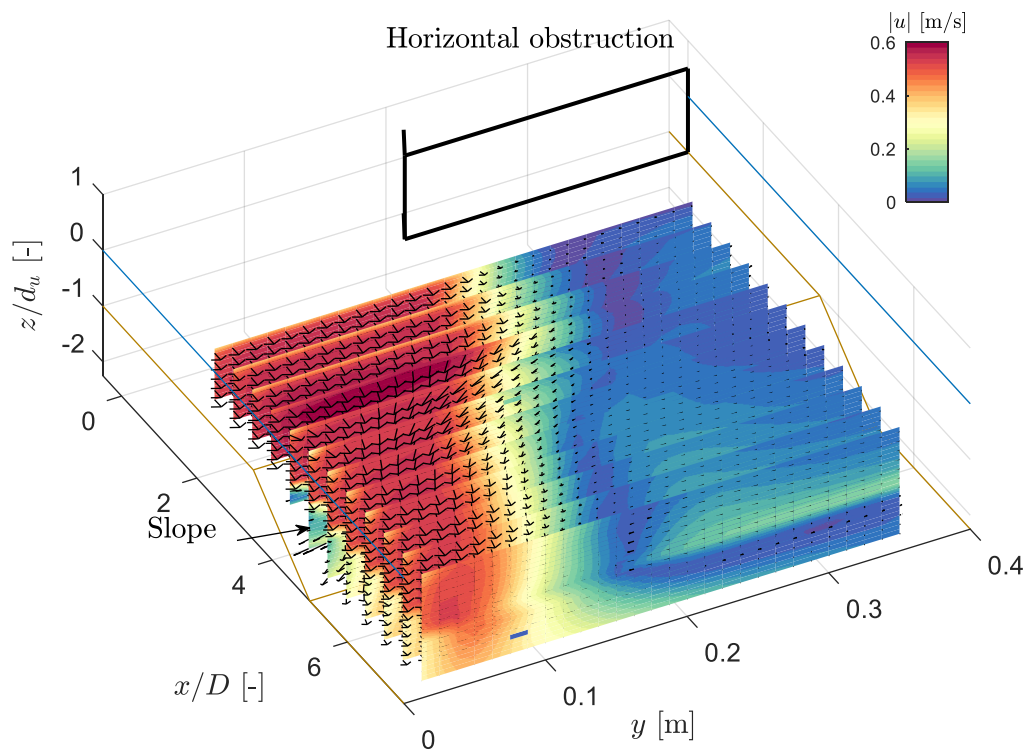
Figure 18: The three-dimensional representation of the time-averaged flow field of case S2D. The origin of the x-axis, $x/D = 0$, is located at the downstream end of the obstruction. The colour bar represents the magnitude of the mean velocity $|\bar{u}| = \sqrt{\bar{u}_1^2 + \bar{u}_2^2 + \bar{u}_3^2}$. Obtained from the simulation.
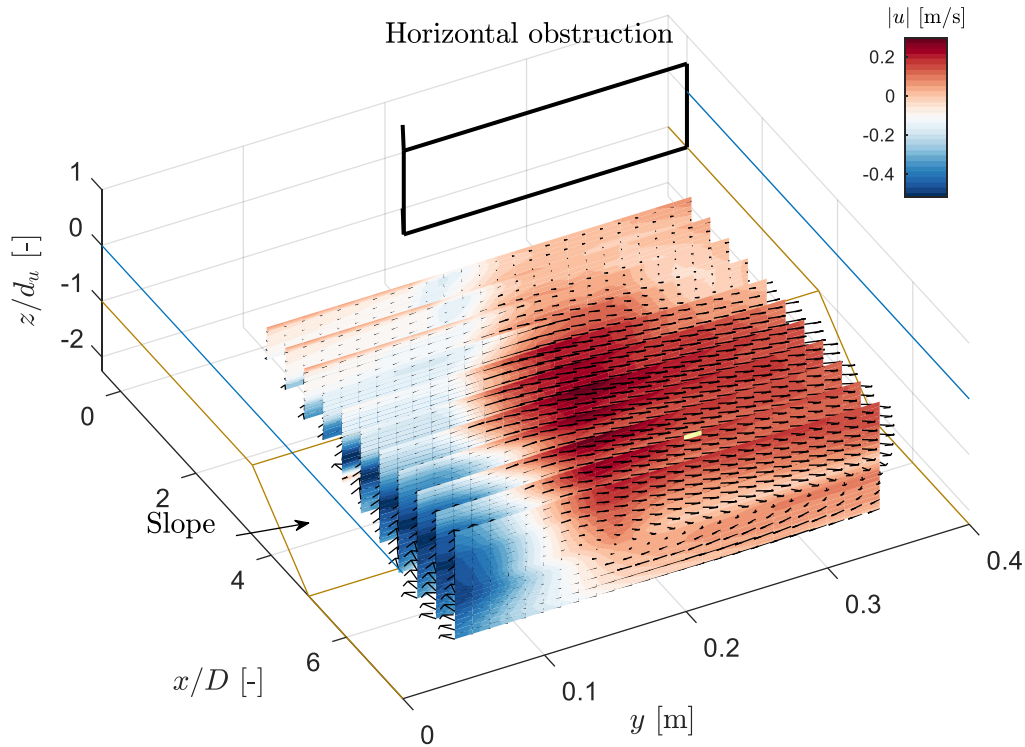
Figure 19: The deviation of the model (measurement - simulation) of the three-dimensional time-averaged flow velocity field, of case S2D. The colour bar denotes the difference in the magnitude of the mean velocity between the measurement and the model ($|\bar{u}|_{measurement} - |\bar{u}|_{model}$).

Broekema et al. (2019) reported that vertically separating flow was observed when the contraction was moved further upstream or away from the upstream edge of the slope. This is based on the understanding that the positioning of the contraction controls the magnitude of the lateral velocity gradient. Specifically, when there is a minimal lateral velocity gradient, the flow does not converge, and flow separation takes place. This observation prompted this research to investigate whether inducing flow separation is possible by adjusting the positioning of the contraction further upstream, thereby reducing the lateral velocity gradient.

To investigate this hypothesis, two additional cases were considered, where the horizontal obstruction is moved further upstream by 0.1 m ($L_D = 0.8$ m) and 0.3 m ($L_D = 1$ m). In line with the reference S2D case, the former adjustment ($L_D = 0.8$ m) did not exhibit flow separation whereas the latter adjustment ($L_D = 1$ m) resulted in vertical flow separation. A comparison between Figure 20 and Figure 18 reveals a slight divergence towards the low-velocity side of the flow because of this positioning. The flow fully diverges, and flow separation occurs when the obstruction is brought even further upstream, as shown by Figure 21. Notably, the flow is also confined to the upper part of the water column due to the vertical recirculation zone; much like the measurements of Broekema et al. (2019). A plausible explanation for this observation is that the placement of the obstruction further upstream allows for the mixing layer, due to the abrupt expansion downstream of the obstruction, to develop and widen over further distance

before reaching the slope. This finding insinuates that the mixing process in the model may be slower than in reality, potentially due to lower turbulence generation and thus insufficient mixing; as will be shown in Section 4.3.4. As a result, the reduction in the lateral velocity gradient is less pronounced, necessitating the obstruction to be placed further upstream for the mixing layer and turbulence to sufficiently develop to give enough mixing and reduction in the lateral velocity gradient, which leads to flow divergence and subsequently flow separation. Thus, these findings support the hypothesis that flow separation can be induced by reducing the lateral velocity gradient.

Case: Slope 1:2 with $L_d = 0.8$m
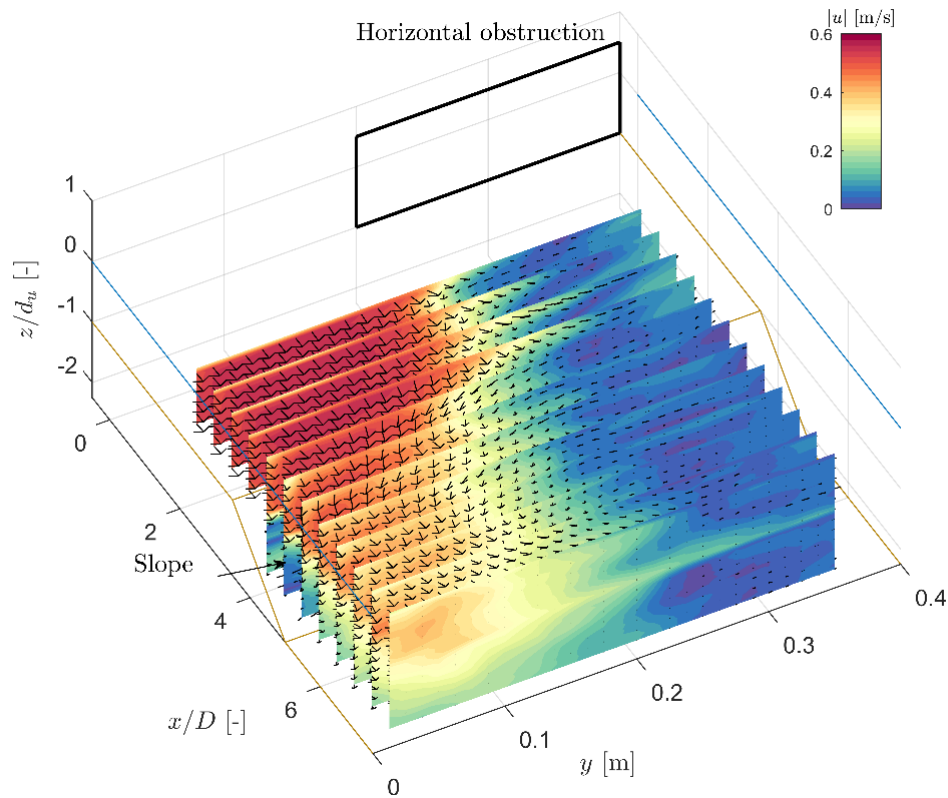
Figure 20: The three-dimensional representation of the time-averaged flow field, where the obstruction is moved further back by 0.1m from the S2D reference case; hence an L_D of 0.8m. The origin of the x-axis, $x/D = 0$, is located at the downstream end of the obstruction. The colour bar represents the magnitude of the mean velocity $|\bar{u}| = \sqrt{\bar{u}_1^2 + \bar{u}_2^2 + \bar{u}_3^2}$. Obtained from the simulation.
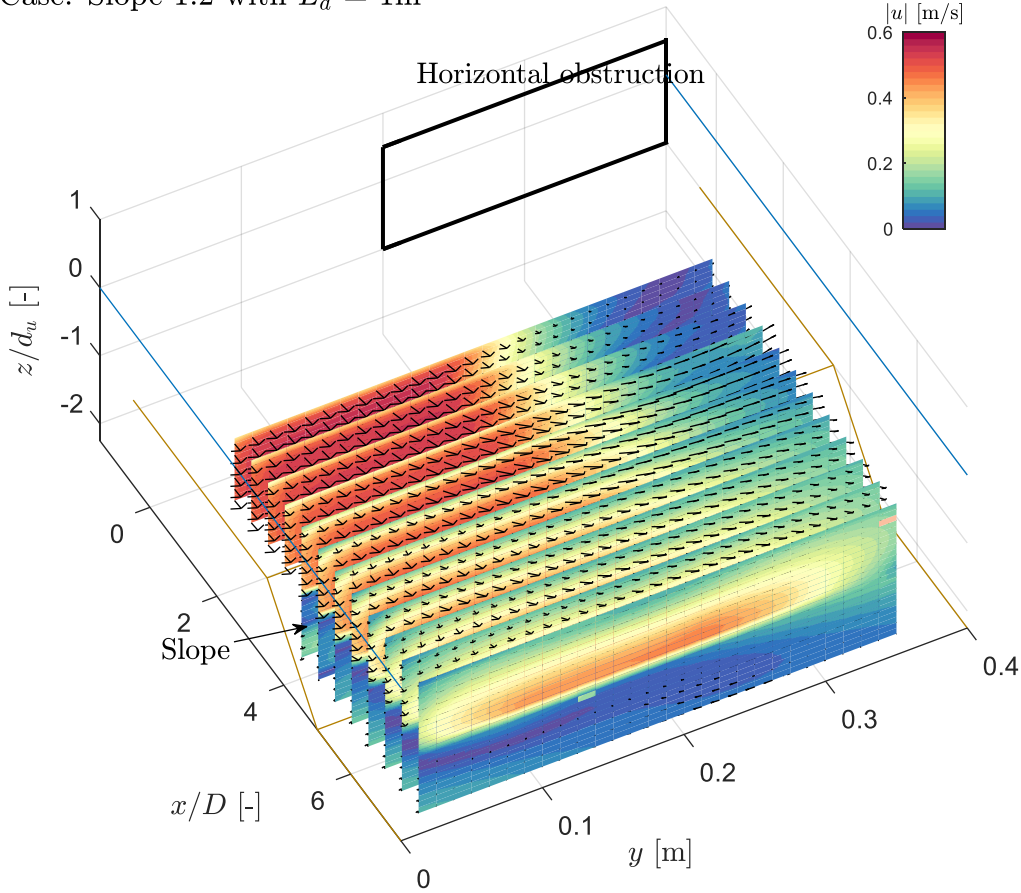
Figure 21: The three-dimensional representation of the time-averaged flow field, where the obstruction is moved further back by 0.3m from the S2D reference case; hence an L_D of 1.0m. The origin of the x-axis, $x/D = 0$, is located at the downstream end of the obstruction. The colour bar represents the magnitude of the mean velocity $|\bar{u}| = \sqrt{\bar{u}_1^2 + \bar{u}_2^2 + \bar{u}_3^2}$. Obtained from the simulation.

Furthermore, the flow field of case S2D displayed backflow, indicating that the outlet of the channel was not positioned sufficiently far from the turbulent region of the flow. Ideally, the outlet should be placed in a relatively steady state, away from areas of strong turbulence, to allow the flow to fully develop downstream and be correctly simulated numerically without the imposed boundary condition significantly influencing the solution or flow field. To address this issue, one can expand the computational domain to include more of the downstream geometry, minimizing the impact of the boundary condition on the predicted flow, or to modify the boundary conditions themselves. In this study, the simulation of case S2D was repeated with slight adjustments made to the pressure outlet boundary conditions, as will be described in Section 4.3.2. Henceforth, the case S2D with adjustments in the pressure boundary condition is referred to as case S2Dp.

Case: S2Dp Simulated
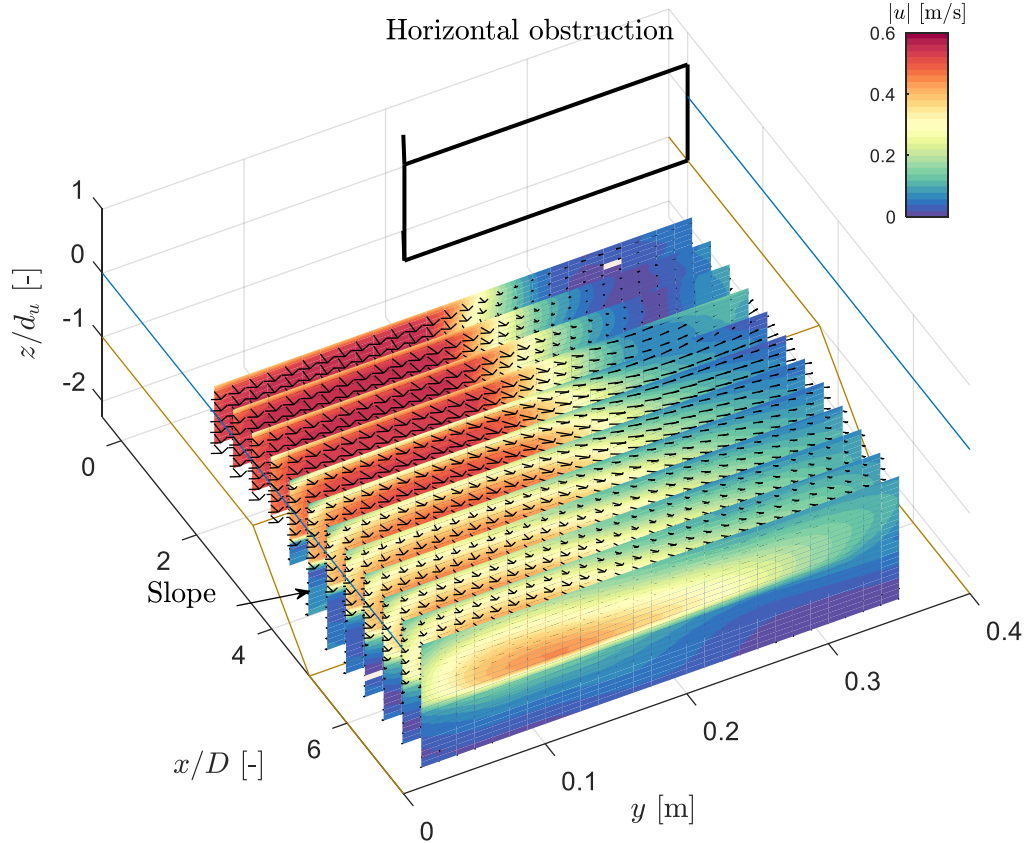
Figure 22: The three-dimensional representation of the time-averaged flow field, where the flow separates from the bed by adjusting the pressure outlet boundary condition, case S2Dp. The origin of the x-axis, $x/D = 0$, is located at the downstream end of the obstruction. The colour bar represents the magnitude of the mean velocity $|\bar{u}| = \sqrt{\bar{u}_1^2 + \bar{u}_2^2 + \bar{u}_3^2}$. Obtained from the simulation.

The adjustment in the boundary conditions resulted in a flow behaviour that more closely resembled the measured data, as illustrated in Figure 22, where the flow exhibited vertical separation and horizontal divergence. Nonetheless, it should be noted that the simulation still shows notable discrepancies compared to the measurement data. As depicted in Figure 23, the simulation tends to overestimate the velocity in the upper part of the water column while underestimating it elsewhere. This discrepancy is further emphasised in Figure 24, which shows noticeable differences in the upper water column of the high-velocity side between the simulation and measurements. These discrepancies can be attributed, at least in part, to the underestimation of the vertical mixing past the slope, which will be analysed further in Section 4.3.3
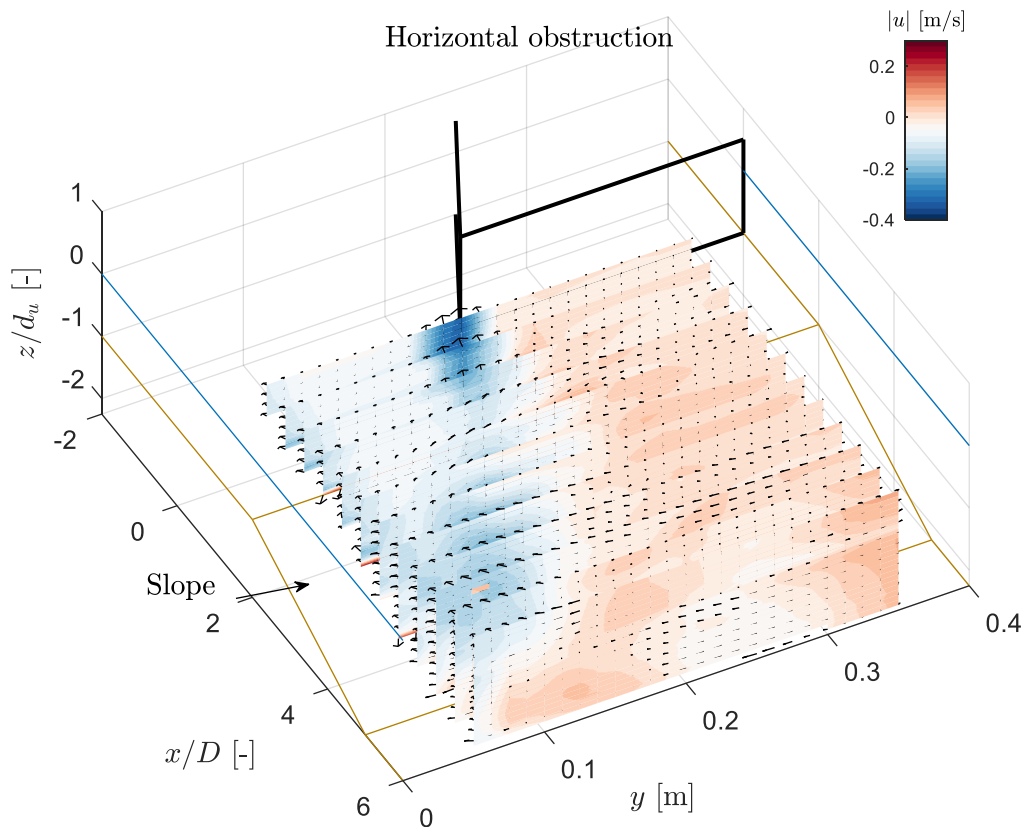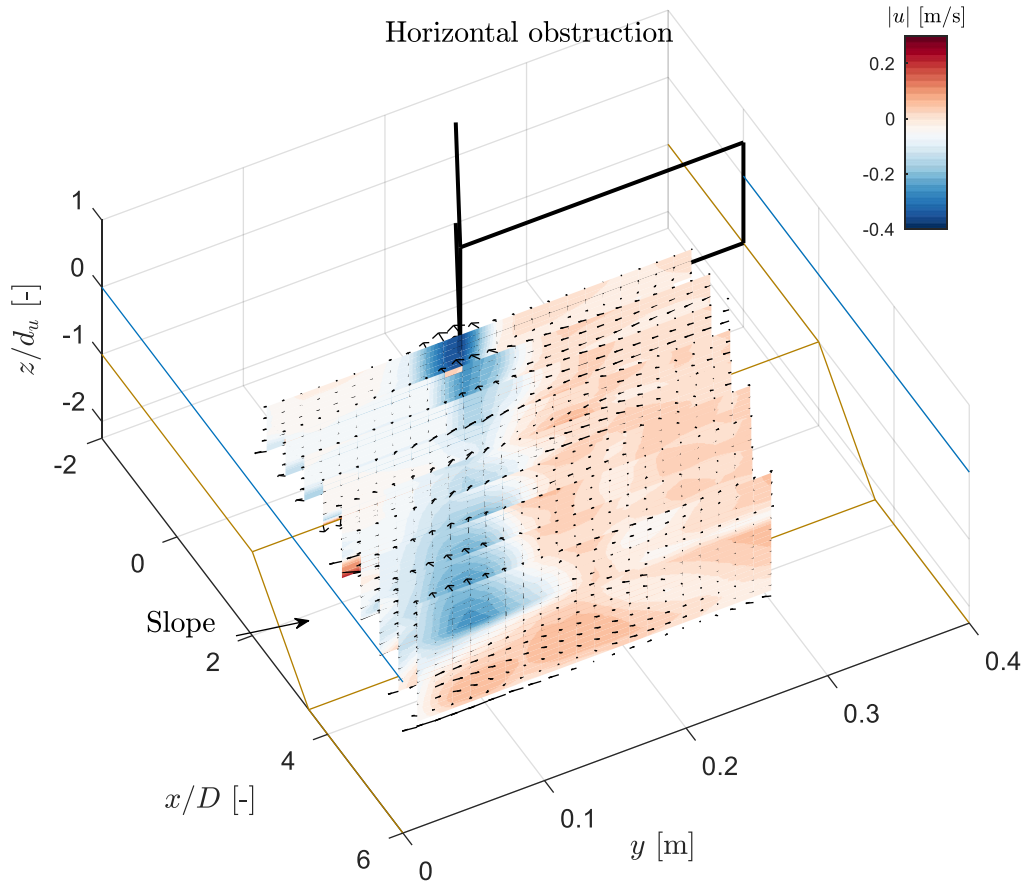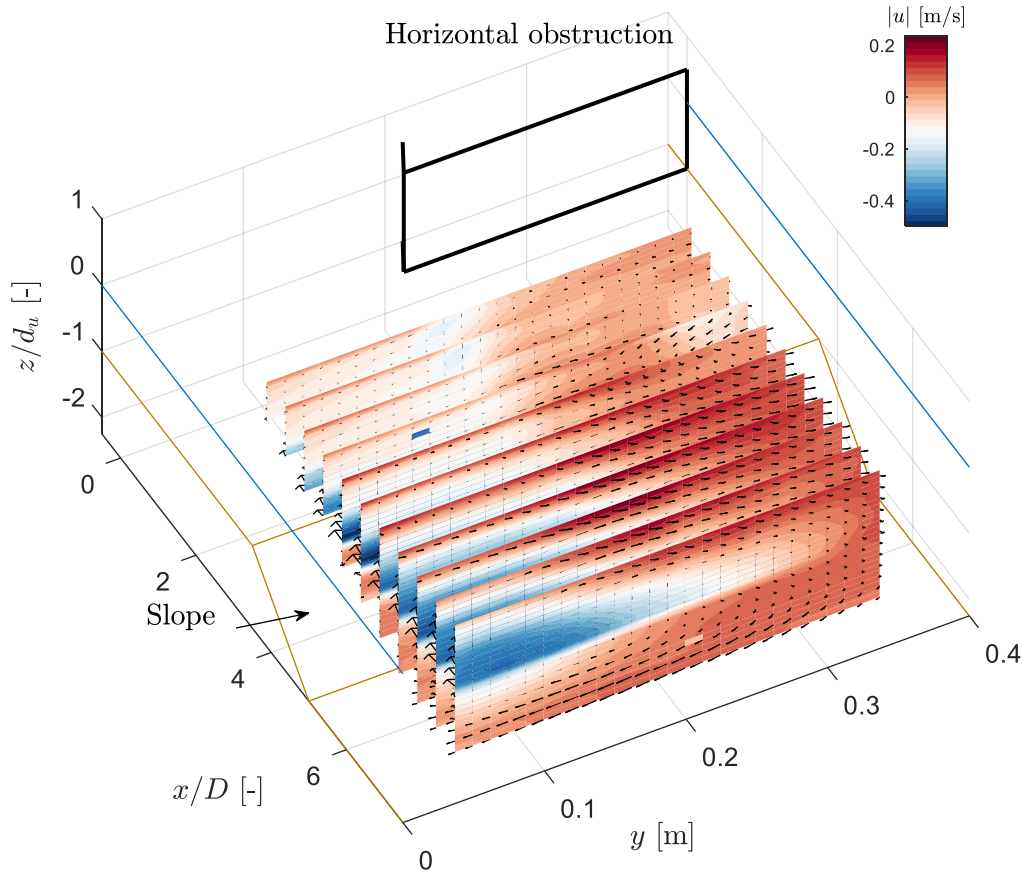
Figure 23: The deviation of the model (measurement - simulation) of the three-dimensional time-averaged flow velocity field, where the flow separates to the bed by adjusting the pressure outlet boundary condition (case S2Dp). The colour bar denotes the difference in the magnitude of the mean velocity between the measurement and the model ($|\bar{u}|_{measurement} - |\bar{u}|_{model}$).

Thus, to this end, the case S2D, with flow separation, was successfully captured by using two methods: 1) shifting the horizontal obstruction backward, supporting the hypothesis of Broekema et al. (2019) that flow separation can be induced by reducing the lateral velocity gradient and 2) changing the pressure outlet boundary condition, which can be considered more of a modelling choice that results in a more accurate representation of the flow field. These findings provide motivation for further investigation into the pressure field, as detailed in the next section.
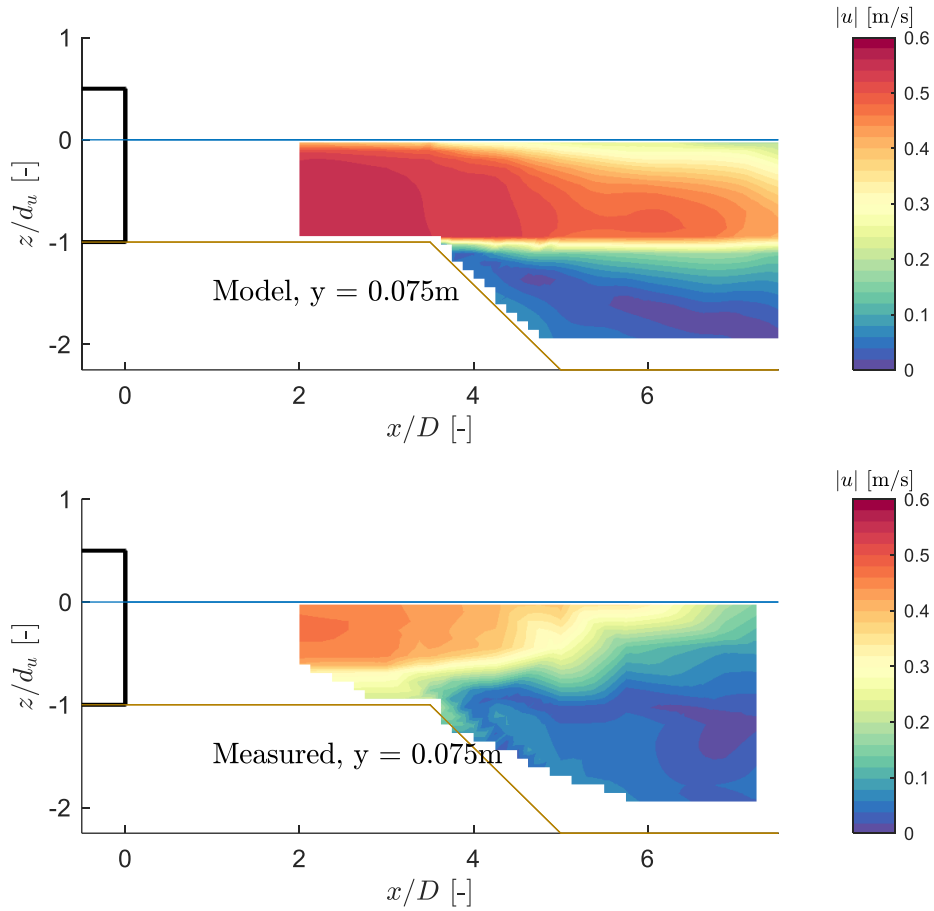
Figure 24: The side view of the vertically separating case (S2Dp) in the high-velocity side (y = 0.075 m), highlighting the difference of the upper part of the water column of the model (top) and the measurements (bottom).

4.3.2. Pressure field

Boundary layer separation is predominantly influenced by the pressure gradient. In this section, the time-averaged dynamic pressure (kg m s^{-2}) of the flow field is analysed. The hydrostatic pressure was not accounted for due to the rigid-lid assumption adopted in the model. Hence, quantitative comparison with the measurement data is also not performed. For convenience, the dynamic pressure is expressed in mm after dividing it with the gravity constant (g = 9.81 m^2 s^{-1}) and the density of water (1000 kg m^{-3}). First, the pressure field of cases S2A and S2Dp are compared to characterize differences in the pressure fields of a vertically attaching and separating flows. Next, the case S2Dp is compared with the reference S2D model case to highlight the improvement arising from the pressure outlet adjustments. Lastly, the pressure field of case S2Dp is compared with that of the simulation where the horizontal was pushed back to 1 m which also results in flow separation.

As earlier mentioned, adjustments were made to the pressure boundary condition that allows for the simulation of vertical flow separation and diverging flow (case S2Dp). As opposed to setting the outlet pressure at a constant value of zero, the pressure at the

outlet was set to have zero gradient (*zeroGradient*), similar to the other pressure boundaries. By doing so, none of the boundaries have a fixed value, hence the value of the pressure in the system is indeterminate to a constant. Since in a closed incompressible system the pressure is relative, only the pressure range or gradient matters and not the absolute value. Therefore, a reference pressure value (*pRefValue*) of 0 was assigned to an arbitrary cell 0 (*pRefCell*) to establish a unique pressure solution. This is analogous to setting an integration constant for the pressure much like the previous constant value of zero at the outlet.

Figure 25 (a,c,e) and Figure 25 (b,d,f) represent the pressure fields of case S2A and S2Dp, respectively. From the top view (Figure 25a and Figure 25b), it is seen that the pressure varies slightly in the transverse direction. On the leeside of the obstruction ($y = 0.25$ m), both cases demonstrate a minor increase in pressure along the streamwise distance, although case S2Dp exhibits a more pronounced increase further downstream past the slope. Notable pressure disparities between the two cases are prominent in the high-velocity side of the flow ($y = 0.075$ m). In instances where flow separation occurs, there is a pressure increase towards the upstream edge of the slope, which is presumably the separation point (Figure 25d). According to Bernoulli's principle, as pressure increases with streamwise distance, the flow decelerates due to the adverse pressure gradient, often resulting in flow separation. Conversely, when the flow remains vertically attached, the pressure towards the upstream edge of the slope decreases (Figure 25c). This pressure decrease leads to an acceleration of the flow velocity, countering the adverse pressure gradient caused by the increase in depth over the slope, which is nicely illustrated by the shift in colour from blue to red over the slope (Figure 25c). An alternative chronological explanation for this flow state would be that there is a reduced deceleration of the flow at the slope due to the horizontal flow convergence which counteracts the adverse pressure gradient.
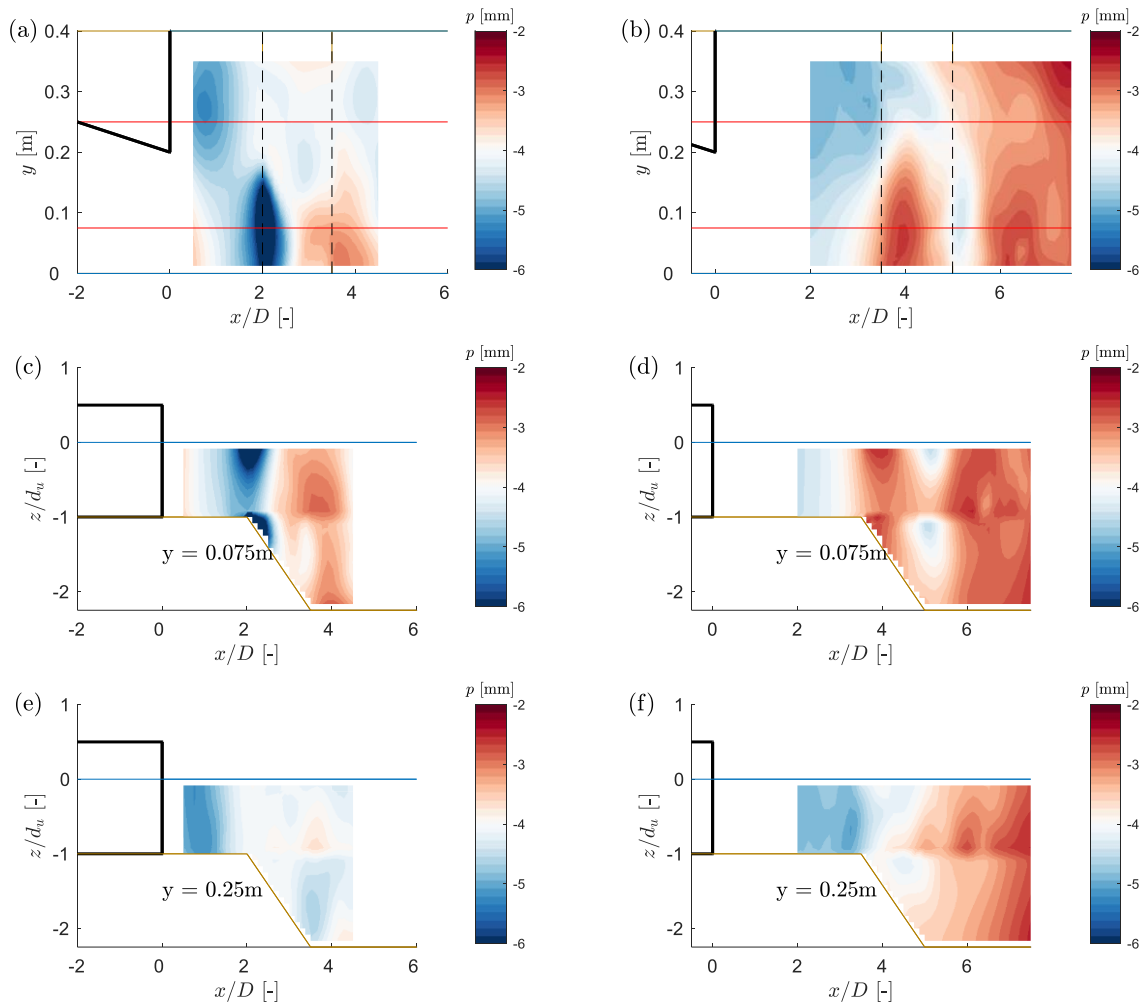
Figure 25: Time-averaged pressure field for case S2A (a,c,e) and S2Dp (b,d,f). (a,b) shows the top view, where the solid black line indicates the horizontal obstruction while the dashed black line indicates the location of the slope. The red lines indicate the location of the high- and low velocity side. (c,d) shows the vertical xz plane of the pressure at the high velocity side. (e,f) shows the vertical xz plane of pressure at the low velocity side. The yellow and blue lines in panels (c-f) indicate the bed and the water surface, respectively.

The comparison of the pressure fields between the case of S2Dp and the case where the horizontal obstruction is positioned further back reveals similarities (Figure 26). Notably, in the latter case, a lower pressure prior to the upstream edge of the slope can be observed, in both the low- and high-velocity side (Figure 26b,c). As previously hypothesised, relocating the obstruction further upstream facilitates the development of the mixing layer over a greater distance, thereby reducing lateral nonuniformity. Consequently, this reduction in lateral nonuniformity contributes to decreased turbulence intensities downstream of the slope, ultimately eliminating the occurrence of backflow and enabling the model to capture flow separation without the need to modify the pressure boundary condition at the outlet.
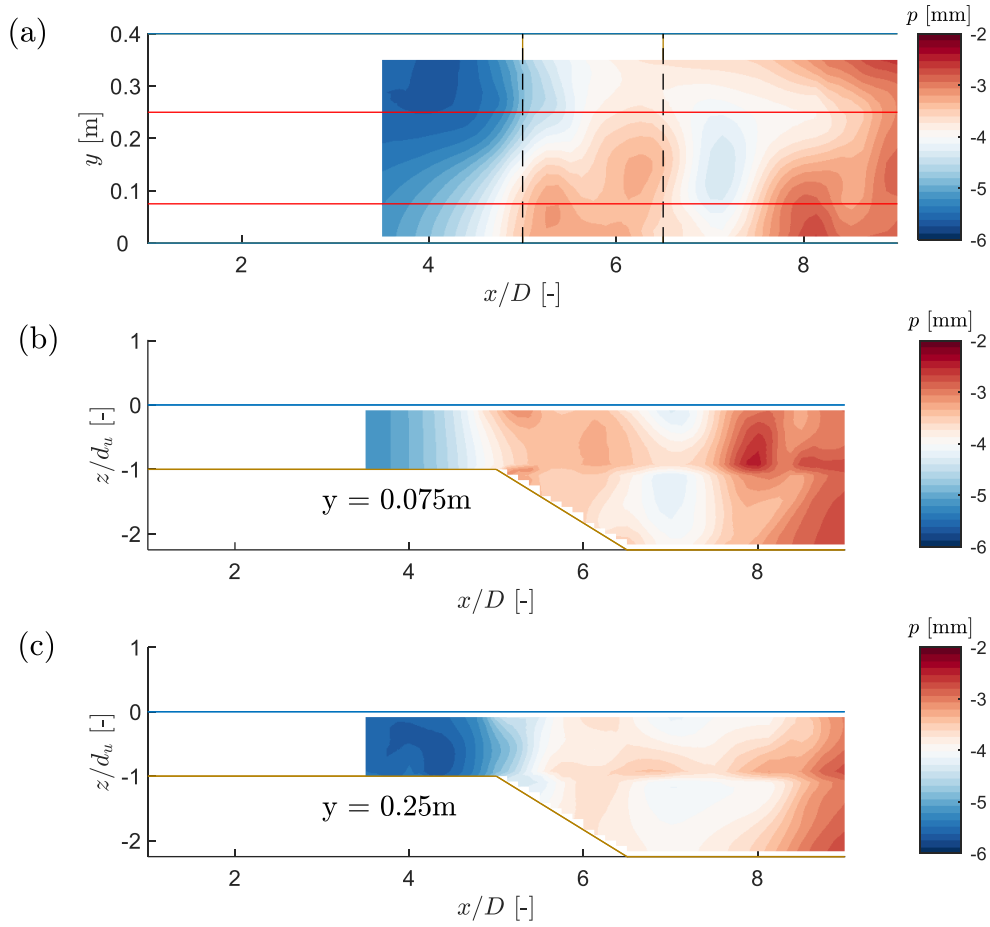
Figure 26: Time-averaged pressure field for the case where the horizontal obstruction is pushed back to $L_D = 1$ m. (a) shows the top view, where the dashed black line indicates the location of the slope. The red lines indicate the location of the high- and low velocity side of the flow. (b) shows the vertical xz plane of the pressure at the high velocity side. (c) shows the vertical xz plane of the pressure at the low velocity side. The yellow and blue lines in panels (b,c) indicate the bed and the water surface, respectively.

4.3.3. Horizontal mixing layer dynamics

This section focuses on the analysis of the downstream development of the mixing layer in the flow. It is well-established that in a fully developed flow, the turbulent shear layers exhibit a self-similar growth pattern (Townsend, 1976). Self-similarity manifests in the mean velocity profiles, whereby the mean velocity profiles can be expressed as a function of flow quantities such as, the lateral velocity differences and the width of the mixing layer, just to name a few, while maintaining geometric similarity across different sections of the flow. Hence, the possibility of describing the transverse profile of the streamwise velocity using a profile function (van Prooijen & Uijttewaal, 2002). In the context of a mixing layer, self-similarity implies a linear growth of the mixing layer with time (Ansari, 1997). The understanding of self-similarity and the significance of mixing layers in various domains, such as aerodynamics and chemical mixing, have motivated extensive experimental investigations (Rogers & Moser, 1994) to explore the growth rates and shapes of self-similar profiles, among other aspects. However, there is no general

agreement on these problems, partly attributed to the various free-stream turbulence level, initial conditions, and other factors (Ansari, 1997).

This study aims to investigate the self-similar behaviour of the mean flow field in the horizontal mixing layer using the theoretical model proposed by van Prooijen and Uijttewaal (2002), which assumes self-similarity in the lateral profiles of the depth-averaged streamwise velocity. It is important to note that this model was originally developed after a plane bed (PB) configuration, which represents a horizontal flume without the influence of side walls and with constant bathymetry. In contrast, the scenarios examined in this study, as well as in the work of Broekema et al. (2019), involves lateral expansion and a sloping bed resulting in an increase in flow depth. Despite these differences, the theoretical model of van Prooijen and Uijttewaal (2002) proves to be applicable in describing the mixing layer characteristics observed in the study of Broekema et al. (2019). This suggests that the model captures the essential properties of the mixing layer, despite the variations in the flow configuration. Furthermore, the theoretical model has been previously validated by Talstra (2011) in the context of shallow lateral expansion, demonstrating good agreement with the observed self-similar behaviour, particularly in the near-field regions ($x/D < 4$). Hence, the reliability of the theoretical model in describing mixing layer dynamics. The theoretical model is as follows (van Prooijen & Uijttewaal, 2002):

$$U(x,y) = U_c(x) + \frac{\Delta U(x)}{2}\tanh\left(\frac{y - y_c(x)}{\frac{\delta(x)}{2}}\right) \qquad (11)$$

Where:
- $U(x,y)$ is the depth-averaged streamwise velocity.
- $\Delta U(x)$ being the velocity difference over the mixing layer, defined as $\Delta U = U_1 - U_2$, where U_1 and U_2 are the maximum and minimum velocities over the mixing layer, respectively.
- $U_c(x)$ being the mean velocity at the centre of the mixing layer, defined as $U_c = (U_1 + U_2)/2$.
- $\delta(x)$ being the width of the mixing layer, defined as $\frac{\Delta U}{\frac{\partial U}{\partial y}(y_c)}$, where y_c is the lateral centreline position of the mixing layer.

Case S4A and S2A
Figure 27 and Figure 28 depicts the depth-averaged streamwise velocity mixing layer profiles of the case S4A and S2A, respectively, as a function of streamwise distance of the model, alongside the corresponding measurement data.

The comparison between the model results and the measurement data reveals a generally satisfactory agreement. However, a noticeable discrepancy emerges in the vicinity of the slope ($x/D \geq 3$), where the model tends to underestimate the velocity

compared to the measurements. It is worth noting that this is also the region where the measurements start to deviate from the plane bed reference, given the increase in flow depth over the slope. Upon reviewing the time-averaged flow (Figure 14), it becomes evident that the model underestimates the near-bed velocity in the proximity of the slope. Consequently, when considering the depth-averaged velocity, the overall flow velocity around the slope is diminished, leading to the observed underprediction of flow velocity on the high-velocity side of the mixing layer. This discrepancy highlights the influence of the near-bed flow dynamics on the overall flow behaviour and emphasizes the need for improved modelling approaches to accurately capture the flow characteristics near the sloping region.
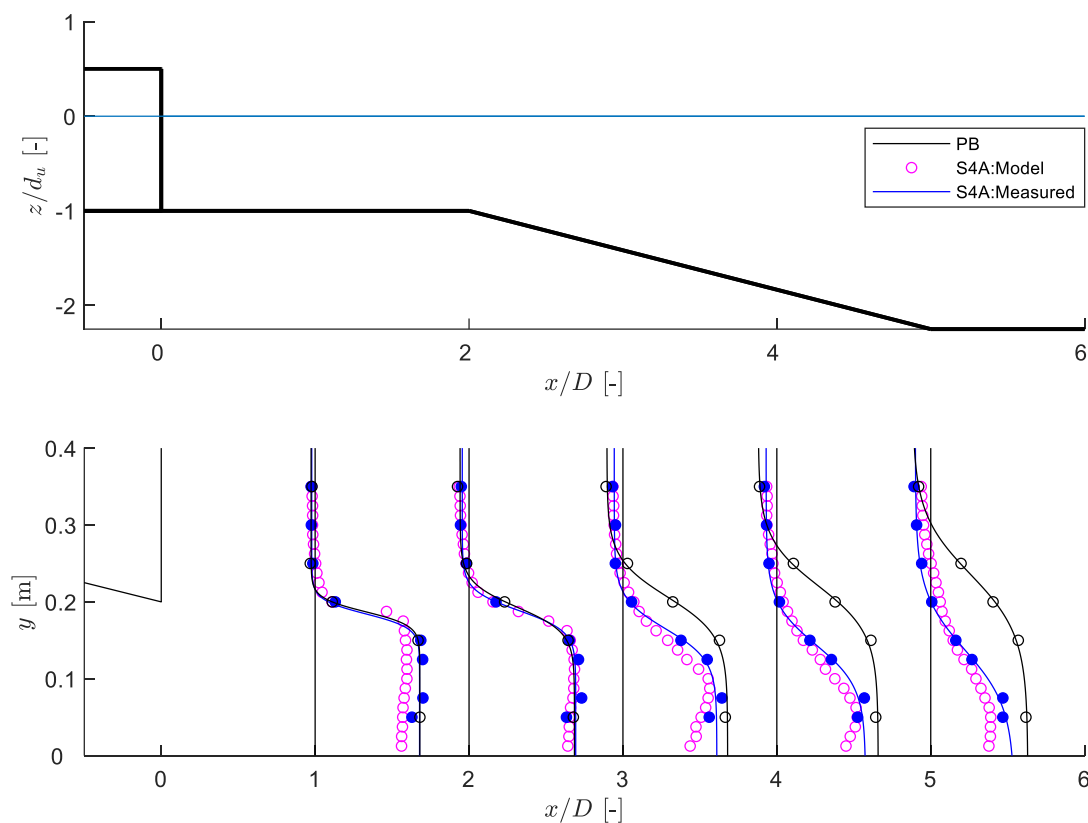
Figure 27: Lateral mixing layer profile of the depth-averaged streamwise velocity of the model and measurement as a function of streamwise distance. The measurements are plotted in both solid lines (fitted hyperbolic-tangent profile) and round markers (measured) for cases PB and S4A. The top panel guides the reader regarding the position of the slope.
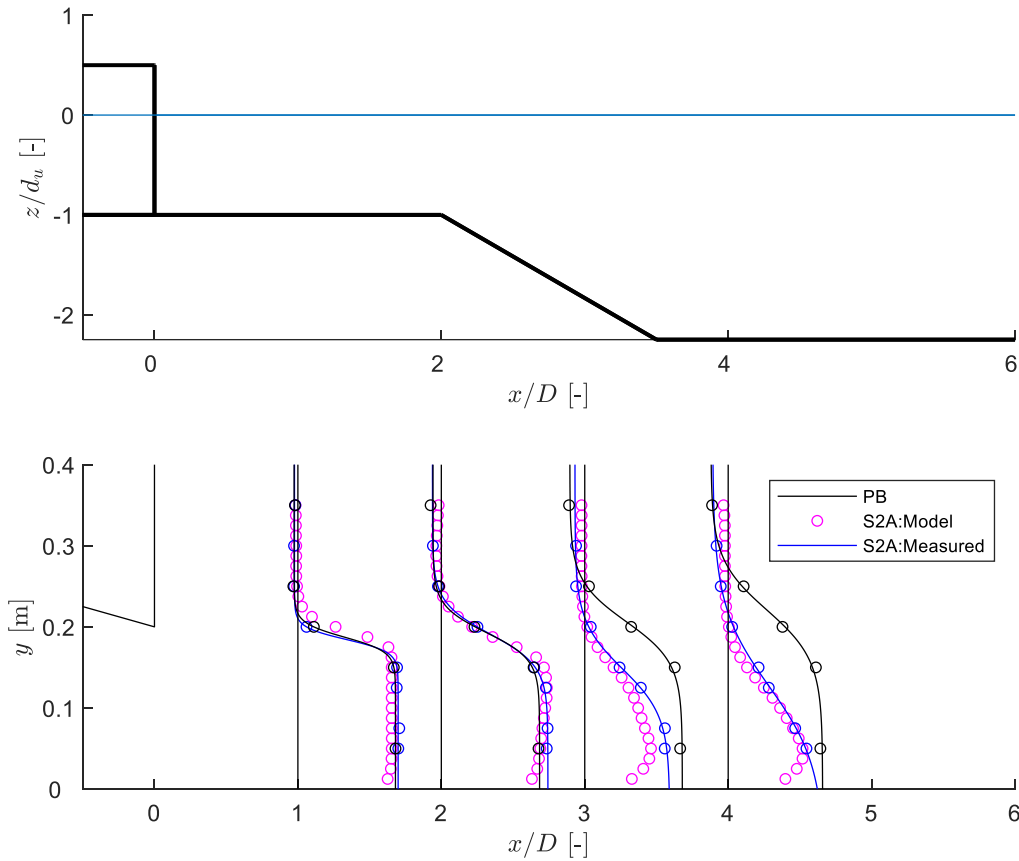
Figure 28: Lateral mixing layer profile of the depth-averaged streamwise velocity of the model and measurement as a function of streamwise distance. The measurements are plotted in both solid lines (fitted hyperbolic-tangent profile) and round markers (measured) for cases PB and S2A. The top panel guides the reader regarding the position of the slope.

In addition, van Prooijen and Uijttewaal (2002) have identified several key characteristics of the shallow mixing layer, including a decrease in velocity difference (ΔU) downstream, a reduced growth rate of the mixing layer width (δ), and a displacement of the mixing layer centre (y_c) towards the low-velocity side. Consequently, these specific properties are examined in Figure 29 and Figure 30, showcasing the results for the plane bed reference case, the measurement data, and the model outcomes for cases S4A and S2A, respectively.

From Figure 29a and Figure 30a, it is observed that upstream of the slope, both the model and measurement data demonstrate a slight increase in velocity difference, attributed to the formation of the horizontal recirculation zone (Broekema et al., 2019). In case S4A, the velocity differences across the domain of the measurements are almost uniform, with a minor drop along the slope. The steeper slope, case S2A, shows a more pronounced drop in the measurements; likely due to the sharper increase in water depth. Consistent in both cases, the model exhibits a similar drop, although to a considerably greater extent, as it replicates the decrease in velocity differences caused by the increase in flow depth over the slope. In case S4A, the model continues to show a drop in velocity differences

over the slope, while the measurements remain relatively uniform after the initial drop. Interestingly, in case S2A, a recovery behaviour is observed downstream of the slope.
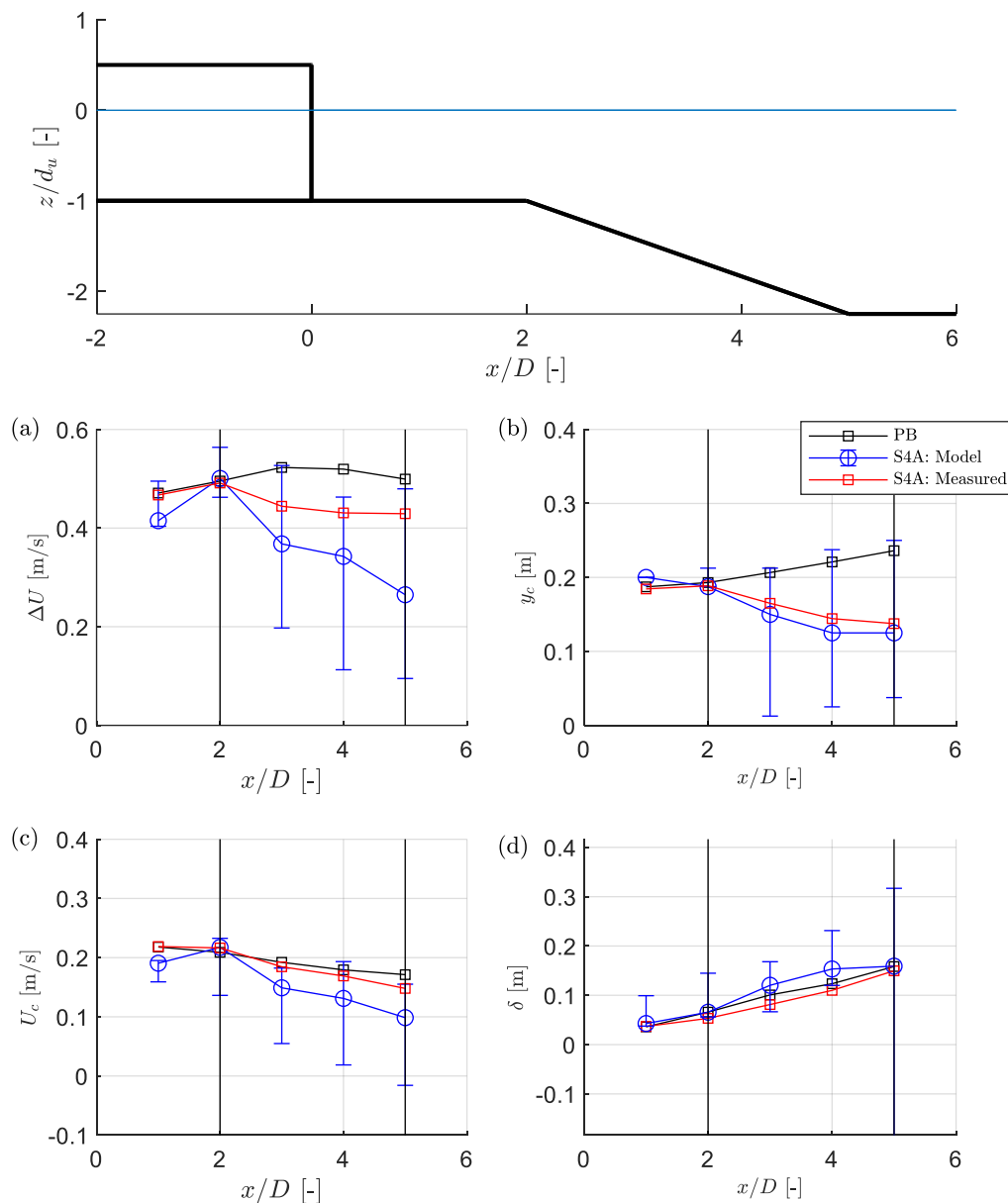
Figure 29: The individual mixing layer properties of the depth-averaged streamwise velocity of case S4A. (a) The velocity difference between the high- and low-velocity side of the mixing layer; (b) the lateral centreline position of the mixing layer; (c) the velocity at the centreline of the mixing layer; (d) the mixing layer width. The error bars indicate the range obtained from the individual calculations from the respective time steps that were averaged over to obtain the time-averaged value. The solid black line represents the upstream and downstream edges of the slope.

Looking at Figure 29b and Figure 30b, the model accurately captures the displacement of the mixing layer's centreline towards the high-velocity side over the streamwise distance, consistent with the measurement data which is uncharacteristic of a typical mixing layer behaviour where the centreline displaces towards the low-velocity side (van Prooijen et al., 2005). This results from the need for the flow to converge over an increase in flow

depth to maintain the uniform vertical structure of the flow, satisfying the conservation of mass (Broekema et al., 2019).

Figure 29c and Figure 29d (Figure 30c and Figure 30d) are best examined together. Following the definition of van Prooijen and Uijttewaal (2002), the growth of the mixing layer is influenced by the velocity difference and the lateral velocity gradient at the centre of the mixing layer. The measurements showed a relatively constant velocity difference and velocity at the centre of the mixing layer, explaining the linear growth of the mixing layer over the streamwise distance. However, the model results exhibit greater variations in the velocity difference and the velocity at the centre of the mixing layer which account for the non-uniform mixing layer growth. Overall, the model struggles to model accurately the velocity differences and hence the subsequent mixing layer width that is derived from it. Notably, in case S2A (Figure 30d), the mixing layer width of the model is smaller than the measurements downstream of the slope.
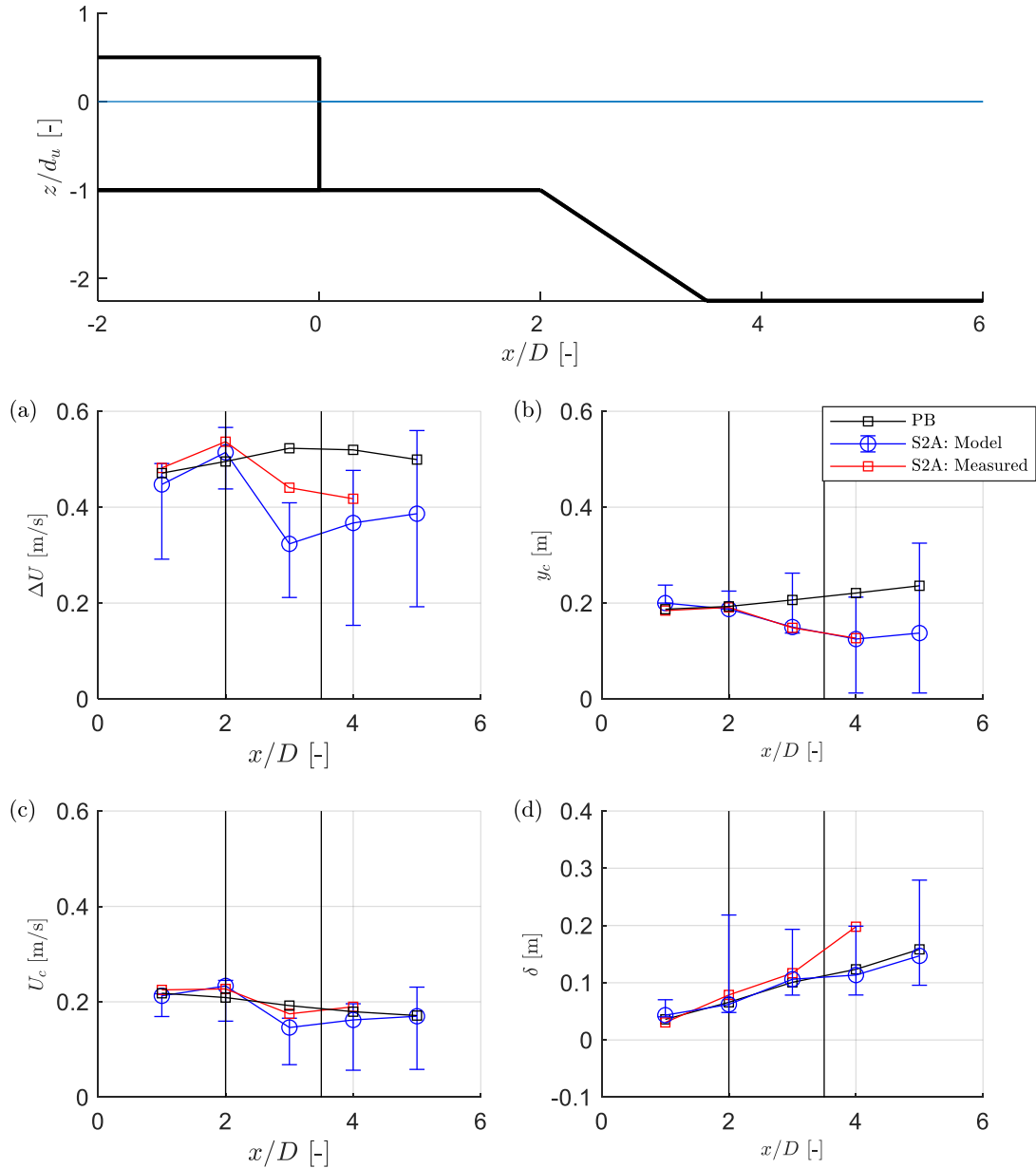
Figure 30: The individual mixing layer properties of the depth-averaged streamwise velocity of case S2A. (a) The velocity difference between the high- and low-velocity side of the mixing layer; (b) the lateral centreline position of the mixing layer; (c) the velocity at the centreline of the mixing layer; (d) the mixing layer width. The error bars indicate the range obtained from the individual calculations from the respective time steps that were averaged over to obtain the time-averaged value. The solid black line represents the upstream and downstream edges of the slope.

Case S2Dp

The lateral mixing layer profiles of the case S2Dp as a function of streamwise distance is illustrated in Figure 31. Notably, this case involves velocity averaging only in the upper part of the water column, following the approach employed by Broekema et al. (2019), for a fair comparison. In line with the previous scenarios, the model demonstrates good agreement with the lateral mixing layer profiles obtained from the measurement data and the plane bed reference case upstream of the slope. Furthermore, the model exhibits a satisfactory match with the measurement data on the leeside of the obstruction

whereby the velocity increases over streamwise distance demonstrating the lateral exchange of momentum with the main flow.
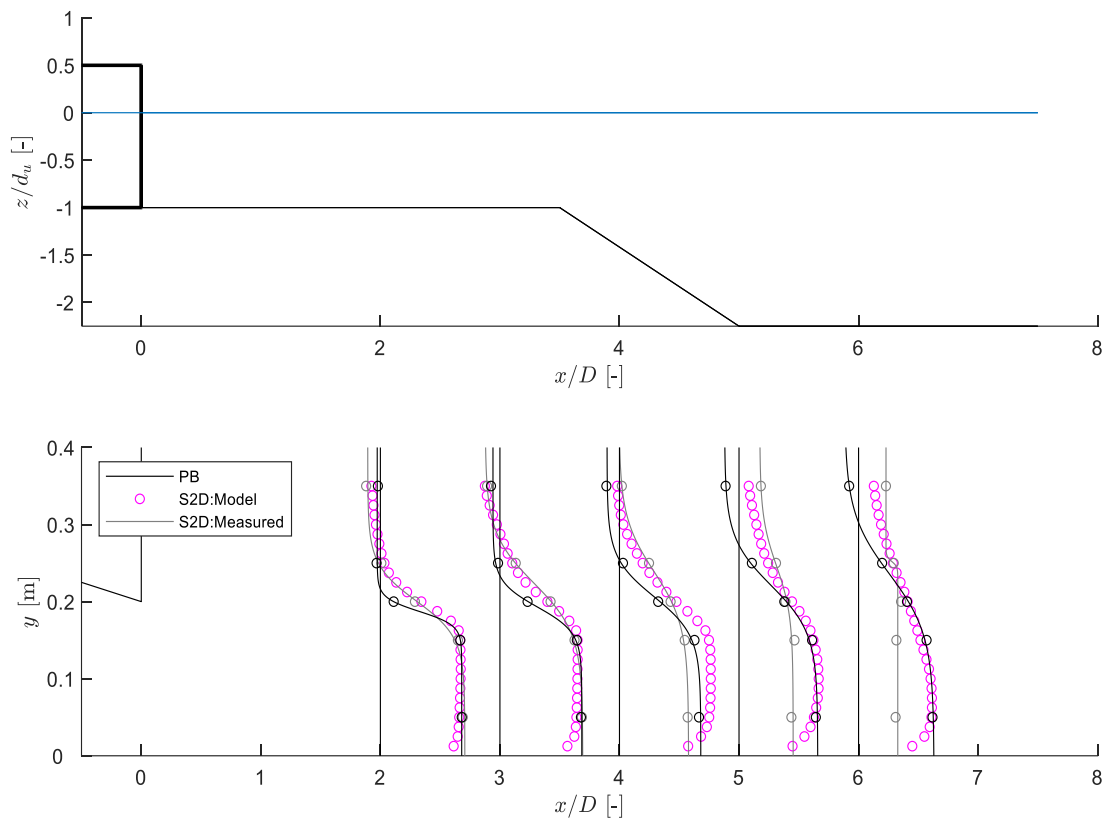
Figure 31: Lateral mixing layer profile of the depth-averaged streamwise velocity of the model and measurement, over the upper part of the water column, as a function of streamwise distance. The measurements are plotted in both solid lines (fitted hyperbolic-tangent profile) and round markers (measured) for cases PB and S2D. The top panel guides the reader regarding the position of the slope.

A substantial deviation between the measurement data and the plane bed mixing layer becomes apparent around the slope ($x/D \geq 4$). This disparity was attributed to the heightened energy dissipation between the mixing layer and the vertical recirculation zone (Broekema et al., 2019). Conversely, the model exhibits a closer agreement with the plane bed case, particularly on the high-velocity side of the domain. This correspondence supports the notion that, in the model, the development of the horizontal mixing layer in a separating flow case resembles that of a plane bed mixing layer without the additional energy dissipation between the main flow and the vertical recirculation zone (Broekema et al., 2019). Such observations suggest a potential underestimation of the vertical recirculation zone, resulting in an underestimated energy dissipation and mixing.

Downstream of the slope ($x/D > 5$), the measurement data reveal a disappearing horizontal mixing layer, primarily attributed to the vertical mixing of streamwise momentum from the main flow (Broekema et al., 2019). Interestingly, the model exhibits a persistent horizontal mixing layer in the downstream region, similar to the plane bed reference case. Figure 32d also shows a growing mixing layer width instead of

diminishing. This finding aligns with the argument that the numerical model underestimates the mixing phenomena.

The disparities between the model and the measurement data also manifest themselves in the individual mixing layer properties, as shown in Figure 32. Consistent with the previous cases, the model encounters challenges in accurately representing velocity differences and the subsequent streamwise development of the mixing layer width. However, unlike the previous cases, in case S2D, the velocity differences of the model are higher than that of the measurement data over streamwise distance. As illustrated in Figure 31, the model's velocity at the lee-side of the obstruction increases with streamwise distance and aligns reasonably well with the measurement data, while the velocity remains high in the high-velocity side of the flow. Consequently, the velocity difference remains high instead of decreasing as expected based on the measurements. This discrepancy highlights the model's likely underestimation of turbulence and the associated energy dissipation between the main flow and the recirculation zone. This will be further investigated in Section 4.3.4.
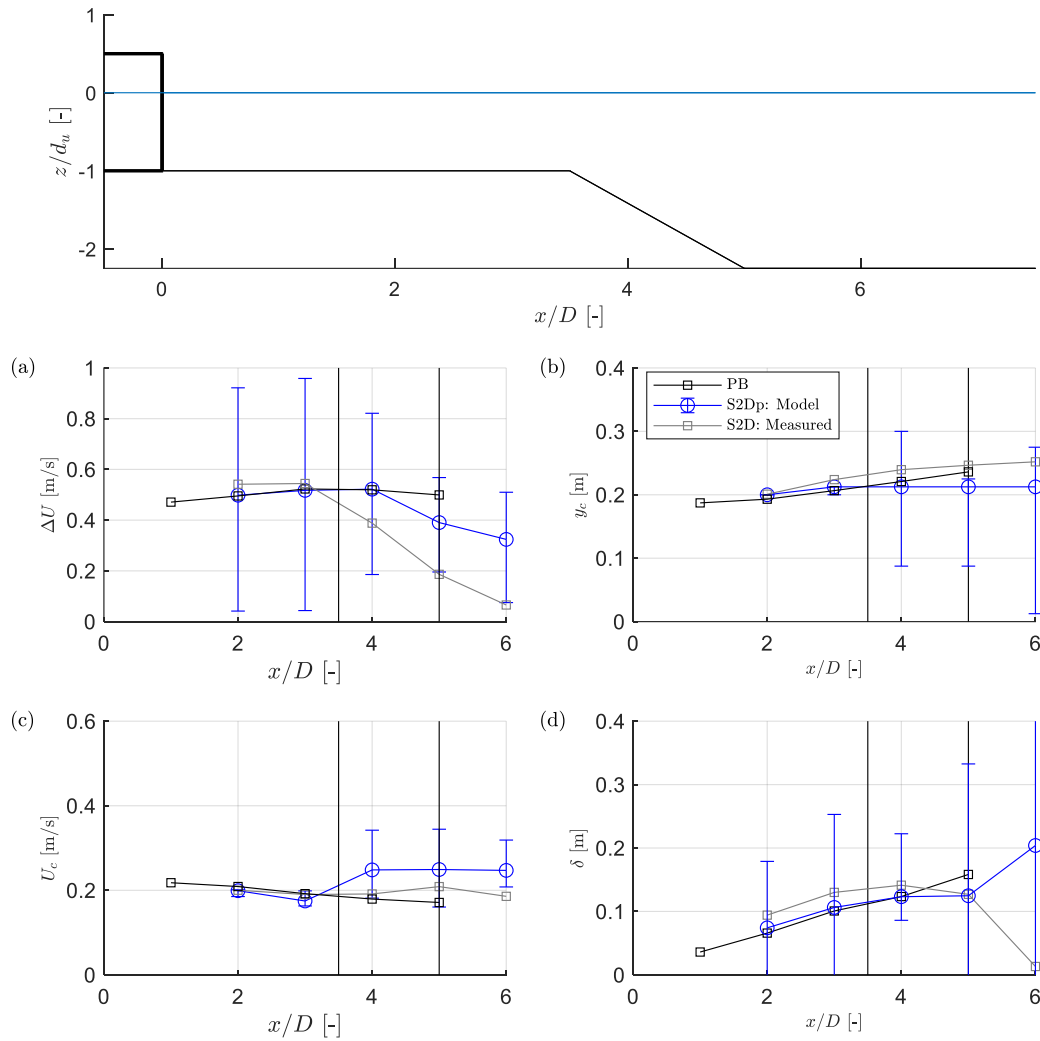
Figure 32: The individual mixing layer properties of depth-averaged streamwise velocity, over the upper part of the water column, of case S2Dp. (a) The velocity difference between the high- and low-velocity side of the mixing layer; (b) the lateral centreline position of the mixing layer; (c) the velocity at the centreline of the mixing layer; (d) the mixing layer width. The solid black line represents the upstream and downstream edges of the slope.

The fluctuative behaviour observed in the simulation, as evidenced by the presence of error bars, warrants careful consideration. However, it is difficult to determine the precise causes behind these fluctuations. It is important to recognize that the measurement data presented in the figures are also time-averaged quantities, which introduces the possibility that they too exhibit a range of values similar to those observed in the simulation. Additionally, most of the fluctuations happen in areas of high turbulence, which is around the slope. This implies that the fluctuations seen in the model may be attributed to the inherent variability of the flow rather than being solely a feature of the simulation. Another possibility is that the fluctuations arise from numerical instabilities inherent in the simulation methodology as the numerical model may

63

encounter challenges in accurately capturing the intricate dynamics of highly unsteady flows.

4.3.4. Turbulence properties

In this section, the time-averaged turbulent kinetic energy (TKE) is analysed. TKE is defined as the mean kinetic energy per unit mass ($m^2 \, s^{-2}$) associated with the turbulent eddies, governed by the following equation (Pope, 2000):

$$k = \frac{1}{2}(\overline{u_i' u_i'})$$

<div align="right">(12)</div>

Here, u_i' denotes the fluctuating components of the velocity vector in the i-th direction and the overbar denotes a time-averaged quantity. First, an overview of how the modelled and measured TKE are distributed over the domain is shown for the vertically attaching case (S4A and S2A) and vertically separating case (S2Dp). Subsequently, a more detailed analysis focuses on the variation of TKE, particularly examining its streamwise and spanwise development near the surface and the bed. This analysis is motivated by the confinement of flow to the upper region of the water column in the case of vertically separating flow.

Case S4A and S2A

Figure 33 and Figure 34 present the modelled time-averaged TKE alongside the TKE computed from the velocity measurement data of Broekema et al. (2019) for case S4A and S2A, respectively. It is evident that the TKE obtained from the model is consistently underestimated throughout the domain in both cases and that the largest differences are observed at locations where also the most TKE is produced, which is around the slope. The measurement data indicate significantly higher levels of turbulence around the slope, indicating that for horizontally converging flows, the presence of the slope intensifies turbulence fluctuations (Broekema et al., 2019); with the steeper one inducing higher turbulence. Although the model shows a similar trend, the difference in the modelling result between case S4A and S2A is insignificant to claim that the steeper slope induces higher turbulence.
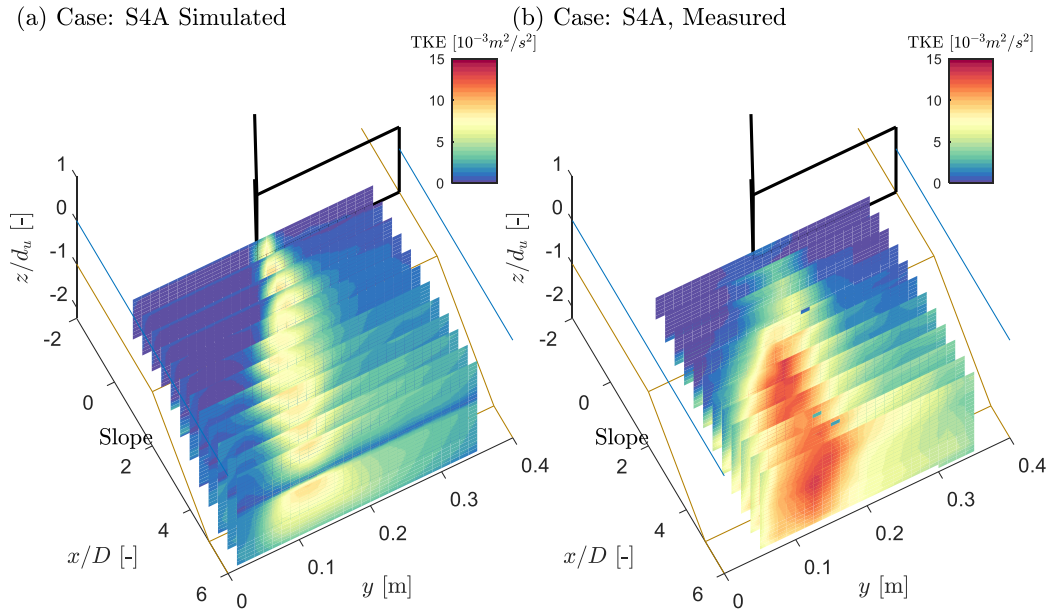
Figure 33: Time-averaged turbulent kinetic energy (TKE) of the case S4A over the domain. The left panel is obtained from the simulation while the right panel is constructed from the measurement data of Broekema et al. (2019).
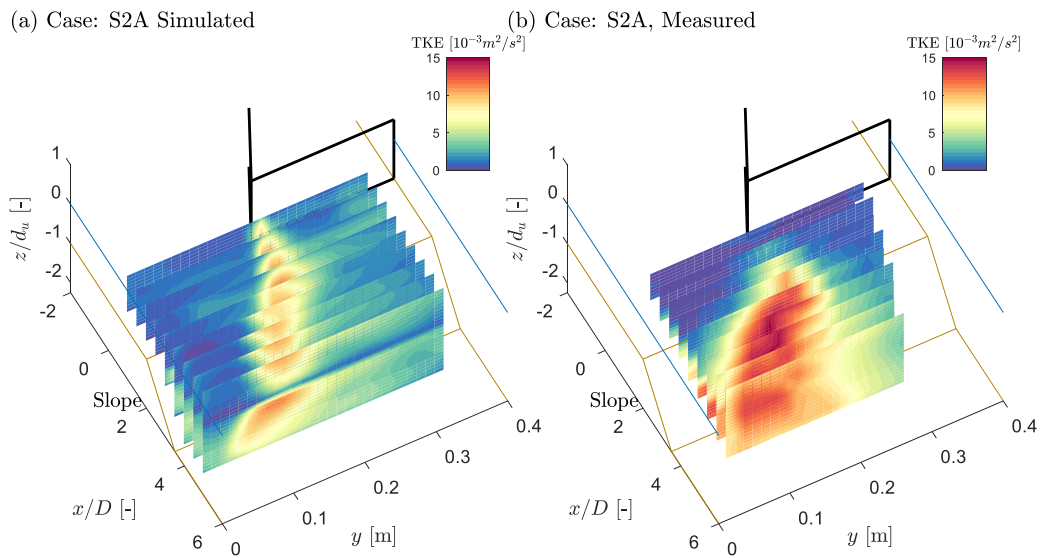
Figure 34: Time-averaged turbulent kinetic energy (TKE) of the case S2A over the domain. The left panel is obtained from the simulation while the right panel is constructed from the measurement data of Broekema et al. (2019).

Case S2Dp

A notable pattern in the TKE can be observed when comparing the vertically attached case with the vertically separated case. Figure 35 reveals a pronounced lateral expansion of TKE in the vertically separated case, aligning with the horizontal divergence of the flow previously discussed. The measurements also show that the vertically attached flow has higher turbulence intensities at the slope than its separated counterpart. However, in line with the other cases, the model consistently underestimates the TKE, signalling that this underestimation is likely to be inherent to the model itself.

(a) Case: S2Dp Simulated (b) Case: S2D Measured
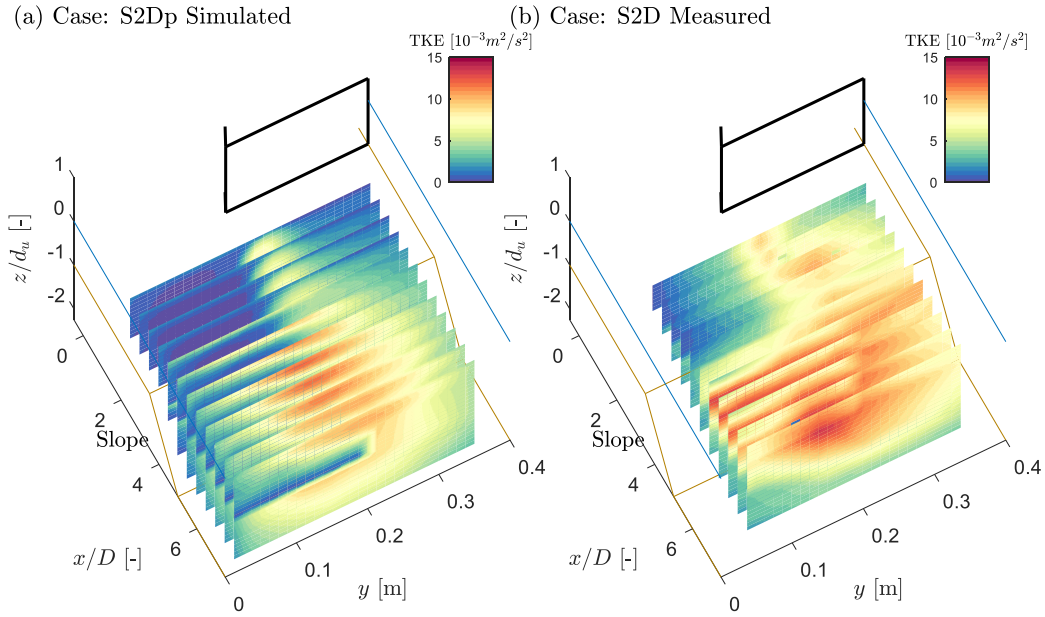
Figure 35: Time-averaged turbulent kinetic energy (TKE) of the case S2Dp over the domain. The left panel (a) is obtained from the simulation while the right panel (b) is constructed from the measurement data of Broekema et al. (2019).

In Section 4.3.3, a quantitative analysis was presented, demonstrating the evolution of the mixing layer over the streamwise distance. The findings suggest that the model lacks turbulence at the interface between the main flow and the recirculation zone, which plays a role in energy dissipation and the subsequent decrease in velocity at the high-velocity side of the flow. This hypothesis gains support from Figure 36, where it is evident that the model fails to capture the high turbulence at the upper part of the water column and also at the interface which is responsible for the energy dissipation. One can also see that the high turbulence region of the measurements in Figure 36 corresponds to the reduced velocity at the same region in Figure 24, which supports that turbulence is what drives this energy dissipation and velocity reduction.

Additionally, it can be argued that the model might have lacked the resolution to accurately represent the gradient between the main flow and the recirculation zone, given the very distinct confinement between the upper and lower region of the flow, which deviates from the continuous nature of the actual flow. The observed absence of turbulence at the interface may have resulted in a significant limitation of the model.
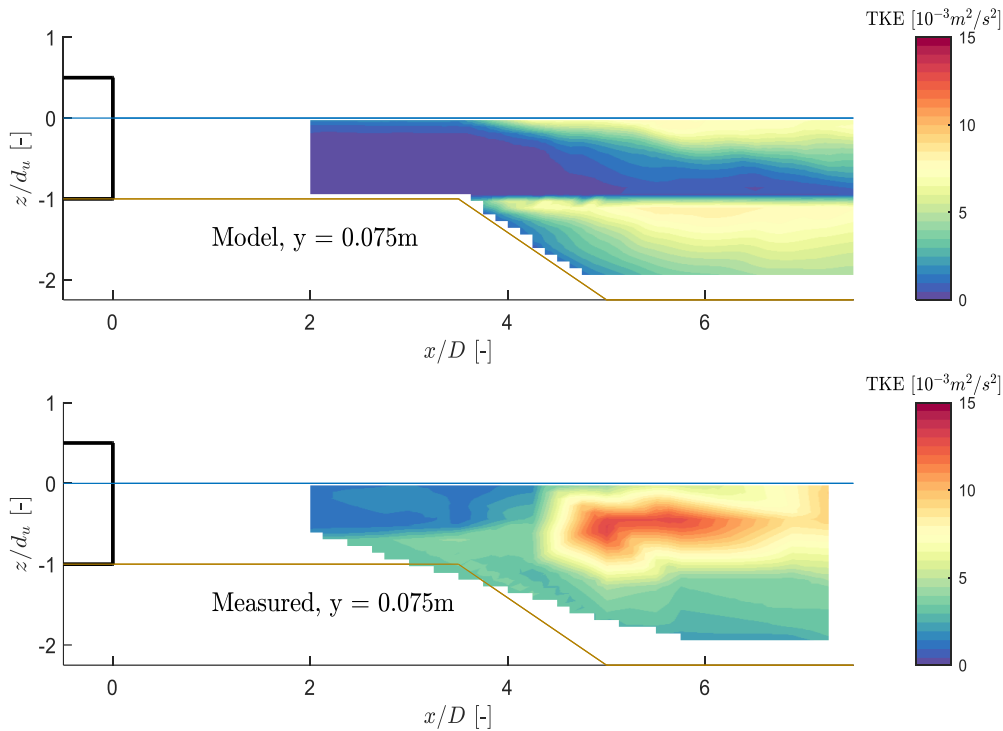
Figure 36: Side view of TKE at the high-velocity side of the separating case S2Dp. The top panel shows the results from the model while the bottom panel shows the measurement data.

The TKE is investigated further, isolating the TKE near surface and bed over the streamwise distance (Figure 37 and Figure 38) and along the spanwise distance (Figure 39). Analysed below are all the cases along the high- and low-velocity side of the flow domain. For convenience, the upstream edge of the slope is denoted as the origin ($x = 0$). Figure 37 shows the development of the TKE over streamwise distance for case S2A (a,c) and case S4A (b,d); demonstrating how the increase in depth enhances turbulence intensities as well. As can be seen, consistent with the previous findings, the TKE of the model is overall underestimated, especially in the high-velocity side of the flow where the difference is nearly twice for the TKE near the bed (Figure 37a, b). This large deviation is mainly observed downstream of the slope ($x > 0$), where high turbulence is observed, which also supports the notion that the model only comes in good agreement with the model upstream of the slope, as also argued in Section 4.3.3.
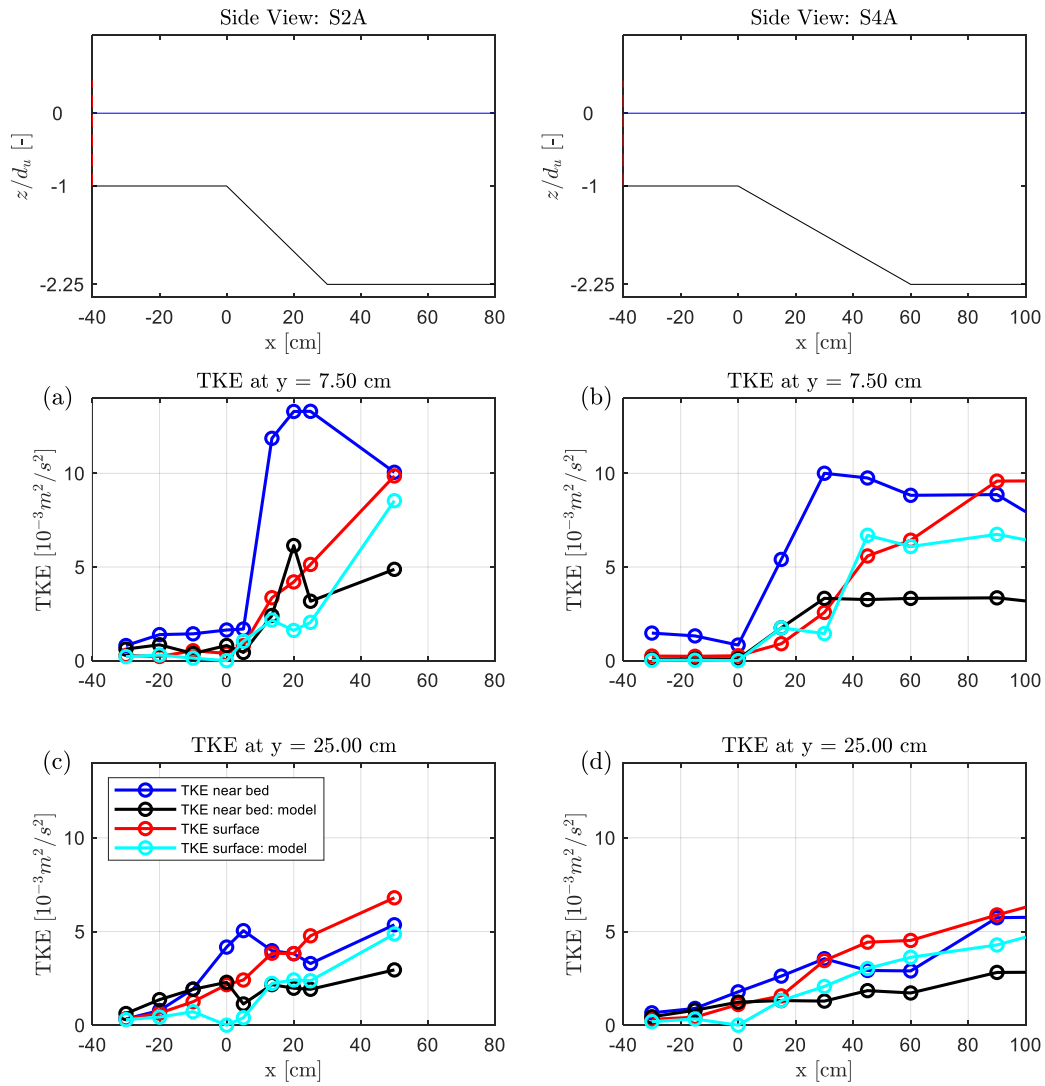
Figure 37:The development of TKE over streamwise distance of case S2A (a,b) and S4A (c,d) near the surface and near the bed along the high-velocity side and low-velocity side of the flow. The top panel guides the reader regarding the position of the slope of case S2A (left) and S4A (right)..

Figure 38 compares the streamwise development of TKE of case S2A and S2Dp. As can be seen, the TKE over streamwise distance is larger for the vertically-attached case, at least in the high-velocity side of the flow. Notable from Figure 38b is that the TKE of the model near the bed increases significantly at $x = 0$, which may signal that this is the point where the flow separates although this is slightly more difficult to judge from the measurement data, given the nearly uniform TKE near the bed.
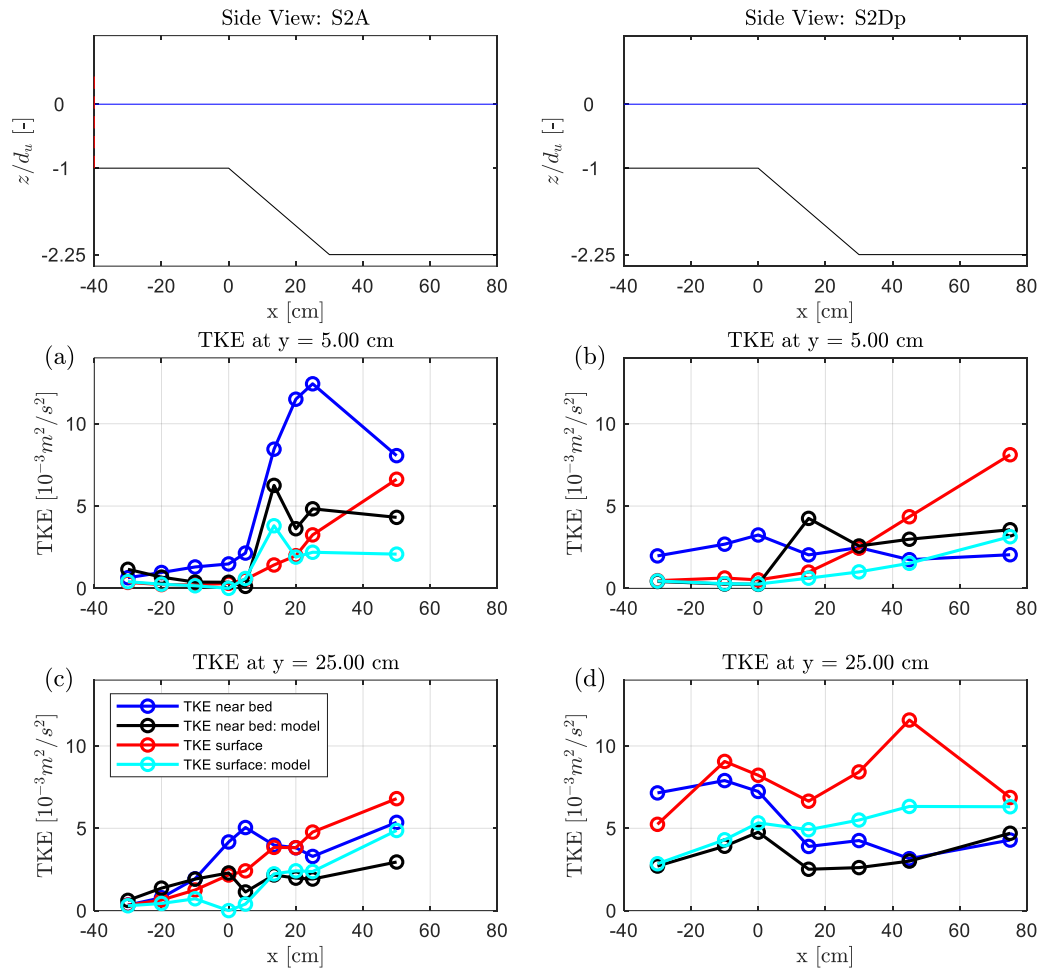
Figure 38: The development of TKE over streamwise distance of case S2A (a,b) and S2Dp (c,d) near the surface and near the bed along the high-velocity side and low-velocity side of the flow. The top panel guides the reader regarding the position of the slope of case S2A (left) and S2Dp (right).

Similarly, in the spanwise direction (Figure 39), the model produces less TKE than the measurement data. Moreover, the streamwise development of TKE is higher than that of the spanwise development. The consistent observation of smaller turbulence (structures) in all cases further highlight the limitation of the RANS approach. The assumption of turbulence isotropy in RANS implies that turbulence properties are independent of direction. However, turbulence properties vary in different directions. This assumption may have restricted the model's ability to accurately capture the turbulence, hence contributing to the observed discrepancies.
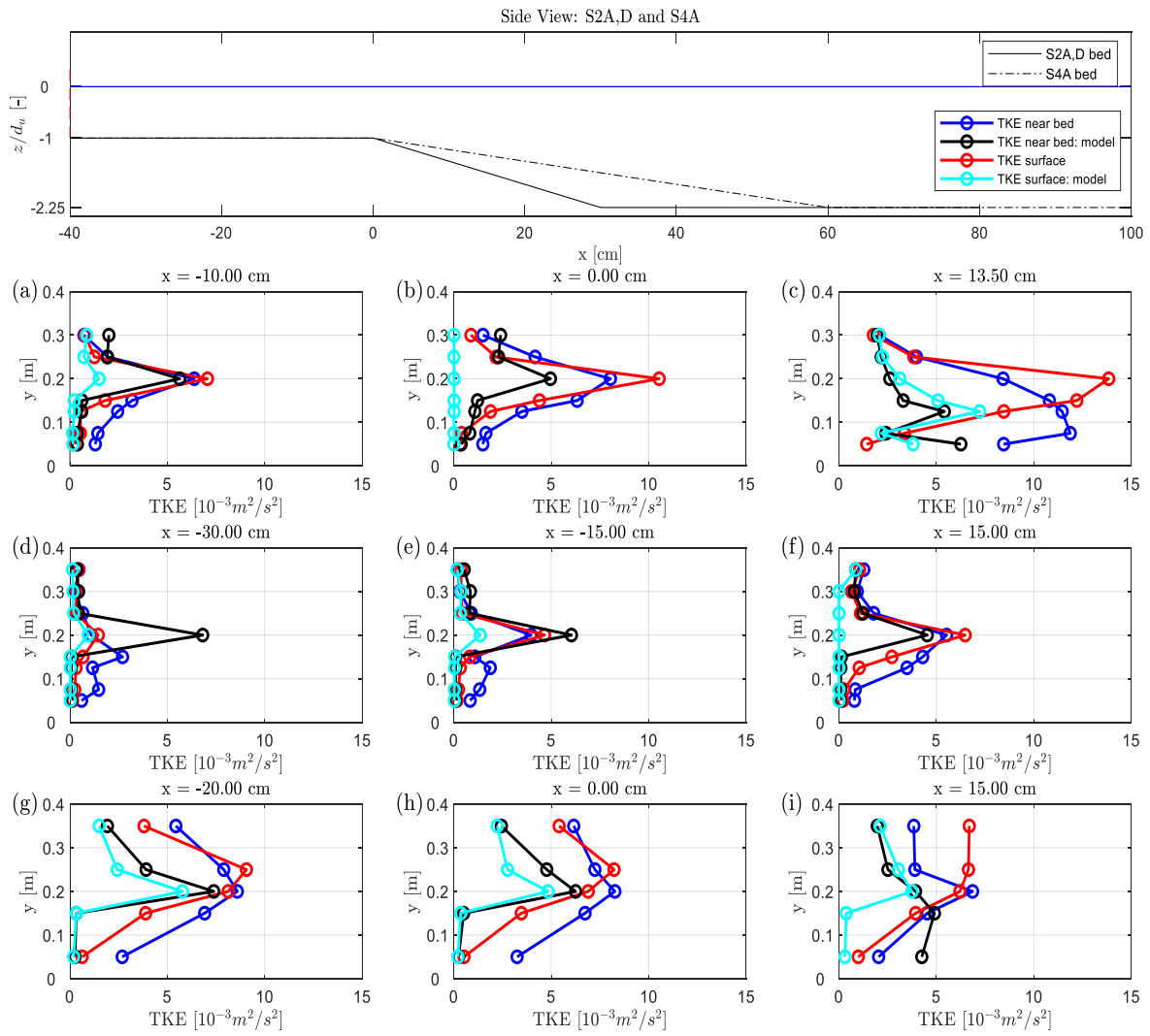
Figure 39: The development of the spanwise TKE of case S2A (a,b,c), S4A (d,e,f) and S2Dp (g,h,i) near the surface and near the bed. The top panel guides the reader regarding the position of the slope of case S2A and S2D (dashed black line) and S4A (solid black line).

5. Discussion

The present study aimed to investigate the flow characteristics and turbulence behaviour in a channel flow with a horizontal obstruction and sloping bed using numerical simulations. Multiple simulation cases were performed to study the two flow states identified by Broekema et al. (2019), namely 1) vertical flow attachment and horizontal convergence (case S4A and S2A) as well as 2) vertical flow separation and horizontal divergence (case S2Dp) to investigate how flow attachment is affected by the upstream flow field and the influence of the slope steepness. The former flow state was captured by the model as is, while the latter was achieved after adjustments in the position of the obstruction and the pressure outlet boundary condition. Throughout the analysis, several key findings and limitations have emerged, shedding light on the intricacies of the flow field and the performance of RANS turbulence modelling approach. In this discussion section, findings, implications, and the limitations of the RANS simulations are discussed.

5.1. The effect of horizontal obstruction placement

One of the key findings of this study is the observed relationship between the distance of the horizontal obstruction to the upstream edge of the slope (L_D) and flow separation. Placing the obstruction further upstream allows for the mixing layer to develop over further distance as it approaches the slope. As the mixing layer propagates, transverse exchange of mass and momentum occurs (van Prooijen & Uijttewaal, 2002) which reduces the lateral velocity gradient, leading to horizontal divergence of the flow (i.e., resulting in a horizontally uniform flow) and allowing for flow separation to happen.

The fact that flow separation occurs by placing the obstruction further upstream also suggests that the mixing process in the model operates slower compared to reality, as also evidenced by the lower turbulence generation. Consequently, the reduction in the lateral velocity gradient is not as significant, requiring the obstruction to be positioned further upstream to attain adequate mixing and a sufficient reduction in the velocity gradient which gives rise to flow divergence and subsequent flow separation. The simulated vertically attaching case also supports this notion. When the obstruction is placed closer to the slope, the mixing layer has shorter distance to develop which results in a large lateral non-uniformity that leads to vertical flow attachment. Thus, this research supports the notion that the occurrence of boundary layer separation is influenced by the lateral non-uniformity and mixing of the upstream flow field.

5.2. Flow separation and adverse pressure gradient

Flow separation in case S2D was observed by adjusting the pressure outlet boundary conditions with the $k - \omega$ SST model, while the $k - \varepsilon$ model does not show any improvement (Appendix C), highlighting that the $k - \omega$ SST model is more suitable for simulating flow separation (Hanjalic, 2004; Versteeg & Malalasekera, 2007).

This study highlighted the observed relationship between the pressure field and flow separation. In all vertically separating cases (both case S2Dp and the simulation where with the obstruction placed further upstream), an adverse pressure gradient was observed upstream and downstream of the slope, where the flow depth increases, causing flow deceleration. Conversely, during flow attachment, the pressure prior to the slope decreases indicating flow acceleration as the flow converges horizontally. Consequently, the deceleration of the flow due to the increased depth at the slope is reduced, resulting in a diminished adverse pressure gradient and the attachment of the boundary layer to the bed.

According to Broekema et al. (2019), their observations suggest that vertical flow separation is influenced not only by adverse pressure gradient but also by enhanced energy dissipation. However, considering the substantial underestimation of turbulence and the largely absent energy dissipation identified in this study, it appears that the adverse pressure gradient plays a more significant role in flow separation. Nevertheless, the discrepancy between the findings of this study and the previous observations highlights the need for further investigation to gain a clearer understanding of the mechanisms driving flow separation. Further studies, whether it be through complementary experimental measurements or advanced numerical models such as LES that may simulate turbulence structures more accurately is recommended to better quantify the contributions of the adverse pressure gradient and energy dissipation in driving flow separation.

5.3.   On mixing layer and turbulent kinetic energy

The findings discussed above indirectly emphasize the important role of the mixing layer (and mixing) in determining flow separation or attachment. The mixing layer of the model generally exhibited good agreement with the measurements upstream of the slope in all cases. However, disparities between the model and the measurements became more pronounced over the slope, which is characterized by higher turbulence intensities, as discussed in Section 4.3.4. The case of flow separation (S2Dp) exhibited the greatest discrepancy in the mixing layer profile compared to the measurement data, where the model result instead closely resembled that of the plane bed case. This discrepancy can be attributed to the model's underestimation of turbulence and the associated energy dissipation between the main flow and the vertical recirculation zone. This is particularly evident at the interface of the main flow and the vertical recirculation zone, where based on the measurements, high turbulence intensities are expected due to the presence of large gradients in the streamwise flow velocity field; but was rather underestimated or missing in the model. These gradients enhance the development and growth of instabilities into large eddies, contributing to increased turbulence. However, as discussed in Section 4.3.4, the model significantly underpredicts the levels of turbulence in this region.

This inadequate representation of turbulence by the model results in inaccurate flow dynamics in the vertically separating flow scenario. Not only does turbulence plays a role in energy dissipation, but it also has a role in mixing (and mixing layer) as it influences the exchange of mass and momentum between the main flow and the recirculation zone. Hence, by underpredicting the turbulence, the model was not able to accurately capture the intensification and growth of instabilities into large eddies, which are responsible for enhanced turbulence and energy dissipation. The underpredicted turbulence also makes it difficult, in the vertically attaching cases, to ascertain whether the slope does intensify turbulence or whether or not it is mainly advected from the upstream flow field since the difference in TKE between the milder (1:4 slope) and steeper slope (1:2 slope) is not significant.

5.4.   Limitations

This research is subject to several limitations that should be acknowledged. Firstly, the achievement of grid independence was not properly demonstrated. The flaws in the meshing process introduced errors into the solution, as evidenced by the higher MAE and RMSE obtained with finer meshes. As a result, the analysis of this thesis had to rely on the medium-resolution mesh, which exhibited the least error. Meanwhile, it is expected that finer meshes would provide results closer to the measurement data.

Additionally, the refinement of the time-step was not implemented as the mesh became more refined, which can be considered a human error. However, the influence of this factor on the solution is difficult to assess since OpenFOAM adjusts the time steps automatically during the simulation as determined by the Courant number. The choice of a Courant number of 3 may seem unconventional at first. However, this choice seemed to be justified by the consistent convergence of solutions for all the cases examined. Moreover, an additional case where the Courant number was lowered to 0.7 with the medium mesh did not yield significant improvements, considering the significantly higher computational resources required for such simulations. Furthermore, the investigation did not delve into the numerical schemes and other solver settings, such as the under-relaxation parameters, which could have potentially improved the solution obtained from the model. Nonetheless, due to time constraints, it was not possible to redo the simulations with the finer meshes nor smaller time-step, which may limit the accuracy and precision of the results.

Moreover, a consistent observation throughout the study was the presence of smaller turbulence intensities (TKE) in all simulated cases, highlighting a limitation of the RANS approach. Despite its prevalence, the RANS turbulence models have inherent limitations when it comes to capturing unsteady flow characteristics such as flow separation and vortex shedding (Li et al., 2013; Sumner et al., 2010; Thé & Yu, 2017). Firstly, RANS models tend to exhibit high viscosity within the boundary layer, leading to reduced turbulence levels and an overprediction of the attached flow regions (Johansen et al., 2002). This limitation hampers the accurate representation of flow separation phenomena. Secondly,

the Boussinesq approximation employed in RANS models assumes isotropy, while turbulent flows are inherently anisotropic in nature (Versteeg & Malalasekera, 2007). As a result, the ability of RANS models to adequately capture vortex shedding, a fundamental aspect of unsteady flow separation, is compromised (Mehta et al., 2014).

The assumption of turbulence isotropy in two-equation turbulence models such as the $k - \omega$ SST implies that turbulence properties are directionally independent, which does not accurately reflect the actual behaviour of turbulence. Meanwhile, shallow shear flows are characterized by the anisotropy of turbulence motion (van Prooijen & Uijttewaal, 2002). Additionally, the turbulence model falls short in capturing the subtle relationships between turbulent energy production and turbulent stresses arising from the anisotropy of the normal stresses (Versteeg & Malalasekera, 2007); especially in modelling the Reynolds stresses after separation (Constantinescu et al., 2003). Additionally, although the model was able to reproduce the general features of the flow, Nagata et al. (2005), argued that such isotropic turbulence is not suitable for flows past an obstacle whereby the three-dimensional flow plays a significant role. Including anisotropic turbulence may result in more accurate prediction of normal Reynolds stress and thus turbulence intensities (Thangam & Speziale, 1991). Hence, this assumption may have restricted the model's ability to capture turbulence characteristics accurately, contributing to the observed discrepancies in this study. Additionally, it could also be the case that the simulation should have run longer to allow for the turbulence to be fully developed.

5.5. Recommendations

The limitation of the RANS model, whereby all turbulence length scales are modelled simultaneously, hinders a comprehensive examination of turbulence representing and associated with the mixing layer; thereby lacking the resolution required to capture the energy transfer between larger and smaller turbulence scales (Talstra, 2011) hence hindering the interaction between 2DCS and bottom turbulence. Based on the significance of the mixing layer and the associated turbulence, according to the findings of this research and Broekema et al. (2019), it is recommended that future research endeavours focus on enhancing the model's capability to accurately resolve turbulence characteristics within the mixing layer at the interface between the main flow and the recirculation zone. One possible approach is to consider higher-resolution models such as Detached Eddy Simulation (DES) or LES, which can directly capture the energy-carrying turbulent scales and the smaller dissipative ones through parameterization.

The simulations conducted in this study employed the rigid-lid assumption, which excluded the modelling of the air-water interface and changes in the water surface. This limitation should be acknowledged as it may affect the accuracy of the simulation results. In a study by Khosronejad et al., (2019), a comparison was made between rigid-lid and free-surface (Level-Set method) LES simulation of a flow past an abutment, with Reynolds (7.9×10^4) and Froude (0.36) number comparable to this research and Broekema et al. (2019). The presence of the abutment was found to locally increase the

Froude number, causing a transition from subcritical to supercritical flow. This led to backwater effects in the upstream region, where the water level upstream of the obstruction increased while the downstream regions experienced a drop in flow depth by about 10-15% of the mean flow depth (Khosronejad et al., 2019). The rigid-lid model showed flow acceleration due to the constriction, but less pronounced than its free-surface counterpart, which exhibited a drop in water surface leading to higher near-bed turbulent kinetic energy. Downstream of the constriction, the free-surface simulation revealed highly fluctuating water surface, associated with the breakdown of high-energy vortical structures near the surface and a significant increase in vertical turbulent stresses $(\overline{w'w'})$ near the surface (Khosronejad et al., 2019). These findings could be similar to the coherent structures identified by Broekema et al. (2019) as contributors to the energy dissipation in the vertically separating case. It can also be argued that as energy dissipates, not only does kinetic energy decrease with flow deceleration, but potential energy and water level also decrease to give the total energy loss. However, these water surface dynamics were not captured in the present study due to the rigid-lid assumption.

The study of Khosronejad et al., (2019) concluded that resolving the free surface has an impact on both the computed first-order (i.e., the velocity components) and second order (i.e., the Reynolds stress tensor and TKE) turbulence statistics, leading to more accurate results. Under similar geometry and flow conditions to of Khosronejad et al., (2019) , Kara et al., (2015) supported this notion, though in a smaller scale experiment ($Re = 6.1 \times 10^3$), demonstrating non-negligible difference in the second-order turbulence statistics between free-surface and rigid-lid simulations due to the disparity in 3D turbulence structures. The free-surface LES simulations revealed stretched turbulence structures caused by local flow acceleration and strong deformations of the water surface, where once more the water level downstream of the obstruction dips due to backwater effects and the local increase in the Froude number. As a result of this dip and vortex stretching, the near-bed turbulent kinetic energy was considerably higher than its rigid-lid counterpart. The vortex stretching led to a higher streamwise and lower spanwise Reynolds stresses in the free-surface simulation compared to the rigid-lid simulation (Kara et al., 2015) which didn't have the vortex stretching. Interestingly, the higher streamwise and lower spanwise Reynolds stresses are consistent with the findings of Broekema et al. (2019) which suggests a compelling relationship between the flow conditions observed in Broekema et al. (2019) with vortex stretching that can be addressed in future research efforts.

Furthermore, Khosronejad et al. (2019) suggested that backwater effects were the primary cause of discrepancy between rigid-lid and free-surface computations, emphasizing the need to resolve the free surface when backwater effects are expected. Considering the limitations of the rigid-lid assumptions and the insights provided by other studies, it becomes evident that incorporating a free-surface model could potentially enhance the accuracy of simulations. Therefore, future research should

consider utilizing free-surface LES not only to capture the influence of water surface fluctuations but also the associated turbulent kinetic energy.

5.6.   Outlook

The present research shows that the two flow states identified by Broekema et al. (2019), namely 1) vertical flow attachment and horizontal convergence (case S4A and S2A) and 2) vertical flow separation and horizontal divergence (case S2D), can be reproduced through RANS simulations, although not wholly satisfactory.

This thesis demonstrated dependencies between the upstream flow conditions (i.e., flow divergence and convergence) and the flow states at the slope (i.e., vertical flow separation and attachment), highlighting the influence of the lateral velocity gradient and the role of horizontal obstruction placement. The underestimation of turbulence and slower mixing observed in the model compared to reality warrants the need for further investigation into turbulence generation, to which this study recommends using higher-resolution numerical modelling such as LES, to overcome the limitations of RANS turbulence models. This research advocates for expanding the range of flow configurations, such as slope angles and spacing between the horizontal obstruction and the upstream edge of the slope, to provide a more comprehensive understanding of their respective impacts and aid in identifying the transition point between the two flow states. Other parameters such as densities and supercritical flow can also be considered.

6. Conclusion

In conclusion, this research aimed to investigate the flow characteristics and turbulence behaviour in a channel flow with a horizontal obstruction, similar to that of Broekema et al., (2019) using numerical simulations, namely the RANS turbulence model. Two solvers were tested, namely the SIMPLE and PIMPLE algorithms. The SIMPLE algorithm, being a steady-state solver, was not able to converge which this research attributes to the unsteady nature of the flow which prevents the residuals from reaching the desired level as the solution attempts to reach for a steady state that does not exist. This hypothesis was confirmed by using the PIMPLE algorithm, which consistently reached convergence in every time step for all cases and demonstrated agreement with the measurements.

With the PIMPLE algorithm and the $k - \omega$ SST turbulence closure model, the RANS simulations were able to represent the overall flow characteristics of the measured flow, although not wholly satisfactory. The vertically separating flow was achieved by adjusting the pressure outlet boundary conditions or adjusting the position of the horizontal obstruction further upstream. With the former adjustment, the $k - \omega$ SST model exhibited improved agreement with the measured data, showing flow divergence and flow separation phenomena. On the other hand, the $k - \varepsilon$ model (Appendix C) did not demonstrate any improvement, highlighting that the $k - \omega$ SST is better suited for this flow phenomenon.

The comparison between the model and measurement data revealed limitations in the RANS modelling approach, particularly in accurately capturing turbulence characteristics. Although the model showed good agreement with the measurement data upstream of the slope in all cases, significant disparities were observed in the sloping region where turbulence intensities were highest, according to the measurements. The turbulent kinetic energy was consistently underpredicted in all cases. This discrepancy makes it challenging to assess whether the presence of a steeper slope leads to increased turbulence in case the flow stays attached, as observed in Broekema et al., (2019). Particularly, in the case of vertical flow separation, the underestimation of turbulence had a substantial impact on the flow representation, as it failed to model turbulence associated with energy dissipation and mixing between the main flow and the vertical recirculation zone responsible for reducing the flow velocity at the high-velocity side of the flow.

The findings of this study have both theoretical and practical implications. The theoretical implications pertain to the understanding of the relationship between the distance of the horizontal obstruction from the upstream edge of the slope (L_D) on flow separation and attachment. Placing the obstruction further upstream allowed for the development of a mixing layer over a longer distance before the slope, resulting in a reduced lateral velocity gradient and horizontal divergence of the flow and ultimately flow separation. Conversely, when the obstruction was placed closer to the slope, a shorter distance for

the mixing layer development led to a larger lateral non-uniformity and vertical flow attachment. This observed relationship has potential practical relevance in the design of hydraulic structures. Given the presence of jet-like flows and the associated lateral velocity gradients near hydraulic structures, it is recommended that bed protections are sufficiently long to allow for sufficient mixing to occur. This allows for the reduction of velocity differences and turbulence intensities to trigger flow separation and prevent scouring to further develop.

The relationship between the pressure field and flow separation was also observed. This study identified the occurrence of adverse pressure gradients upstream and downstream of the slope in the vertically separating cases, indicating flow deceleration due to increased flow depth. In contrast, during flow attachment, the pressure decreased upstream of the slope, indicating flow acceleration and diminished adverse pressure gradients, allowing for the attachment of the boundary layer to the bed.

The limitations of the RANS approach in capturing anisotropic turbulence and energy transfer underscore the need for future research efforts to investigate higher model resolution for better accuracy in representing the turbulence characteristics. The recommendation to explore higher-resolution models such as DES and LES opens avenues for more detailed simulations and a better understanding of turbulence characteristics. Additionally, this research also suggests looking into free-surface modelling to capture the dynamics of the air-water interface and changes in water surface to better analyse the flow behaviours.

Bibliography

Ansari, A. (1997). Self-similarity and mixing characteristics of turbulent mixing layers starting from laminar initial conditions. *Physics of Fluids*, *9*(6), 1714–1728. https://doi.org/10.1063/1.869288

Babarutsi, S., Nassiri, M., & Chu, V. H. (1996). Computation of Shallow Recirculating Flow Dominated by Friction. *Journal of Hydraulic Engineering*, *122*(7), 367–372. https://doi.org/10.1061/(ASCE)0733-9429(1996)122:7(367)

Baker, C., Johnson, T., Flynn, D., Hemida, H., Quinn, A., Soper, D., & Sterling, M. (2019). Computational techniques. *Train Aerodynamics*, 53–71. https://doi.org/10.1016/B978-0-12-813310-1.00004-6

Bey, A., Faruque, M., & Balachandar, R. (2007). Two-Dimensional Scour Hole Problem: Role of Fluid Structures. *Journal of Hydraulic Engineering*, *133*(4), 414–430. https://doi.org/10.1061/(ASCE)0733-9429(2007)133:4(414)

Bijvelds, M. D. J. P., Kranenburg, C., & Stelling, G. S. (1999). 3D Numerical Simulation of Turbulent Shallow-Water Flow in Square Harbor. *Journal of Hydraulic Engineering*, *125*(1), 26–31. https://doi.org/10.1061/(ASCE)0733-9429(1999)125:1(26)

Breusers, H. N. C. (1967). Time scale of two dimensional local scour. *Proc. 12th Congress IAHR, Vol 3, Paper C32*. https://repository.tudelft.nl/islandora/object/uuid%3A72d3a33a-5a0e-4eac-b9a7-730bd7fb32c7

Broekema, Y. B., Labeur, R. J., & Uijttewaal, W. S. J. (2018). Observations and Analysis of the Horizontal Structure of a Tidal Jet at Deep Scour Holes. *Journal of Geophysical Research: Earth Surface*, *123*(12), 3162–3189. https://doi.org/10.1029/2018JF004754

Broekema, Y. B., Labeur, R. J., & Uijttewaal, W. S. J. (2019). Suppression of vertical flow separation over steep slopes in open channels by horizontal flow contraction. *Journal of Fluid Mechanics*, *885*, 8. https://doi.org/10.1017/JFM.2019.972

Brown, S. A., Greaves, D. M., Magar, V., & Conley, D. C. (2016). Evaluation of turbulence closure models under spilling and plunging breakers in the surf zone. *Coastal Engineering*, *114*, 177–193. https://doi.org/10.1016/J.COASTALENG.2016.04.002

Caretto, L. S., Gosman, A. D., Patankar, S. V., & Spalding, D. B. (1973). Two calculation procedures for steady, three-dimensional flows with recirculation. *Proceedings of the Third International Conference on Numerical Methods in Fluid Mechanics*, 60–68. https://doi.org/10.1007/BFB0112677

Constantinescu, G., Chapelet, M., & Squires, K. (2003). Turbulence modeling applied to flow over a sphere. *AIAA Journal*, *41*(9), 1733–1742. https://doi.org/10.2514/2.7291

Dargahi, B. (2010). Scour development downstream of a spillway. *Journal of Hydraulic Research*, *41*(4), 417–426. https://doi.org/10.1080/00221680309499986

Dietz, J. W. (1969). Kolksicherung am Elbewehr Geesthach. *Kolksicherung Durch Befestigungsstrecken Für Das Eidersiel*, *29*, 51–76. http://henry.baw.de/handle/20.500.11970/103057

Faragher, J. (2004). *Probabilistic Methods for the Quantification of Uncertainty and Error in Computational Fluid Dynamic Simulations*. https://apps.dtic.mil/sti/citations/ADA429143

Fluid Mechanics 101. (2019, April 15). *[CFD] What is the difference between y+ and y*?* https://www.youtube.com/watch?v=nSdVaF3JnI0

Ghodsian, M., & Vaghefi, M. (2009). Experimental study on scour and flow field in a scour hole around a T-shape spur dike in a 90° bend. *International Journal of Sediment Research*, *24*(2), 145–158. https://doi.org/10.1016/S1001-6279(09)60022-6

Guan, D., Melville, B. W., Asce, M., & Friedrich, H. (2013). Flow Patterns and Turbulence Structures in a Scour Hole Downstream of a Submerged Weir. *Journal of Hydraulic Engineering*, *140*(1), 68–76. https://doi.org/10.1061/(ASCE)HY.1943-7900.0000803

Hanjalic, K. (2004). *Closure models for incompressible turbulent flows* (C. Benocci & J. van Beeck, Eds.). Von Karman Lecture Series 2004/2005: Von Karman Institutes Fluid Dynamics.

Hoffmans, G., & Booij, R. (2010). Two-dimensional mathematical modelling of local-scour holes. *Journal of Hydraulic Research*, *31*(5), 615–634. https://doi.org/10.1080/00221689309498775

Hoffmans, G., & Verheij, H. (2021). *Scour Manual : Current-Related Erosion* (G. J. C. M. Hoffmans & H. J. Verheij, Eds.). CRC Press. https://doi.org/10.1201/B22624

Hu, H. H. (2012). Computational Fluid Dynamics. *Fluid Mechanics*, 421–472. https://doi.org/10.1016/B978-0-12-382100-3.10010-1

Issa, R. I. (1986). Solution of the implicitly discretised fluid flow equations by operator-splitting. *Journal of Computational Physics*, *62*(1), 40–65. https://doi.org/10.1016/0021-9991(86)90099-9

Jaramillo Ibarra, J. Ernesto., Oliva, Asensio., Pérez Segarra, C. David., & Universitat Politècnica de Catalunya. Departament de Màquines i Motors Tèrmics. (2008). Suitability of different RANS models in the description of turbulent forced convection flows: application to air curtains. *TDX (Tesis Doctorals En Xarxa).* https://upcommons.upc.edu/handle/2117/94007

Jirka, G. H. (2001). Large scale flow structures and mixing processes in shallow flows. *Journal of Hydraulic Research*, *39*(6), 567–573. https://doi.org/10.1080/00221686.2001.9628285

Johansen, J., Sørensen, N. N., Michelsen, J. A., & Schreck, S. (2002). Detached-eddy simulation of flow around the NREL Phase VI blade. *Wind Energy*, *5*(2–3), 185–197. https://doi.org/10.1002/WE.63

Kara, S., Kara, M. C., Stoesser, T., & Sturm, T. W. (2015). Free-Surface versus Rigid-Lid LES Computations for Bridge-Abutment Flow. *Journal of Hydraulic Engineering*, *141*(9). https://doi.org/https://doi.org/10.1061/(ASCE)HY.1943-7900.0001028

Khosronejad, A., Ghazian Arabi, M., Angelidis, D., Bagherizadeh, E., Flora, K., & Farhadzadeh, A. (2019). Comparative Hydrodynamic Study of Rigid-Lid and Level-Set Methods for LES of Open-Channel Flow. *Journal of Hydraulic Engineering*, *145*(1). https://doi.org/https://doi.org/10.1061/(ASCE)HY.1943-7900.0001546

Kim, S.-E., Choudhury, D., Division, A. F. E., & Engineers, J. S. of M. (1995). A Near-Wall Treatment Using Wall Functions Sensitized to Pressure Gradient. In *Separated and complex flows, ASME -PUBLICATIONS- FED, Symposium; Fluids engineering and laser anemometry conference, Separated and complex flows* (Vol. 217). ASME; https://www.tib.eu/de/suchen/id/BLCP%3ACN013245860

Koshizuka, S., Shibata, K., Kondo, M., & Matsunaga, T. (2018). Fundamentals of Fluid Simulation by the MPS Method. *Moving Particle Semi-Implicit Method*, 25–109. https://doi.org/10.1016/B978-0-12-812779-7.00002-3

Launder, B. E., & Spalding, D. B. (1974). The numerical computation of turbulent flows. *Computer Methods in Applied Mechanics and Engineering*, *3*(2), 269–289. https://doi.org/10.1016/0045-7825(74)90029-2

Li, C., Zhu, S., Xu, Y. L., & Xiao, Y. (2013). 2.5D large eddy simulation of vertical axis wind turbine in consideration of high angle of attack flow. *Renewable Energy*, *51*, 317–330. https://doi.org/10.1016/J.RENENE.2012.09.011

Lü, X., Lu, T., Yang, T., Salonen, H., Dai, Z., Droege, P., & Chen, H. (2021). Improving the Energy Efficiency of Buildings Based on Fluid Dynamics Models: A Critical Review. *Energies 2021, Vol. 14, Page 5384*, *14*(17), 5384. https://doi.org/10.3390/EN14175384

McDavid, R. M. (2001). Macroscopic Modeling. *Encyclopedia of Materials: Science and Technology*, 4720–4732. https://doi.org/10.1016/B0-08-043152-6/00823-8

Mehta, D., van Zuijlen, A. H., Koren, B., Holierhoek, J. G., & Bijl, H. (2014). Large Eddy Simulation of wind farm aerodynamics: A review. *Journal of Wind Engineering and Industrial Aerodynamics*, *133*, 1–17. https://doi.org/10.1016/J.JWEIA.2014.07.002

Menter, F. R. (2012). Two-equation eddy-viscosity turbulence models for engineering applications. *AIAA Journal*, *32*(8), 1598–1605. https://doi.org/10.2514/3.12149

Molland, A. F., & Turnock, S. R. (2007). Theoretical and numerical methods. *Marine Rudders and Control Surfaces*, 233–311. https://doi.org/10.1016/B978-075066944-3/50009-3

Nagata, N., Hosoda, T., Nakato, T., & Muramoto, Y. (2005). Three-Dimensional Numerical Model for Flow and Bed Deformation around River Hydraulic Structures. *Journal of Hydraulic Engineering*, *131*(12), 1074–1087. https://doi.org/https://doi.org/10.1061/(ASCE)0733-9429(2005)131:12(1074)

Neill, S. P., & Hashemi, M. R. (2018). Ocean Modelling for Resource Characterization. *Fundamentals of Ocean Renewable Energy*, 193–235. https://doi.org/10.1016/B978-0-12-810448-4.00008-2

Nieuwstadt, F. T. M., Boersma, B. J., & Westerweel, J. (2016). Turbulence: Introduction to Theory and Applications of Turbulent Flows. *Turbulence: Introduction to Theory and Applications of Turbulent Flows*, 1–284. https://doi.org/10.1007/978-3-319-31599-7

Norton, T., Grant, J., Fallon, R., & Sun, D. W. (2010). Optimising the ventilation configuration of naturally ventilated livestock buildings for improved indoor environmental homogeneity. *Building and Environment*, *45*(4), 983–995. https://doi.org/10.1016/J.BUILDENV.2009.10.005

Pereira, F. S., Eça, L., Vaz, G., & Girimaji, S. S. (2021). Toward Predictive RANS and SRS Computations of Turbulent External Flows of Practical Interest. *Archives of Computational Methods in Engineering 2021 28:5*, *28*(5), 3953–4029. https://doi.org/10.1007/S11831-021-09563-0

Pope, S. B. (2000). *Turbulent Flows*. Cambridge University Press. https://doi.org/doi:10.1017/CBO9780511840531

Rapp, B. E. (2017). Fluids. *Microfluidics: Modelling, Mechanics and Mathematics*, 243–263. https://doi.org/10.1016/B978-1-4557-3141-1.50009-5

Rogers, M. M., & Moser, R. D. (1994). Direct simulation of a self-similar turbulent mixing layer. *Physics of Fluids*, *6*(2), 903–923. https://doi.org/10.1063/1.868325

Schiereck, G. J. (2012). Introduction to bed, bank and shore protection (2nd edition). *Collegedictaat CIE4310*. http://resolver.tudelft.nl/uuid:7e6e6425-8304-4992-96be-aa277811f616

Sharif Ahmadian, A. (2016). Numerical Methods and Procedures. *Numerical Models for Submerged Breakwaters*, 93–108. https://doi.org/10.1016/B978-0-12-802413-3.00006-7

Sumner, J., Watters, C. S., & Masson, C. (2010). CFD in wind energy: The virtual, multiscale wind tunnel. *Energies*, *3*(5), 989–1013. https://doi.org/10.3390/EN3050989

Talstra, H. (2011). *Large-scale turbulence structures in shallow separating flows*. http://resolver.tudelft.nl/uuid:922e297b-19b9-4399-808d-23e837401a52

Thangam, S., & Speziale, C. G. (1991). Turbulent separated flow past a backward-facing step: A critical evaluation of two-equation models. *Https://Doi.Org/10.2514/3.11066*, *30*(5), 1314–1320. https://doi.org/10.2514/3.11066

Thé, J., & Yu, H. (2017). A critical review on the simulations of wind turbine aerodynamics focusing on hybrid RANS-LES methods. *Energy*, *138*, 257–289. https://doi.org/10.1016/J.ENERGY.2017.07.028

Townsend, A. A. (1976). *Structure of Turbulent Shear Flows*. Cambridge University Press.

Tu, J., Yeoh, G.-H., & Liu, C. (2018). CFD Solution Procedure: A Beginning. *Computational Fluid Dynamics*, 33–63. https://doi.org/10.1016/B978-0-08-101127-0.00002-7

Uijttewaal, W. S. J., Lehmann, D., & Mazijk, A. van. (2001). Exchange Processes between a River and Its Groyne Fields: Model Experiments. *Journal of Hydraulic Engineering*, *127*(11), 928–936. https://doi.org/10.1061/(ASCE)0733-9429(2001)127:11(928)

van Prooijen, B. C., Battjes, J. A., & Uijttewaal, W. S. J. (2005). Momentum Exchange in Straight Uniform Compound Channel Flow. *Journal of Hydraulic Engineering*, *131*(3), 175–183. https://doi.org/10.1061/(ASCE)0733-9429(2005)131:3(175)

van Prooijen, B. C., & Uijttewaal, W. S. J. (2002). A linear approach for the evolution of coherent structures in shallow mixing layers. *Physics of Fluids*, *14*(12), 4105. https://doi.org/10.1063/1.1514660

van Velzen, G., Raaijmakers, T. C., & Hoffmans, G. J. C. M. (2014). Scour development around the Eastern Scheldt storm surge barrier-field measurements and model predictions. *Scour and Erosion - Proceedings of the 7th International Conference on Scour and Erosion, ICSE 2014*, 693–704. https://doi.org/10.1201/B17703-90

Versteeg, H., & Malalasekera, W. (2007). *An Introduction to Computational Fluid Dynamics: The Finite Volume Method* (2nd ed.).

White, F. (2009). *Fluid Mechanics* (7th ed.). McGraw-Hill,. 192.168.6.56/handle/123456789/4025

Wilcox, D. C. (2012). Formulation of the k-w Turbulence Model Revisited. *AIAA Journal*, *46*(11), 2823–2838. https://doi.org/10.2514/1.36541

Zanke, U. (1978). Zusammenhänge zwischen Strömung und Sedimenttransport. *Mitteilungen Franzius Inst Wasserbau Küs-Teningenieurswesen Tech Univ Hannover*, *47*, 214–345.

Appendix A: SIMPLE Results

This section provides a brief overview of the results obtained from the implementation of the SIMPLE algorithm. It is important to note that a grid independence analysis was not conducted, and therefore, the focus is solely on the convergence of the residuals using a medium-mesh configuration.

A.1. Monitoring Convergence

The convergence analysis of the SIMPLE algorithm was performed to assess the convergence behaviour. Here, the residuals of the velocities, pressure, k, ε and ω are presented. Although convergence alone does not represent accuracy, it sheds light on the stability and reliability of the algorithm. Upon analysing the convergence behaviour, regardless of the turbulence closure model or the cases, it was observed that convergence could not be achieved in any of the cases. Instead, it can a diverging solution was found.

For brevity, case S4A and case S2D are used as example to highlight the represent the vertically attaching and separating cases, with both the $k - \varepsilon$ and $k - \omega$ SST. Figure 40 and Figure 41 illustrate the inability to achieve the desired convergence level of $O(10^{-6})$ of case S4A and case S2D, respectively. The observed lack of convergence raises the possibility of transient behaviour in the simulated flow, which is attributed to the unsteady nature of flow separation phenomena. After all, flow separation (or attachment) is unsteady and may only occur for a part of the total time considered (Talstra, 2011). These unsteady characteristics manifest as persistent fluctuations in the flow field from one iteration to the next, which prevents the residuals from reaching the desired level as the solution attempts to reach for a steady state that does not exist due to the inherently unsteady flow separation process.

While transient behaviour is a plausible explanation, it is important to explore other contributing factors that may hinder convergence. Inaccurate solver settings or numerical settings could potentially contribute to the convergence difficulties, which warrant further investigation on their impact on the convergence behaviour. However, a notable point supporting the transient behaviour hypothesis is the successful convergence achieved with the PIMPLE algorithm, a transient solver, while keeping all other aspects of the simulations unchanged.
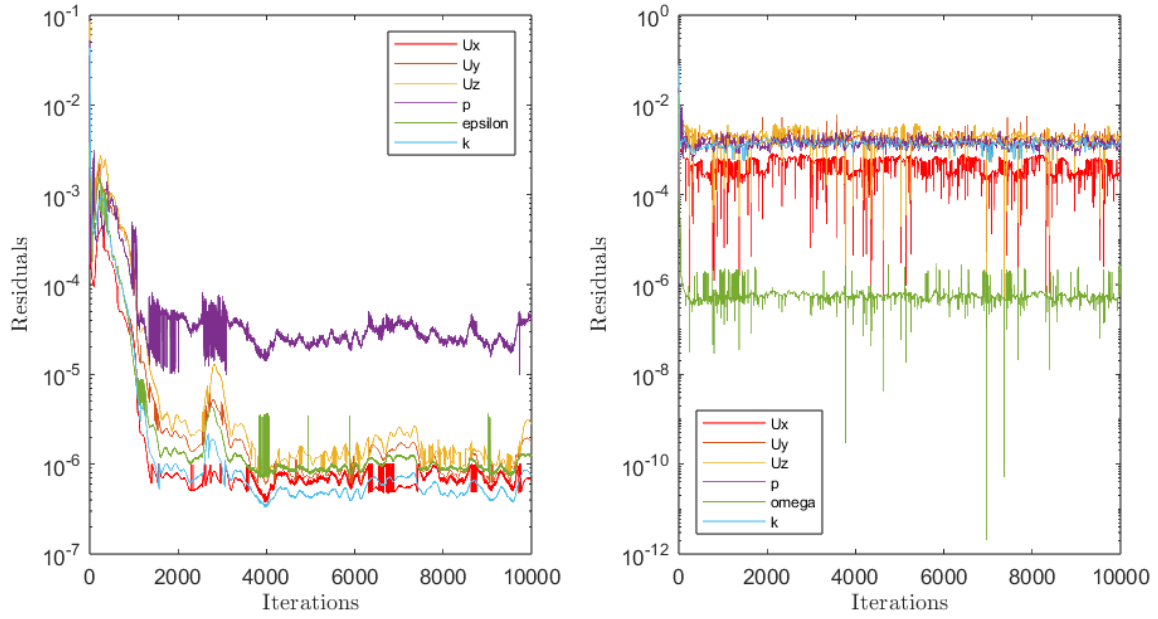
Figure 40: Residuals of the RANS-simulation with $k - \varepsilon$ model (left) and $k - \omega$ SST model (right) and the SIMPLE algorithm of case S4A using the medium resolution mesh.
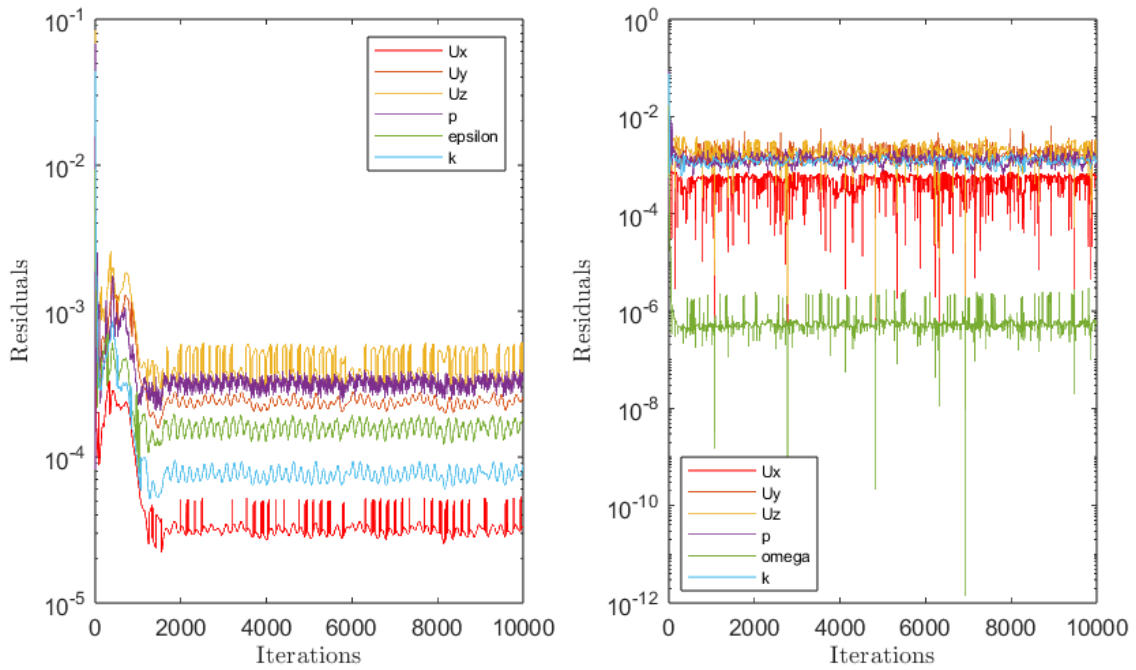

Figure 41: Residuals of the RANS-simulation with $k - \varepsilon$ model (left) and $k - \omega$ SST model (right) and the SIMPLE algorithm of case S2D using the medium resolution mesh.

A.2. Flow velocities

In this section, the flow velocities obtained from the SIMPLE algorithm for case S4A and S2D are presented. In the vertically attaching case (S4A), both the $k - \omega$ SST and $k - \varepsilon$ model are able to reproduce the expected flow behaviour, where the flow converges and remains attached to the bed over the slope. Conversely, in the vertically separating case (S2D), it is evident from Figure 44 and Figure 45 that the flow does not exhibit divergence upstream of the slope and flow separation is not observed. Instead, the flow closely resembles that of a vertically attached case. Adjustments in the outlet pressure boundary condition (S2Dp) do not induce flow divergence and separation at the slope for both turbulence closure models, as depicted in Figure 46 and Figure 47.
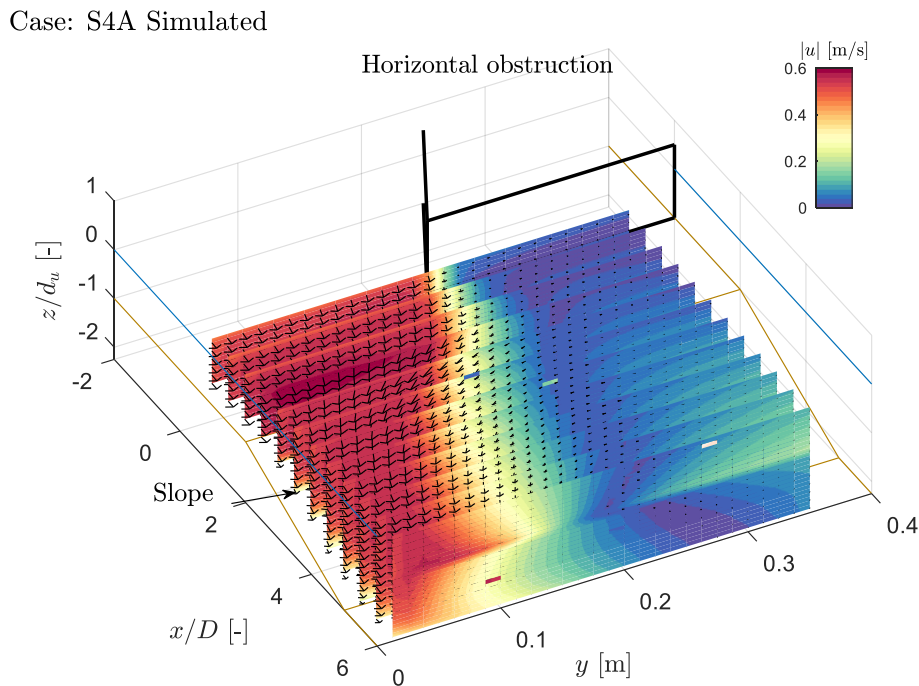

Figure 42: The three-dimensional representation of the flow field of case S4A with the $k - \varepsilon$ turbulence closure model and SIMPLE algorithm. The origin of the x-axis, $x/D = 0$, is located at the downstream end of the obstruction. The colour bar represents the magnitude of the mean velocity $|\bar{u}| = \sqrt{\bar{u}_1^2 + \bar{u}_2^2 + \bar{u}_3^2}$. Obtained from the simulation.
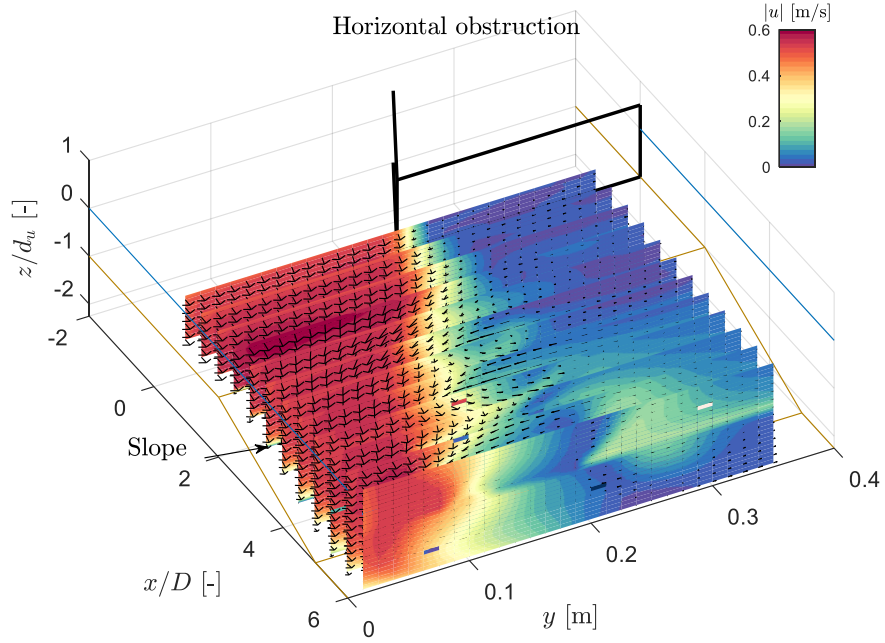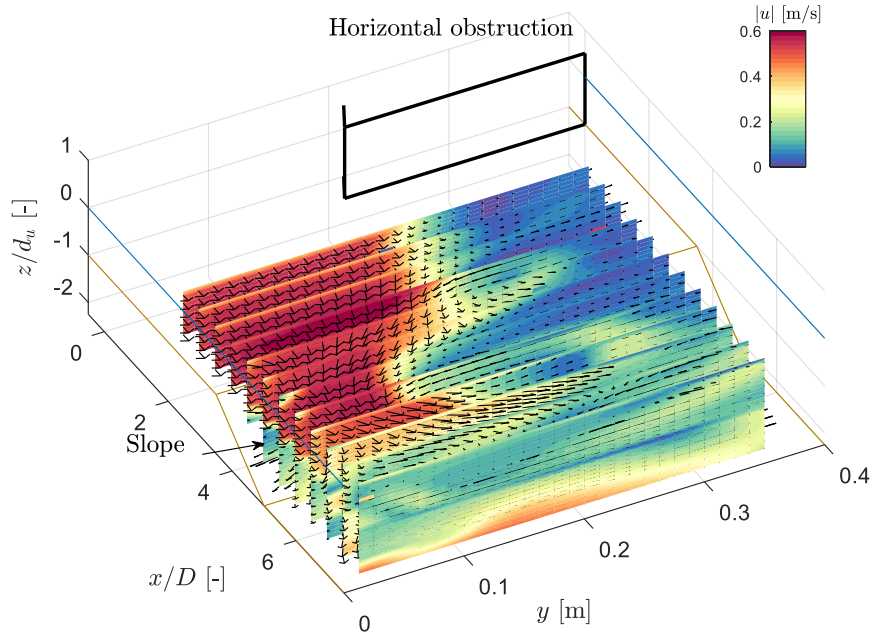
Case: S4A Simulated

Figure 43: The three-dimensional representation of the flow field of case S4A with the $k - \omega$ SST turbulence closure model and SIMPLE algorithm. The origin of the x-axis, $x/D = 0$, is located at the downstream end of the obstruction. The colour bar represents the magnitude of the mean velocity $|\bar{u}| = \sqrt{\bar{u}_1^2 + \bar{u}_2^2 + \bar{u}_3^2}$. Obtained from the simulation.

Case: S2D Simulated

Figure 44: The three-dimensional representation of the flow field of case S2D with the $k - \omega$ SST turbulence closure model and SIMPLE algorithm. The origin of the x-axis, $x/D = 0$, is located at the downstream end of the obstruction. The colour bar represents the magnitude of the mean velocity $|\bar{u}| = \sqrt{\bar{u}_1^2 + \bar{u}_2^2 + \bar{u}_3^2}$. Obtained from the simulation.
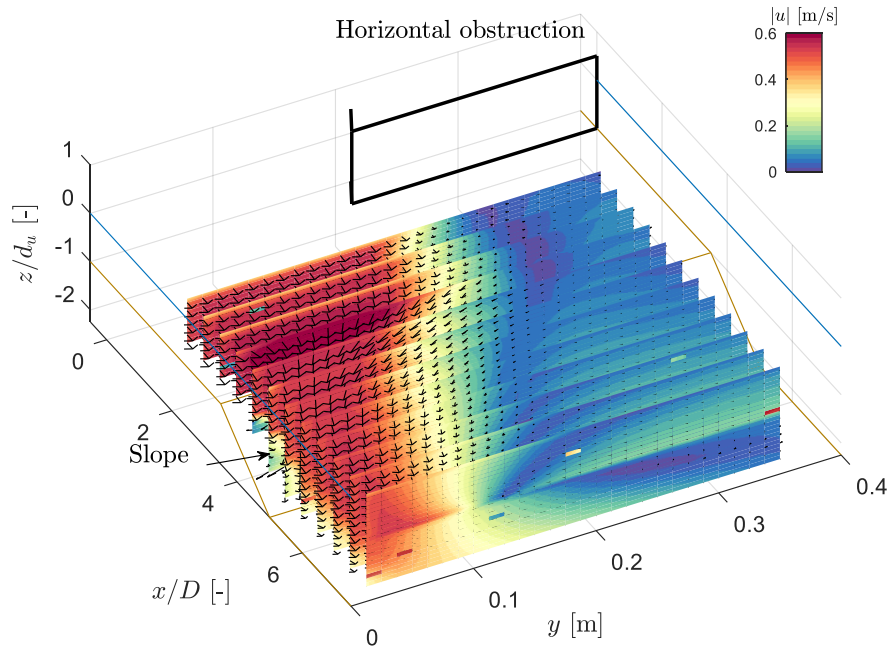
Figure 45: The three-dimensional representation of the flow field of case S2D with the $k - \varepsilon$ turbulence closure model and SIMPLE algorithm. The origin of the x-axis, $x/D = 0$, is located at the downstream end of the obstruction. The colour bar represents the magnitude of the mean velocity $|\bar{u}| = \sqrt{\bar{u}_1^2 + \bar{u}_2^2 + \bar{u}_3^2}$. Obtained from the simulation.

Figure 46: The three-dimensional representation of the flow field of case S2Dp with the $k - \varepsilon$ turbulence closure model and SIMPLE algorithm. The origin of the x-axis, $x/D = 0$, is located at the downstream end of the obstruction. The colour bar represents the magnitude of the mean velocity $|\bar{u}| = \sqrt{\bar{u}_1^2 + \bar{u}_2^2 + \bar{u}_3^2}$. Obtained from the simulation.
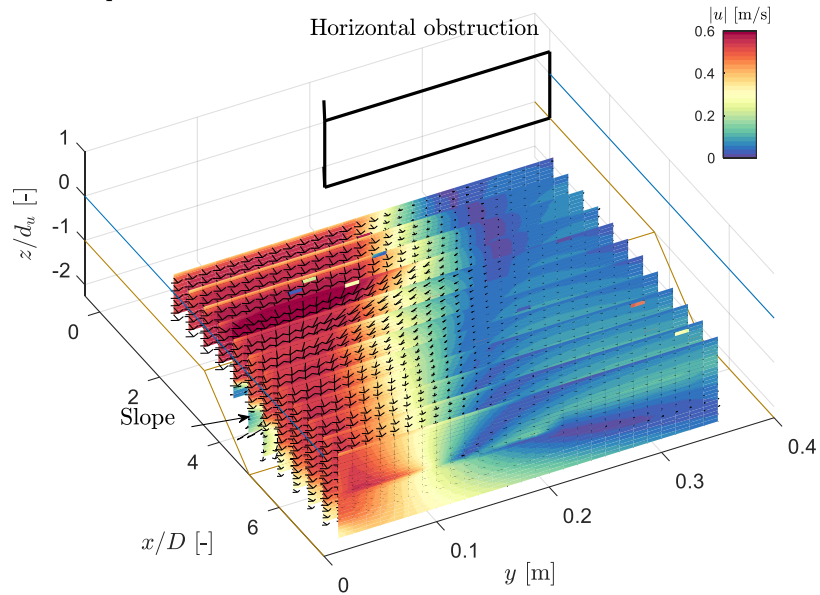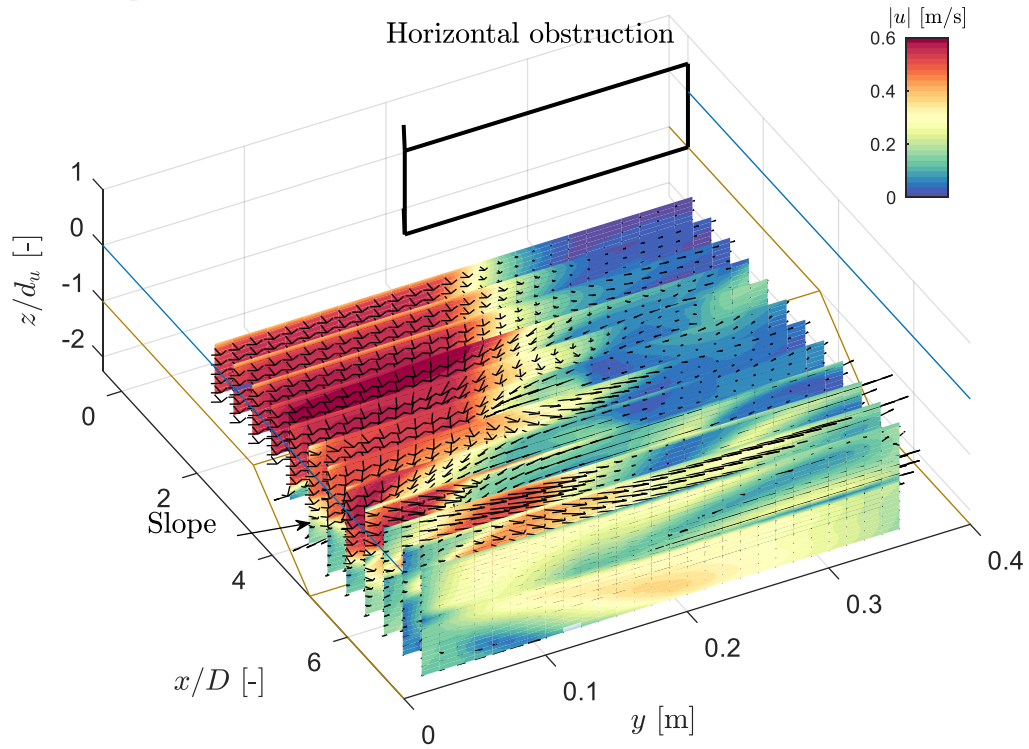
Case: S2Dp Simulated

Figure 47: The three-dimensional representation of the flow field of case S2Dp with the $k - \omega$ SST turbulence closure model and SIMPLE algorithm. The origin of the x-axis, $x/D = 0$, is located at the downstream end of the obstruction. The colour bar represents the magnitude of the mean velocity $|\bar{u}| = \sqrt{\bar{u}_1^2 + \bar{u}_2^2 + \bar{u}_3^2}$. Obtained from the simulation.

Appendix B: Lateral velocity profiles from various mesh resolutions

In the following section, the lateral velocity profiles obtained with all the mesh resolutions considered are presented for all cases, including the measurement data and the plane bed reference.
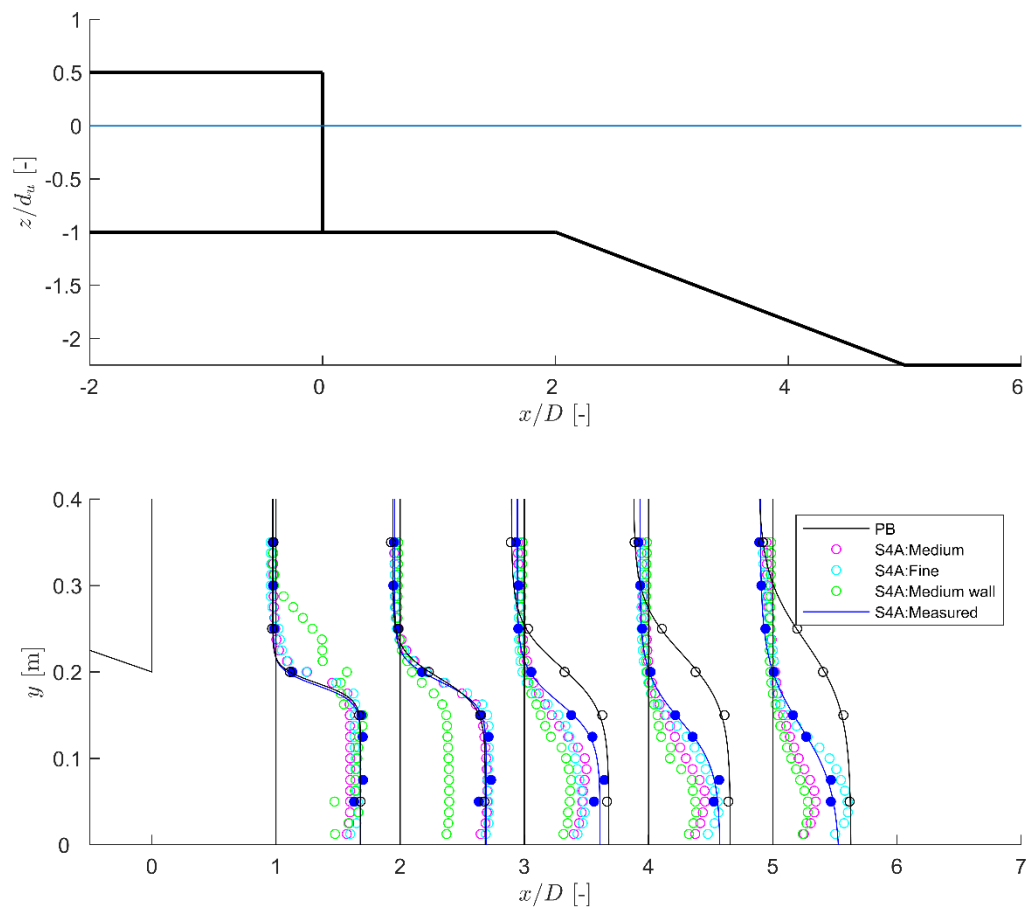

Figure 48: Lateral mixing layer profile of the depth-averaged streamwise velocity of the model (of various mesh resolutions) and measurement as a function of streamwise distance. The measurements are plotted in both solid lines (fitted hyperbolic-tangent profile) and round markers (measured) for cases PB and S4A. The top panel guides the reader regarding the position of the slope.
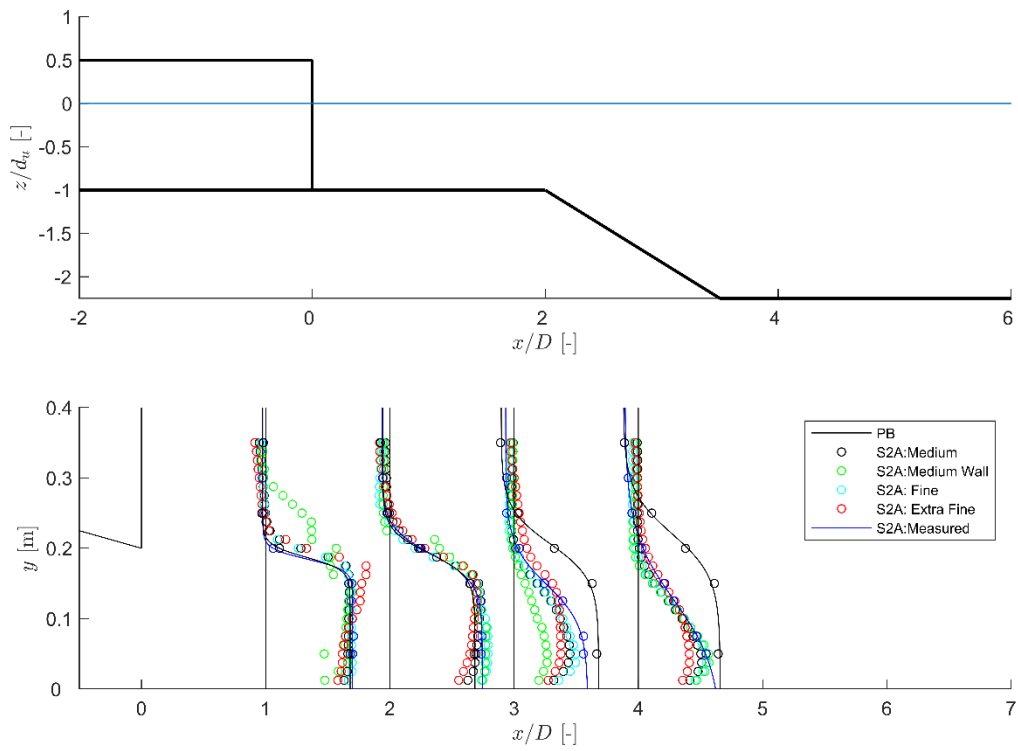
Figure 49: Lateral mixing layer profile of the depth-averaged streamwise velocity of the model (of various mesh resolutions) and measurement as a function of streamwise distance. The measurements are plotted in both solid lines (fitted hyperbolic-tangent profile) and round markers (measured) for cases PB and S2A. The top panel guides the reader regarding the position of the slope.
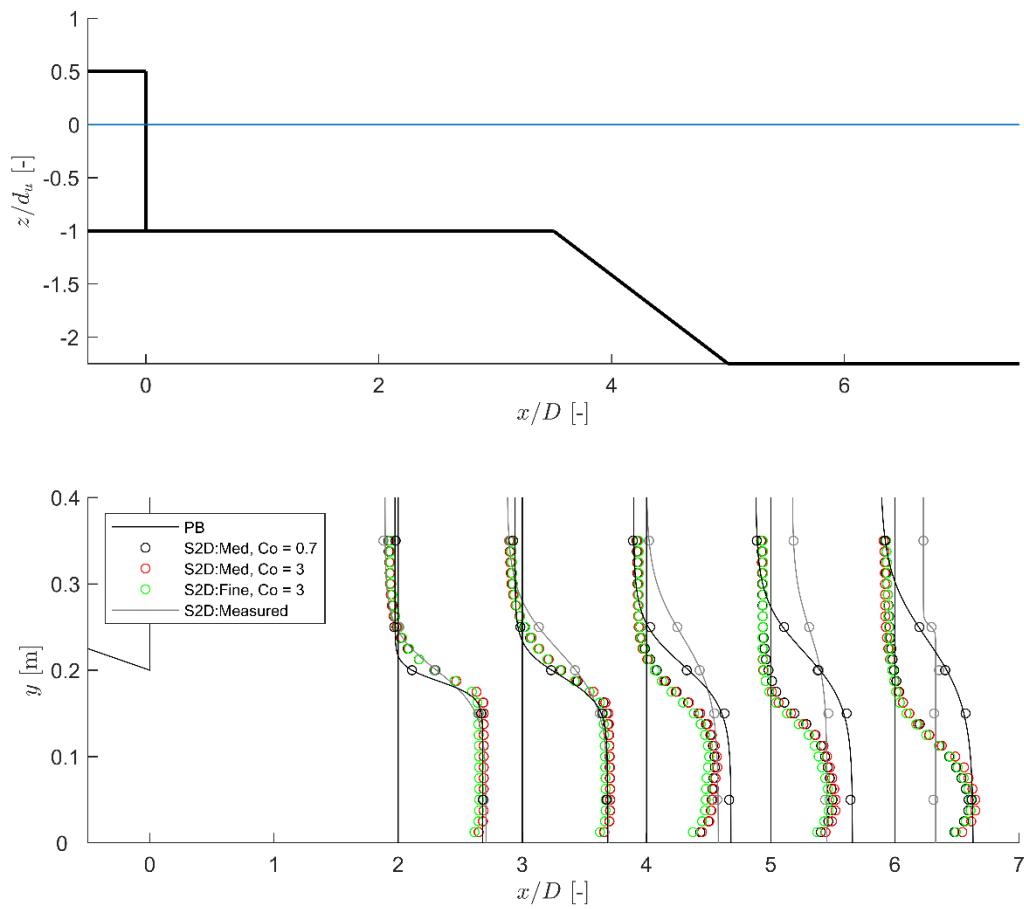
Figure 50: Lateral mixing layer profile of the depth-averaged streamwise velocity of the model (of various mesh resolutions) and measurement as a function of streamwise distance. The measurements are plotted in both solid lines (fitted hyperbolic-tangent profile) and round markers (measured) for cases PB and S2D without adjustments in the pressure outlet boundary condition. The top panel guides the reader regarding the position of the slope.

Appendix C: PIMPLE results with the $k - \varepsilon$ model

In this section, the result obtained from the RANS simulation using the PIMPLE algorithm and the $k - \varepsilon$ model are presented for the vertically separating (S2Dp) and attaching case (S4A) with the medium resolution mesh. Similar to the findings with the $k - \omega$ SST model, the $k - \varepsilon$ model failed to reproduce the flow divergence and separation phenomenon without adjustments in the pressure outlet boundary. Notably, even after adjustments were made to the pressure outlet boundary, the $k - \varepsilon$ model still fell short in simulating flow separation; highlighting the limitation of the $k - \varepsilon$ model in simulating flow separation as shown in Figure 51.
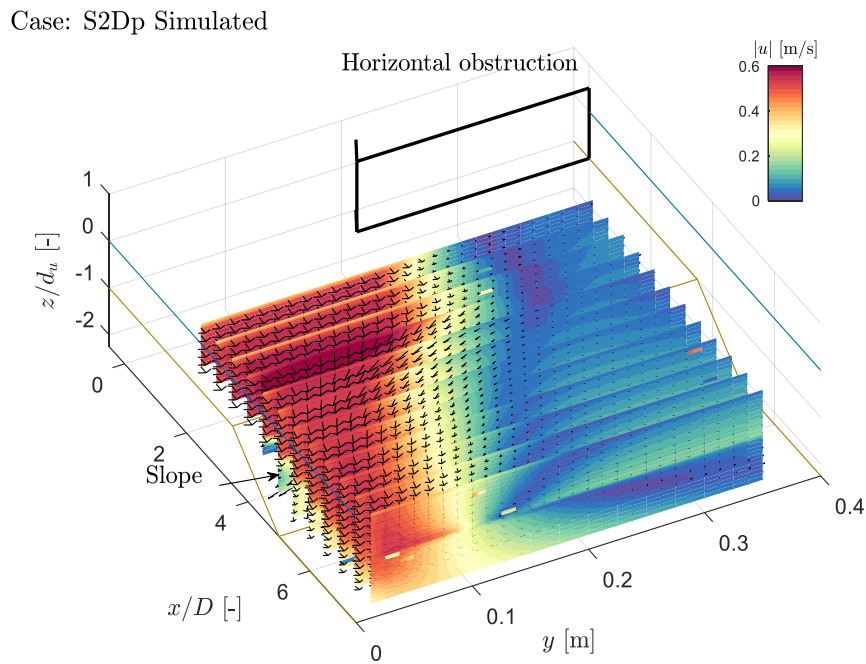

Figure 51: The three-dimensional representation of the flow field of case S2Dp with the $k - \varepsilon$ turbulence closure model and PIMPLE algorithm. The origin of the x-axis, $x/D = 0$, is located at the downstream end of the obstruction. The colour bar represents the magnitude of the mean velocity $|\bar{u}| = \sqrt{\bar{u}_1^2 + \bar{u}_2^2 + \bar{u}_3^2}$. Obtained from the simulation.

The $k - \varepsilon$ model was also tested for the vertically attaching case S4A. Although it was able to simulate the flow characteristics correctly (i.e., flow convergence and attachment), its performance was inferior to the $k - \omega$ SST model. When comparing the time-averaged flow velocities between the model and the measurements, the $k - \varepsilon$ model exhibited higher MAE (0.051 m/s) and RMSE (0.075 m/s) than its $k - \omega$ SST counterpart. Hence, these results provide further justification for choosing the $k - \omega$ SST model.
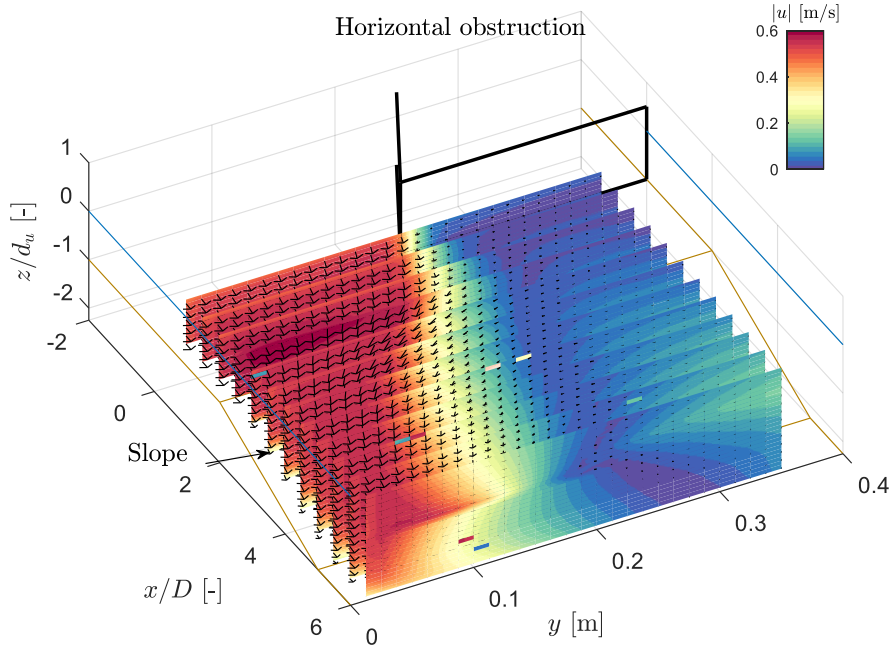
Figure 52: The three-dimensional representation of the flow field of case S4A with the $k - \varepsilon$ turbulence closure model and PIMPLE algorithm. The origin of the x-axis, $x/D = 0$, is located at the downstream end of the obstruction. The colour bar represents the magnitude of the mean velocity $|\bar{u}| = \sqrt{\bar{u}_1^2 + \bar{u}_2^2 + \bar{u}_3^2}$. Obtained from the simulation.